

QC  
807.5  
.U66  
no.454  
c.2

NOAA Technical Report ERL 454-ETL 68



# **Turbulence-Induced Ionization Fluctuations in the Lower Ionosphere**

R.J. Hill  
K.A. Mitton

November 1998

**U.S. DEPARTMENT OF COMMERCE**  
National Oceanic and Atmospheric Administration  
Environmental Research Laboratory

NOAA Technical Report ERL 454-ETL 68



# **Turbulence-Induced Ionization Fluctuations in the Lower Ionosphere**

Reginald J. Hill  
Kenneth A. Mitton

Environmental Technology Laboratory  
Boulder, Colorado

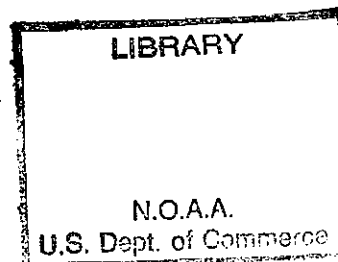
November 1998

QC  
B07.5  
.U66  
no. 454  
c. 2

**U.S. Department of Commerce**  
William M. Daley, Secretary

National Oceanic and Atmospheric Administration  
D. James Baker, Under Secretary for Oceans and Atmosphere/Administrator

Environmental Research Laboratories  
Silver Springs, Maryland  
James L. Rasmussen, Director



## NOTICE

Mention of a commercial company or product does not constitute an endorsement by NOAA/ERL. Use for publicity or advertising purposes of information from this publication or concerning proprietary products or the tests of such products is not authorized.

# CONTENTS

ABSTRACT .....	1
1. INTRODUCTION .....	1
1.1 Introduction to the Current Study .....	1
1.2 Historical Introduction to Ionospheric Applications .....	2
1.3 Introduction to Turbulent Advection Modeling .....	8
2. EQUATIONS FOR PLASMA DYNAMICS COUPLED TO HYDRODYNAMIC TURBULENCE .....	11
3. PLASMA ADVECTION WITH DIFFUSION .....	15
4. PERTURBATION ANALYSIS .....	18
5. EQUATIONS FOR SPECTRA AND COSPECTRA .....	23
6. APPLICATION OF THE TURBULENCE ADVECTION MODEL .....	26
6.1 Locally Stationary Case With No Coupling to Temperature Fluctuations .....	26
6.2 Locally Stationary Case With Coupling to Temperature Fluctuations .....	29
6.3 The Nonstationary Case .....	32
7. THE POWER SPECTRUM OF ELECTRON-CONCENTRATION FLUCTUATIONS ...	35
8. BOUNDARY CONDITIONS .....	38
8.1 Boundary Conditions for the Stationary Case With Coupling to Temperature Fluctuations .....	38
8.2 Boundary Conditions for the Nonstationary Case With No Coupling to Temperature Fluctuations .....	40
8.3 Boundary Conditions for the Nonstationary Case With Coupling to Temperature Fluctuations .....	42
9. LIMITATIONS OF THE NONSTATIONARY CASE .....	49
10. DEFINITION OF DISSIPATION RATES .....	49
11. CALCULATIONS OF SPECTRA AND COSPECTRA .....	56
12. RELATIONSHIP TO RADAR CROSS SECTION AND SCATTERED POWER .....	103
13. DISCUSSION .....	105
14. ACKNOWLEDGMENTS .....	105
15. REFERENCES .....	105
APPENDIX: COLLISION RATE FOR SPECIES $\alpha$ .....	108



# **Turbulence-Induced Ionization Fluctuations in the Lower Ionosphere**

**Reginald J. Hill and Kenneth A. Mitton**

**ABSTRACT.** As part of a larger research project to calculate radar scattering from the lower ionosphere using numerical simulation of internal wave breaking and shear instabilities, subgrid-scale turbulence advection modeling is required to calculate the radar-scattering cross section from the spectrum of electron-concentration fluctuations. The plasma dynamics of multiconstituent ambipolar diffusion is studied to obtain the equations governing the mixing-ratio fluctuations of the ionized species advected by turbulent air. These equations are used with the turbulence advection model to obtain coupled equations for the spectra and cospectra of the ion's mixing ratio and of the potential temperature. The solutions of these equations determine the spectrum of electron-concentration fluctuations. Many example solutions of the equations are presented which include cases of many ion species and cases of very massive ions.

## **1. INTRODUCTION**

### **1.1 Introduction to the Current Study**

Numerical simulations of turbulence will calculate breaking internal-wave events and Kelvin-Helmholtz instabilities for conditions in the lower ionosphere. These simulations will be used to advect initial profiles of ionization to determine the ionization fluctuations at the smallest scales that can be resolved by the simulation. These smallest resolved scales are much larger than the Bragg scales that contribute to radar backscatter of relevant radars. To use the simulation to predict radar backscatter, it is necessary to use subgrid-scale modeling to determine the power spectrum of electron-concentration fluctuations. Evaluation of this spectrum at a radar's Bragg wavenumber determines the scattering cross section. Of particular interest are the polar mesospheric summer echoes (PMSE), which might be caused by the presence of massive ions. However, PMSE are only one specific application of our general formulation.

The subgrid-scale model is an application of the turbulence advection model and plasma dynamics developed by Hill and Bowhill (1976). The method in this report requires equations that are coupled by the ambipolar electric field.

In section 2, we formulate the relevant plasma dynamics for an arbitrary number of ionized species. The equations are expressed in terms of mixing ratios rather than concentrations of the species because the mixing ratios are conserved quantities in the numerical simulation. In section 3, the plasma dynamics is specialized to describe the phenomenon of multispecies,

quasi-neutral plasma diffusion. This diffusion phenomenon acts to dissipate the ionization fluctuations. In section 4, a perturbation analysis is used to linearize the nonlinear plasma diffusion equations. The result is coupled linear equations for the Fourier transforms of the mixing ratios of all the ion species.

In section 5, the linearized equations are used to formulate coupled equations for the ensemble-averaged spectra and cospectra of the mixing ratios for the ion species. In section 6, the turbulence advection model is applied to the coupled equations, resulting in equations that can be solved by a predictor-corrector integration algorithm. Section 6.1 presents the simplest case of local stationarity and no coupling to temperature fluctuations. Section 6.2 describes the complication caused by coupling to temperature fluctuations. Section 6.3 presents the nonstationary case. The boundary conditions for these several cases are given in section 8. Boundary conditions are needed to initialize the predictor-corrector algorithm. The limitations of the nonstationary case caused by the approximations employed are discussed in section 9.

The power spectrum of electron-concentration fluctuations is needed for calculation of the radar-scattering cross section. Section 7 shows how to calculate this electron-concentration spectrum from the advection model's determination of mixing-ratio and potential-temperature spectra and cospectra. The relevance of the electron-concentration spectrum to the radar cross section and scattered power is given in section 12.

Section 11 gives numerous examples of the numerical solution for the various spectra and cospectra. The input parameters for these computed examples are somewhat arbitrary. When applied with the numerical simulation of turbulence generation, the numerical simulations will provide all of the relevant input parameters. Section 10 defines the dissipation rates that are input parameters for the turbulence advection model and shows how these dissipation rates will be calculated from the numerical simulations.

Plasma transport coefficients are needed in the equations. These coefficients depend on the ion-neutral momentum-transfer collision rate. The Appendix explains our calculation of the ion-neutral momentum-transfer collision rate.

## **1.2 Historical Introduction to Ionospheric Applications**

It is important to place the present work in perspective relative to other work done on this subject in the 1970s and the newer work on PMSE in the 1990s. First, we discuss the studies of VHF radar scattering from the mesosphere which took place during the 1970s at Jicamarca, Peru. The turbulence advection model that we use in the current study was developed to explain those observations. We examine the ability of the model to predict the scattered power for the

Jicamarca radar and the sensitivity of the predicted cross section to changes in energy-dissipation rate and Schmidt number. Second, we review more recent theory and observations that confirm and extend the applicability of the advection model. Third, we describe misunderstandings regarding the application to the PMSE phenomenon of both the turbulence advection model and the theory of multiconstituent ionization diffusion.

Prabhat K. Rastogi investigated the scattering of 50-MHz radar waves from the equatorial D-region at Jicamarca, Peru, in the early and mid-1970s. He recognized that the Bragg wavenumber was deep within the viscous range of the energy spectrum for plausible energy-dissipation rates at those altitudes. He thereby determined that the backscattered power significantly exceeded that which could be predicted on the basis of the assumption that the electron-concentration spectrum had the same form as either the energy or temperature spectra of air. The result was a research program to predict the scattered power; the report by Hill and Bowhill (1976) evolved from that research.

The ions had not been observed above Jicamarca during the radar scattering studies, but measurements at other locations and times showed heavy hydrated positive and negative ions at the altitudes of interest and simpler ions at higher altitudes. Because of the lack of simultaneous observation of ion composition during radar observations, it was simplest to assume that the ions of both negative and positive charge had the same diffusion coefficient, although a general theory of multi-ion diffusion had been derived by Hill and Bowhill (1976). For the observed ion masses, it was sufficient to calculate the diffusion coefficients from the polarization interaction; that is, the ions were not so large as to require a hard-sphere repulsion. The essential simplification of equal ion diffusion coefficients is that the electrons then behave as though they have an effective diffusion coefficient; this can be seen in equations (4.105a,b) of Hill and Bowhill (1976) or (17a,b) of Hill (1978a). However, the electrons do not have an effective diffusion coefficient if all the ions do not have the same diffusion coefficient; this can be seen in equations (4.109a,b) and (4.110a) of Hill and Bowhill (1976) or (20a,b) of Hill (1978a). In fact, to quote Hill (1978a), "The linearized version of these equations implies the existence of many diffusion modes: the number of these modes is one less than the number of charged species." The effect on the electron concentration of unequal ion diffusion coefficients can be that the electrons are thrust out of or into the ion perturbation because the electrons go wherever they must to maintain approximate charge neutrality, as illustrated by Hill (1978a) and Hill and Bowhill (1976). This effect is very different from the case of equal diffusion coefficients of all the ions, a case that gives an effective electron diffusion coefficient.

For the case of an effective electron diffusion coefficient, Fig. 8.2 in Hill and Bowhill (1976) shows the Schmidt number effect on the electron-concentration spectrum, and Tables 9.1



and 9.2 in Hill and Bowhill (1976) give the Schmidt numbers and predict cross sections for radar backscatter. However, the Bragg wavenumber used to generate Table 9.2 was in error, so the predicted cross sections are in error. That error is corrected here. One unfortunate aspect of the evaluation of scattering cross sections by Hill and Bowhill (1976) was the necessity of guessing the dissipation rates. Here, knowledge from numerical simulation of the Kelvin-Helmholtz instability is used to estimate the dissipation rates and, thereby, the radar scattering cross sections.

Current understanding of the Kelvin-Helmholtz instability in the upper atmosphere suggests a billow length of about 4 km, which results in a turbulent layer about 2 km in depth. Entrainment of ionization is greatest at the top and bottom of the layer, whereas radio scattering strength requires that the energy dissipation rate also be large. Numerical simulation of the instability shows that energy-dissipation peaks near the middle of the layer. The result of large entrainment of ionization at the edges of the turbulent layer and of energy dissipation increasing toward the middle of the layer is that scattering strength is greatest in two zones separated vertically by about 1 km. Therefore, a single Kelvin-Helmholtz instability produces a turbulent layer about 2 km in depth that appears as two scattering layers separated by about 1 km. Since the horizontal wind differs at the two scattering layers, the Doppler spectrum has the appearance observed by Rastogi and Bowhill (1976). Indeed, Rastogi and Bowhill (1976) interpreted their observed Doppler spectra as evidence for two scattering layers separated by at least 1 km. It is now clear that this observation can result from a single unstable Kelvin-Helmholtz billow. Rastogi and Woodman (1974) used the Jicamarca radar to observe scattered power that is 4–18 dB greater than the incoherent scatter power (assuming 500 electrons per cubic centimeter). For two dominant scattering zones of depth 300 m each and the 5000-m range resolution of the Jicamarca radar as implemented by Rastogi and Woodman (1974), the measurements of scattered power by Rastogi and Woodman (1974) suggest that the scattering cross section per unit volume within the dominant scattering zones is  $5 \times 10^{-21}$  to  $1.3 \times 10^{-19} \text{ cm}^{-1}$ .

One can evaluate the scattering cross-section formula (9.2) in Hill and Bowhill (1976) using either model 2 or model 4 by Hill (1978b). Because the Schmidt numbers are sufficiently high, these models can be approximated by their asymptotic formulas. Hill (1978b) showed that these formulas correspond to Batchelor's (1959) and Kraichnan's (1968) theories for models 2 and 4, respectively. The asymptotic formula for model 2 was used in the evaluation by Hill and Bowhill (1976). Model 4 was shown to be more accurate in comparison with data than model 2 by Hill (1978b); this was recently confirmed by Bogucki et al. (1997) and Chasnov (1998) by means of comparing numerical simulation of scalar advection with Batchelor's and Kraichnan's

theories. Using equation (9.2) of Hill and Bowhill (1976), the formulas for the cross section per unit volume are as follows:

$$\sigma = r_e^2 2\pi^2 \chi K^{-3} (\epsilon/\nu)^{-1/2} F(K)$$

$$F(K) \equiv \begin{cases} 4.08 \exp(-\rho_B) & \text{(model 2)} \\ 5.10 (1 + \rho_K) \exp(-\rho_K) & \text{(model 4)} \end{cases}$$

$$\rho_B \equiv 4.08 \text{ Sc}^{-1} (K/k_d)^2$$

$$\rho_K \equiv 5.52 \text{ Sc}^{-1/2} (K/k_d)$$

$$k_d \equiv (\epsilon/\nu^3)^{1/4}.$$

Here,  $\sigma$  is the cross section per unit volume,  $r_e$  is the classical electron radius,  $\chi$  is the dissipation rate of electron-concentration fluctuations,  $K$  is the Bragg wavenumber,  $\epsilon$  is the energy dissipation rate,  $\nu$  is kinematic viscosity,  $k_d$  is Kolmogorov's dissipation wavenumber, and  $\text{Sc}$  is the Schmidt number.

For the height of 70 km, which corresponds to the height of the observation of Rastogi and Woodman (1974), we use the Schmidt number from Table 9.1 of Hill and Bowhill (1976); namely,  $\text{Sc} = 1.1$ . The kinematic viscosity at 70 km is  $\nu = 1643 \text{ cm}^2 \text{ s}^{-1}$ . We take  $\epsilon = 1000 \text{ cm}^2 \text{ s}^{-3}$ , which is obtained from the numerical simulation of the Kelvin-Helmholtz instability at an active stage of its development. At this same stage, the numerical simulation gives a dissipation rate of potential-temperature fluctuations of  $0.01 \text{ K}^2 \text{ s}^{-1}$  in the two entrainment zones. The initial potential-temperature gradient of the simulation was  $4.73 \text{ K km}^{-1}$ , which gives a temperature gradient of  $-4.75 \text{ K km}^{-1}$ , a reasonable temperature gradient for the height of 70 km. The electron-concentration dissipation rate,  $\chi$ , can be obtained by multiplying the potential-temperature dissipation rate by the square of the ratio of the gradient of electron-concentration mixing ratio to the gradient of the potential temperature and also multiplying by the square of the concentration of neutrals. The electron-concentration gradient at 70 km for active sun is about  $54 \text{ cm}^{-3} \text{ km}^{-1}$ , and the contribution of the height variation of the neutral density for an electron concentration of  $500 \text{ cm}^{-3}$  is  $76 \text{ cm}^{-3} \text{ km}^{-1}$ . Adding these, we obtain  $130 \text{ cm}^{-3} \text{ km}^{-1}$  for the total gradient of the electron mixing ratio times the neutral density. The resultant electron-concentration dissipation rate corresponding to the simulation and to a height of 70 km is  $\chi = 7.5 \text{ cm}^{-6} \text{ s}^{-1}$ . The Bragg wavenumber of the Jicamarca radar is  $k = 2.1 \times 10^{-2} \text{ rad cm}^{-1}$ . Evaluation of the cross section gives

$$\rho_B = 3.44$$

$$\rho_K = 5.07$$

$$\sigma \equiv \begin{cases} 2 \times 10^{-19} \text{ cm}^{-1} & \text{(model 2)} \\ 3 \times 10^{-19} \text{ cm}^{-1} & \text{(model 4).} \end{cases}$$

From the measurements of Rastogi and Woodman (1974), recall that the cross section per unit volume within the dominant scattering zones is typically in the range of  $5 \times 10^{-21}$  to  $1.3 \times 10^{-19} \text{ cm}^{-1}$ . By using a very active stage of the Kelvin-Helmholtz instability, we obtain a cross section at the upper end of the observed range. Clearly, evaluation of the cross section at less active stages would account for the lesser values of the cross section. Significantly, the arguments of the exponentials, namely,  $\rho_B$  and  $\rho_K$ , are large. Indeed, the Bragg wavenumber is nearly equal to the Kolmogorov wavenumber for the height of 70 km and  $\varepsilon = 1000 \text{ cm}^2 \text{ s}^{-3}$ . The large value of the argument of the exponentials results in the sensitivity of the scattered power to the variation of  $\varepsilon$  that was discovered by Rastogi and Bowhill (1976). Also significant is the sensitivity of the arguments of the exponentials to the Schmidt number  $Sc$ . For instance, consider replacing the value of  $Sc$  with the value pertaining to neutral density, which is the same as the Prandtl number, namely,  $Sc = Pr = 0.72$ . With this replacement, our evaluation of the cross section per unit volume becomes  $3.4 \times 10^{-20} \text{ cm}^{-1}$  for model 2 and  $1.1 \times 10^{-19} \text{ cm}^{-1}$  for model 4. Thus, at least when using Batchelor's (1959) theory (i.e., model 2), one would find it difficult to predict the largest observed cross sections if  $Sc = 0.72$ .

The importance of the enhanced  $Sc$  and its evaluation from the theory of ion-neutral collisions is a central theme of Hill and Bowhill (1976). Rastogi was well aware of the Schmidt number effect at the earliest stages of the research. Rastogi (private communication, 1975) suggested to one of the authors (Hill) that the Schmidt number would be very large if the ions were very large, and he suggested that this would result in radio scatter for frequencies substantially larger than 50 MHz. He further suggested that noctilucent clouds were evidence that such large ions could exist. However, there was no evidence that the very large ions would be present in great enough numbers, and it was unlikely that the equatorial ionosphere observed by the Jicamarca radar would contain such very large ions. What is remarkable about this insight by Rastogi is that it was a prediction of the PMSE phenomenon many years before its discovery.

Kelley et al. (1987) and Kelley and Ulwick (1988) proposed that very large ions produce large Schmidt numbers in the summer polar mesopause region and that the Schmidt number effect produces enhanced radar scattering. This idea was studied on the basis of multiconstituent

ionization diffusion by Cho et al. (1992) and Cho (1993), who used as the basis for their development the multiconstituent ionization diffusion theory derived by Hill and Bowhill (1976) and further developed by Hill (1978a). However, the use of the multiconstituent ionization diffusion theory by Cho et al. (1992) is incorrect, as we show in the next paragraph. Their error appears to originate in the misconception that the turbulence advection model requires that the diffusion theory be reduced to having an “effective electron diffusivity” as its sole descriptor. This is not a limitation of the turbulence advection model.

The case of electrons, one type of positive ion having diffusivity  $D_+$  and one type of negative ion having diffusivity  $D_-$ , is sufficient to show that the effective electron diffusivity used by Cho et al. (1992) and Cho (1993) is incorrect. As explained by Hill (1978a), the case in which  $D_+$  is not equal to  $D_-$  has two diffusion modes, having diffusion coefficients that differ from the effective electron diffusivity determined by Cho et al. (1992) and Cho (1993). Figure 3 of Hill (1978a) shows the case of ten times as many negative ions than positive ions and  $D_+ = 10 D_-$ . (This case is qualitatively similar to negatively charged aerosols, for which  $D_+ \gg D_-$ .) The behavior of electrons in this figure is not that described by an effective electron diffusivity; the electrons are thrust away from the ions’ perturbations by the ambipolar electric field. As shown by Hill (1978a), this situation can be reversed by a different initial condition. That is, if the negative aerosols have a local enhancement where positive ions have a local deficit, then the inward diffusion of positive ions and outward diffusion of negative aerosol cause the electrons to rush inward. Such an initial condition could arise in the ionosphere. Thus, the initial condition can control the nature of the diffusion. Another case of this control by the initial condition is given by Hill (1978a). In Appendix A of Cho (1993), he observed that his simulations of the diffusion equations had two distinct modes that may have very different corresponding time scales and that the simulations were sensitive to the initial conditions. He nonetheless obtained an effective electron diffusivity by finding an  $e^{-1}$  time of the perturbation. This does not produce a useful or correct descriptor for the problem.

One misunderstanding caused by Cho’s (1993) insistence that his simulations produce an effective electron diffusivity is that the Schmidt number cannot be large unless the total charge on the aerosols is at least 1.2 times the electron charge density if the aerosols are negatively charged and at least 0.6 times the electron charge density if the aerosols are positively charged. This misunderstanding appears in Cho et al. (1992, 1996), as well as in Cho (1993). Certainly, a significant charge on very large ions enhances electron-concentration fluctuations at small spatial scales. However, the Schmidt numbers are determined from ion-neutral momentum-transfer collision frequencies; as such, the Schmidt numbers for multiconstituent ionization diffusion are independent of charge densities.

There are several other inaccuracies with regard to the multiconstituent ionization diffusion theory by Cho (1993). Because his equations apply to arbitrary charge of the ions, he stated that his diffusion theory was more general than that by Hill (1978a). In fact, the theory by Hill (1978a) does apply to multiply charged ions, as is clear from the derivation of that theory, as well as from the yet more general theory of modes of a weakly ionized plasma by Hill and Bowhill (1977a). In addition, the theory by Hill (1978a) is more general than that by Cho (1993) in that it includes the case of nonzero Debye length, a case that is of some interest for the smallest spatial scales of the ionization fluctuations.

It seems that Cho (1993) used an incorrect value of the parameter describing the transition between the inertial- and viscous-convective ranges. Hill (1978b) showed that the correct onset of the viscous-convective range was at such a low wavenumber relative to Kolmogorov's scaling wavenumber that a nascent viscous-convective range appears even for a Schmidt number less than unity. On this basis, one should clearly see about a decade of viscous-convective range in Cho's (1993) Figs. 4.3 and 4.5 for the case of a Schmidt number equal to 10; in fact, the viscous-convective range is hardly evident for that case.

One motivation for the current study is to put the turbulence advection modeling of multiconstituent ionization on a correct basis. In particular, a correct description of the role of very large ions in the PMSE phenomenon is sought.

### **1.3 Introduction to Turbulent Advection Modeling**

Since the mid-1970s, several advances in the turbulence advection model have added to its reliability. The turbulence advection model of Hill and Bowhill (1976), as well as several other models, was compared with data by Hill (1978b). The data were the temperature power spectra measured in air, water, and mercury, for which the ratio of thermal diffusivity to kinematic viscosity are 0.7, 9.0, and 0.02, respectively (these ratios are the Prandtl numbers), as well as the ammonium acetate power spectrum for which the ratio of molecular diffusivity to kinematic viscosity is 700 (this ratio is the Schmidt number). This comparison with data showed the model to be in excellent agreement with data for this enormous range of Prandtl and Schmidt numbers. Furthermore, the comparison established an accurate value for the wavenumber of the transition between inertial- and viscous-convective ranges of the spectrum relative to Kolmogorov's dissipation wavenumber. (The latter is the inverse of the Kolmogorov microscale.) This ratio of the transition wavenumber to Kolmogorov's dissipation wavenumber is one parameter of the model. The comparison with data also established an accurate value of the other parameter of the model, namely, the width of the transition between the inertial- and

viscous-convective ranges. Thus, the model has no unknown parameters, and no parameters can be adjusted.

The irradiance scintillations of laser light propagating through the turbulent atmosphere can be used as a stringent test of the model's accuracy. This is because irradiance scintillations are sensitive to the dissipation range and to the features in the refractive-index spectrum that arise due to the transition between the inertial-convective range, the viscous-convective range, and the viscous-diffusive range. Atmospheric scintillation experiments by Hill and Ochs (1978), Ochs and Hill (1985), Azoulay et al. (1988), Frehlich (1992), Hill and Ochs (1992), and Thiermann and Grassl (1992) have shown that the model spectrum must be used to quantitatively predict weak scintillation. (Weak scintillation refers to the case of irradiance fluctuations much less than the mean irradiance and has a well-known theory.) Recently, comparison of experimental data by Consortini et al. (1993) with data from numerical simulation of wave propagation by Flatté et al. (1993) has shown that the model is necessary to quantitatively predict strong scintillation from atmospheric propagation. Importantly, no alteration of the model's parameters from the values established by Hill (1978b) was made (or necessary) for these model verifications. These stringent tests give confidence that the model produces quantitatively correct spectra of advected scalars.

Hill (1978c) demonstrated that the turbulence advection model applies to the cospectrum of two scalar quantities advected by the same turbulent flow. This is important because the simultaneous conservation equations for the various ionization constituents (such as electrons, positive ions, aerosols, temperature, etc.) give rise to coupled equations for the power spectra of the scalars and the cospectra of pairs of the scalars. The coupling arises because of the coupled nature of the multiconstituent ionization diffusion equations (coupled because of the ambipolar electric field), or because of the coupled nature of the photochemical rate equations, or both. Thus, the ability to calculate cospectra is essential and available. The fact that the turbulent-advection model has the ability to calculate spectra and cospectra for the case of scalars that have coupled equations is the advection model's essential advantage over a formula for a given scalar's spectrum that fits data for that one spectrum. The turbulent advection of the photochemically coupled upper D-region, including ambipolar diffusion and diffusion of heat and nitric oxide, has been modeled by Hill (1981). In that study, nitric oxide NO, its ion NO<sup>+</sup>, electrons, and temperature (because of the temperature dependence of the recombination rate of NO<sup>+</sup> with electrons) were considered, yielding six coupled equations for spectra and cospectra.

The Obukhov-Corrsin constant  $\beta$  is the proportionality constant in the inertial-convective range;  $\beta$  relates spectra and cospectra to their corresponding dissipation rates. Hill (1989) showed that  $\beta$  has the same value for all spectra and cospectra; thus, a single empirical value of  $\beta$

can be used with confidence for all the spectra and cospectra. This is important because it gives confidence to our ability to relate spectral and cospectral levels to the dissipation rates determined by the numerical simulations of gravity-wave breaking and Kelvin-Helmholtz instability. Either of these spectral and cospectral levels or the dissipation rates are the quantities needed to initialize the turbulence advection model.

Hill (1978b) compared the spectral models with data from high Reynolds number turbulent flow. For application to the lower ionosphere, it is of interest to compare the models with data from moderate Reynolds number turbulence because it is likely that turbulence in the mesosphere has moderate-to-low Reynolds numbers. Bogucki et al. (1997) have made relevant comparisons of models with numerical simulations for moderate Reynolds number. Their comparisons of their spectra with Kraichnan's (1968) and Batchelor's (1959) theories are, in essence, comparisons with model 4 and model 2 by Hill (1978b), respectively. Bogucki et al. (1997) showed that the same models and values of the models' parameters that apply at very high Reynolds numbers also apply equally well at moderate Reynolds numbers. They also showed better agreement of data with Kraichnan's theory than with Batchelor's theory, which agrees with the comparison with data by Hill (1978b). This fact is also confirmed by Chasnov (1998), who used numerical simulation of turbulence in two-dimensional space which he compared with both Batchelor's theory and Kraichnan's theory for the viscous-convective and viscous-diffusive ranges.

Despite the superiority of model 4 over model 2, model 2 is used in this study (see section 6). The reason is that model 4, and hence also Kraichnan's theory, must be integrated from high wavenumbers toward low wavenumbers; otherwise, there is numerical swamping from the unwanted solution of the second-order differential equation. Because of the complexity of the diffusive ranges of the ions, it seems extremely difficult to derive the boundary conditions at high wavenumbers that are needed to initialize the calculation of model 4.

For the diffusive ranges, the ambipolar electric field causes complicated coupling of all the ions, which, in turn, results in complicated relationships between dissipation rates and diffusive-range spectral levels. The direct numerical simulation provides the dissipation rates of uncoupled passive scalars. These dissipation rates can be used to calculate the boundary conditions in the inertial-convective range for the purpose of integrating the equations toward high wavenumbers. Model 2 is the expedient model for this purpose because, unlike model 4, there is no difficulty in integrating model 2 toward high wavenumbers.

In section 6.3 we consider modeling nonstationary turbulence advection. In this case there exists temporal dependency of the energy-dissipation rate and the dissipation rates of scalar variance and covariance. Independently, Chasnov (1998) derived similar equations to those that

we obtain in section 6.3. We discuss the relationship between his result and ours in section 6.3. He considered the case of the viscous-convective and viscous-diffusive range of a single scalar. In contrast, we include the inertial-convective range and the transition between the inertial-convective range and the two viscous ranges, and we consider the more complicated case of coupled scalars. An important feature of Chasnov's (1998) study is his comparison of the nonstationary model with data obtained from calculations of two-dimensional turbulence. The good agreement of the model with the data that he obtained gives us confidence in our treatment of the nonstationary case.

## 2. EQUATIONS FOR PLASMA DYNAMICS COUPLED TO HYDRODYNAMIC TURBULENCE

To treat the turbulent advection of ionization, it is necessary to derive continuity equations for the charged species. This investigation uses the multifluid continuum momentum and the continuity equations of plasma dynamics. The continuum equations are obtained by multiplying the Boltzmann equation by powers of the particle velocities and averaging (Holt and Haskell, 1965). This produces an infinite hierarchy of coupled equations that requires a closure hypothesis. This study uses the isotropic, isothermal closure for the particle pressures. The time scales involved in turbulent advection are much longer than the thermal-relaxation time for the species considered. Therefore, the charged species have temperatures equal to the local atmospheric temperature throughout the advection process, and gradients in the temperature of a charged species exist only if a gradient exists in the atmospheric temperature. The thermal-diffusion effect due to local gradients in the atmospheric temperature is negligible.

Hill (1979) derived equations for multiconstituent plasma, including the effects of the magnetic field and motions of the neutral gas and showed that the magnetic field could be neglected for application to the lower ionosphere provided that the spatial extent of the fluctuations was not too great. Excluding the magnetic field, and without simplifying the pressure term, equation (8) by Hill (1979) is

$$m_\alpha \mathbf{v}_\alpha \cdot \nabla \mathbf{v}_\alpha + m_\alpha (\nabla \cdot \mathbf{v}_\alpha) \mathbf{v}_\alpha = -N_\alpha m_\alpha (\mathbf{a} - \mathbf{g}) + N_\alpha q_\alpha \mathbf{E} - \nabla P_\alpha . \quad (1)$$

The continuity equation (2) by Hill (1979) is

$$\frac{\partial N_\alpha}{\partial t} + \nabla \cdot (N_\alpha \mathbf{v}_\alpha) = Z_\alpha - L_\alpha . \quad (2)$$



Our notation list is:

$N_\alpha$  is the concentration of species  $\alpha$

$N$  is the concentration of neutral gas

$Q_\alpha = N_\alpha/N$  is the mixing ratio of species  $\alpha$

$P_\alpha$  is the pressure of species  $\alpha$

$P$  is atmospheric pressure, both hydrostatic and dynamical

$T_\alpha$  is the temperature in energy units of species  $\alpha$ ;  $T_\alpha = T$  because of thermal equilibrium

$T$  is the absolute temperature of the neutral gas in energy units; that is,

absolute temperature multiplied by Boltzmann's constant

$\underline{V}_\alpha$  is the velocity of species  $\alpha$

$\underline{V}$  is velocity of the neutral gas

$\underline{v}_\alpha = \underline{V}_\alpha - \underline{V}$  is the velocity of species  $\alpha$  relative to the neutral gas

$\underline{\Gamma}_\alpha = N_\alpha \underline{v}_\alpha$  is the flux of species  $\alpha$  relative to the neutral gas

$\underline{E}$  is the total electric field

$\underline{g}$  is acceleration due to gravity

$\underline{a}$  is acceleration of the neutral gas

$q_\alpha$  is the charge of species  $\alpha$

$e$  is the elementary unit of charge, i.e., the magnitude of the electron's charge

$S_\alpha \equiv q_\alpha/e$  is the charge number (including the sign) of species  $\alpha$

$m_\alpha$  is the mass of species  $\alpha$

$m$  is the mass of neutral molecules

$\nu_\alpha$  is the momentum-transfer collision rate for species  $\alpha$

$\mu_\alpha = \frac{q_\alpha}{m_\alpha \nu_\alpha}$  is the mobility of species  $\alpha$

$D_\alpha = \frac{T}{m_\alpha v_\alpha}$  is the diffusion coefficient of the concentration of species  $\alpha$

$\mathcal{D}_\alpha = \frac{P}{m_\alpha v_\alpha} = ND_\alpha$  is a diffusion coefficient of the mixing ratio  $Q_\alpha$

$Q = \sum_\alpha q_\alpha Q_\alpha$  is the mixing ratio of net charge density

$\tilde{J} = \sum_\alpha q_\alpha \tilde{\Gamma}_\alpha$  is the current density relative to the flow of neutral gas

$\lambda_\alpha^2 = \frac{T}{4\pi N_\alpha q_\alpha^2}$  is the square of the Debye length of species  $\alpha$

$\varepsilon$  is energy-dissipation rate per unit of mass of fluid

$\nu$  is kinematic viscosity

$\eta = (\nu^3/\varepsilon)^{1/4}$  is Kolmogorov's microscale

$\chi_{\alpha\gamma}$  is the rate of dissipation of mixing-ratio covariance or, for  $\alpha = \gamma$ , of mixing-ratio variance

$Z_\alpha$  is the photochemical production rate of species  $\alpha$

$L_\alpha$  is the photochemical loss rate of species  $\alpha$

The task at hand is to express (1) and (2) in terms of quantities that are conserved following the fluid motion when production, loss, diffusion, and external forces are all ignored. The quantity chosen is the mixing ratio  $Q_\alpha$ :

$$Q_\alpha = N_\alpha/N . \quad (3)$$

The particle pressure is given by (Hill, 1979)

$$P_\alpha = N_\alpha T_\alpha = N_\alpha T = Q_\alpha P , \quad (4)$$

where we used the ideal gas law,

$$P = NT , \quad (5)$$

for the neutral air. Performing the gradient of (4), we have

$$\underline{\nabla} P_\alpha = P \underline{\nabla} Q_\alpha + Q_\alpha \underline{\nabla} P . \quad (6)$$

For high Reynolds number turbulence, the flow's acceleration  $\underline{a}$  is dominated by the pressure gradient  $\underline{\nabla} P$ . That is, the acceleration by the viscous force is negligible (Hill and Thoroddsen, 1997). Moreover,  $\underline{\nabla} P$  has a hydrostatic mean value balancing gravity. Thus,

$$\underline{\nabla} P = -Nm (\underline{a} - \underline{g}) . \quad (7)$$

The second term on the left-hand side (lhs) of (1) is negligible (in comparison with the first term) because velocity gradients are much smaller than the collision frequency,  $v_\alpha$ . Neglecting that second term and substituting (6) and (7) in (1) gives

$$m_\alpha v_\alpha \underline{\Gamma}_\alpha = -N_\alpha (m_\alpha - m) (\underline{a} - \underline{g}) + N_\alpha q_\alpha \underline{E} - P \underline{\nabla} Q_\alpha . \quad (8)$$

The terms in this equation represent the effects of collisional drag on the left side and buoyancy, electric field, and diffusion on the right side.

The buoyancy term is clearly expressed in (8). Introducing the mixing ratio  $Q_\alpha$  resulted in this clarity because part of the buoyancy term was previously hidden in the term  $-\underline{\nabla} P_\alpha$  in (1). In the following, we neglect the buoyancy term.

The concentration of neutral molecules obeys

$$\frac{\partial N}{\partial t} + \underline{\nabla} \cdot (N \underline{V}) = 0 . \quad (9)$$

Combining (2) and (9), we have

$$\frac{\partial Q_\alpha}{\partial t} + \underline{V} \cdot \underline{\nabla} Q_\alpha = -\frac{1}{N} (\underline{\nabla} \cdot \underline{\Gamma}_\alpha + Z_\alpha - L_\alpha) . \quad (10)$$

No approximation is used to obtain (10) from (2) and (9); in particular, incompressibility was not used.

### 3. PLASMA ADVECTION WITH DIFFUSION

The production,  $Z_\alpha$ , and loss,  $L_\alpha$ , are neglected from (10), and the buoyancy term is neglected from (8). Our equations are

$$m_\alpha v_\alpha \cdot \nabla_\alpha = N_\alpha q_\alpha \underline{E} - P \nabla Q_\alpha \quad (11)$$

and

$$\frac{DQ_\alpha}{Dt} \equiv \frac{\partial Q_\alpha}{\partial t} + \underline{v} \cdot \nabla Q_\alpha = -\frac{1}{N} \nabla \cdot \underline{\Gamma}_\alpha, \quad (12)$$

where  $D/Dt$  signifies the time derivative following the neutral gas. These equations are nonlinear because  $\underline{E}$  satisfies Poisson's equation,

$$\nabla \cdot \underline{E} = 4\pi \sum_\beta q_\beta N_\beta. \quad (13)$$

Eliminating  $\underline{E}$  leads to complicated nonlinear terms on the right-hand side (rhs) of (12). Numerical solution is needed for these nonlinear equations.

Equations (11)–(13) describe many phenomena having wide ranges of time and space scales. Solutions of these equations given by Hill and Bowhill (1977a) include collisional damping of species velocities, free electron diffusion, collisionally damped space charge waves, free ion diffusion, and ambipolar diffusion. The temporal frequencies for these phenomena in the  $D$  region as given by Hill and Bowhill (1977a) range from  $10^8$  to  $10^{-3} \text{ s}^{-1}$ . Here, we are interested only in the lowest-frequency phenomena, which are diffusion phenomena. The diffusion phenomena are ambipolar diffusion and nearly free ion diffusion. The number of such diffusion modes equals the number of ion species.

Dividing (11) by  $m_\alpha v_\alpha$  and performing the divergence gives

$$\nabla \cdot \underline{\Gamma}_\alpha = N_\alpha \mu_\alpha \nabla \cdot \underline{E} + \nabla (N_\alpha \mu_\alpha) \cdot \underline{E} - \nabla \cdot (\mathcal{D}_\alpha \nabla Q_\alpha). \quad (14)$$

This is the divergence needed in (12). Multiplying (12) and (14) by  $q_\alpha$ , summing over  $\alpha$ , and defining, for simplicity,

$$C \equiv \sum_{\alpha} q_{\alpha} N_{\alpha} \mu_{\alpha} \quad (15a)$$

and

$$\underline{\Psi} \equiv \sum_{\alpha} q_{\alpha} \mathcal{D}_{\alpha} \underline{\nabla} Q_{\alpha} , \quad (15b)$$

we have from (14),

$$\underline{\nabla} \cdot \underline{J} = C \underline{\nabla} \cdot \underline{E} + (\underline{\nabla} C) \cdot \underline{E} - \underline{\nabla} \cdot \underline{\Psi} , \quad (16)$$

and from (12),

$$\frac{DQ}{Dt} = -\frac{1}{N} \underline{\nabla} \cdot \underline{J} , \quad (17)$$

where  $Q$  is the charge mixing ratio and  $\underline{J}$  is the current density relative to the flow of the neutral gas. Multiplying (11) by  $\mu_{\alpha}$  and summing, we can obtain the current density relative to the neutral gas,

$$\underline{J} = C \underline{E} - \underline{\Psi} . \quad (18)$$

Of course, the divergence of (18) is (16). In (18),  $C$  has the appearance of a conductivity; that is, current flowing in response to the electric field, as in  $\underline{J} = C \underline{E}$ . However, in plasma diffusion the electric field retards the diffusion of some species and enhances the motion of other species such that little charge develops and little current flows. That is,  $\underline{J}$  is negligible compared with the terms on the rhs of (18), in which case  $\underline{J} = 0$  substituted in (18) gives the approximation to the electric field

$$\underline{E} = \underline{\Psi}/C = 4\pi N \sum_{\alpha} q_{\alpha} W_{\alpha} \underline{\nabla} Q_{\alpha} , \quad (19)$$

where

$$W_{\alpha} \equiv \left[ \sum_{\beta} \lambda_{\beta}^{-2} \frac{m_{\alpha} v_{\alpha}}{m_{\beta} v_{\beta}} \right]^{-1}$$

is a weighted harmonic mean of Debye lengths squared. Now (19) is valid even in a plasma devoid of electrons. If the electron density and its gradient are not too small, then the electron's

term dominates the sums in  $\Psi$  and  $C$  because the electron's mobility is greater than any ion's mobility by many orders of magnitude. Then

$$\Psi \approx -e \mathcal{D}_e \nabla Q_e, \quad (20a)$$

$$C \approx -e N_e \mu_e, \quad (20b)$$

and (19) becomes

$$\underline{E} \approx \frac{\mathcal{D}_e}{N_e \mu_e} \nabla Q_e = \frac{P}{-e N_e} \nabla Q_e = 4\pi N(-e) \lambda_e^2 \nabla Q_e, \quad (21)$$

which is essentially equation (24) by Hill (1978a). The divergence (14) can be expressed in terms of gradients by using (19) to eliminate the electric field; then (12) becomes

$$\frac{\partial Q_a}{\partial t} + \underline{V} \cdot \nabla Q_a = -\frac{1}{N} \left[ \nabla \cdot (N_a \mu_a \Psi / C) - \nabla \cdot (\mathcal{D}_a \nabla Q_a) \right], \quad (22)$$

which constitutes a set of coupled nonlinear equations. The coupling is through the summations of (15a,b) defining  $\Psi$  and  $C$ .

A simpler set of equations results when there are a sufficient number of electrons such that (21) is accurate. Now (21) is essentially (11) for the electrons with the lhs neglected. For the low-frequency diffusion phenomena, Hill and Bowhill (1977a) showed that only the electric field and diffusion terms in (11) are important for the electrons; the collisional drag on the electrons may be neglected. That is, because the electrons are by far the most mobile species (by orders of magnitude), the electrons enforce charge neutrality to the extent permitted by their diffusion. However, according to (11), the approximation (21) is equivalent to  $\underline{\Gamma}_e = 0$ , which means that  $Q_e$  cannot be determined from (12). Instead,  $Q_e$  will be obtained from Poisson's equation (13). The physics and method of non-neutral multiconstituent diffusion obtained by Hill (1978a) is essentially the same as described above, although we have generalized the theory because (19) and (22) apply even if the plasma is devoid of electrons.

#### 4. PERTURBATION ANALYSIS

To render the equations tractable, a perturbation analysis is used, by means of which the nonlinear equations are approximated by linear equations. We introduce ambient and perturbation fluxes relative to the neutral gas,

$$\Gamma_\alpha = \Gamma_\alpha^o + \Gamma_\alpha' . \quad (23)$$

Superscript  $o$  indicates an ambient quantity, and prime indicates a perturbation quantity. Transport coefficients (e.g.,  $v_\alpha$ ,  $D_\alpha$ ,  $\mathcal{D}_\alpha$ ) depend on the hydrodynamic variables ( $T$ ,  $P$ ,  $N$ ), fluctuations of which cause, through (11) and (12), fluctuations in  $\Gamma_\alpha$  and  $N_\alpha$ . Therefore, linearization must include the hydrodynamic variables by use of

$$\begin{aligned} T &= T^o + T' \\ N &= N^o + N' . \end{aligned}$$

In doing so, we ignore pressure fluctuations,  $P'$ . At the large wavenumbers ( $k$ ) of interest (i.e., wavenumbers in the inertial-convective range and higher), the pressure spectrum falls much faster than that of conserved scalars (e.g., as  $k^{-7/3}$  versus  $k^{-5/3}$  for an inertial range). Thus,  $P'$  can be safely ignored.

The Appendix shows that  $v_\alpha$  is proportional to the product of  $P$  and a function of  $T$ . From its definition,  $\mathcal{D}_\alpha$  is thus a function of  $T$  and is independent of  $P$ . Therefore,

$$\mathcal{D}_\alpha = \mathcal{D}_\alpha^o + \mathcal{D}_\alpha' = \mathcal{D}_\alpha^o + \frac{d\mathcal{D}_\alpha}{dT} T' , \quad (24)$$

where  $\mathcal{D}_\alpha^o$  is the value at  $T^o$ , and the right-most expression follows from the Taylor series expansion. We define a dimensionless coefficient as

$$c_{v\alpha} \equiv \left. \frac{T^o}{v_\alpha^o} \frac{\partial v_\alpha^o}{\partial T^o} \right)_P = - \frac{T^o}{\mathcal{D}_\alpha^o} \frac{d\mathcal{D}_\alpha^o}{dT^o} \quad (25)$$

in terms of which (24) becomes

$$\mathcal{D}_\alpha = \mathcal{D}_\alpha^o \left( 1 - c_{va} \frac{T'}{T^o} \right). \quad (26)$$

We divide (11) by  $m_\alpha v_\alpha$  and substitute (21) for  $\underline{E}$  to obtain

$$\underline{\Gamma}_\alpha = N_\alpha \mu_\alpha \frac{P}{-e N_e} \underline{\nabla} Q_e - \mathcal{D}_\alpha \underline{\nabla} Q_\alpha. \quad (27)$$

Substituting the ambient and fluctuating quantities in the first term of (27), we have to first order,

$$\begin{aligned} N_\alpha \mu_\alpha \frac{P}{-e N_e} \underline{\nabla} Q_e &= -S_\alpha \mathcal{D}_\alpha \left( \frac{Q_\alpha}{Q_e} \right) \underline{\nabla} Q_e \\ &= -S_\alpha \mathcal{D}_\alpha^o \left( \frac{Q_\alpha^o}{Q_e^o} \right) \underline{\nabla} Q_e^o \left\{ 1 + \frac{\underline{\nabla} Q_e'}{\underline{\nabla} Q_e^o} + \frac{(Q_\alpha/Q_e)'}{(Q_\alpha^o/Q_e^o)} - c_{va} \frac{T'}{T^o} \right\}. \end{aligned} \quad (28)$$

From left to right, the terms in the brackets,  $\{\dots\}$ , are the ambient value associated with  $\underline{\Gamma}_\alpha^o$ , and the remaining terms are the fluctuations associated with  $\underline{\Gamma}_\alpha'$  and are of obvious origin, with the term proportional to  $c_{va}$  arising from fluctuations of  $\mathcal{D}_\alpha$ . The term  $\underline{\nabla} Q_e' / \underline{\nabla} Q_e^o$  is of the order of  $Q_e' / Q_e^o$  times the ratio of the large scale on which ambient quantities vary to the small scale on which diffusion is effective. In addition,  $c_{va}$  approaches zero as ion size increases. Therefore, the first fluctuation term,  $\underline{\nabla} Q_e' / \underline{\nabla} Q_e^o$ , is much greater than the other terms.

We now turn to the diffusion term in (27). To first order, it is

$$\mathcal{D}_\alpha \underline{\nabla} Q_\alpha = \mathcal{D}_\alpha^o \left\{ \underline{\nabla} Q_\alpha^o + \underline{\nabla} Q_\alpha' - c_{va} \frac{T'}{T^o} \underline{\nabla} Q_\alpha^o \right\}. \quad (29)$$

The ambient and perturbation electric fields are

$$\underline{E}^o = \frac{P}{-e N_e^o} \underline{\nabla} Q_e^o \quad (30)$$



$$\underline{\underline{E}}' = \frac{P}{-e N_e^o} \underline{\underline{\nabla}} Q_e' - \frac{N_e'}{N_e^o} \underline{\underline{E}}^o . \quad (31)$$

Applying ambient and fluctuating quantities in (12) and subtracting the ambient equation, we have to first order,

$$\frac{DQ_a'}{Dt} = -\frac{1}{N^o} \left\{ \underline{\underline{\nabla}} \cdot \underline{\underline{\Gamma}}_a' + \frac{T'}{T^o} \underline{\underline{\nabla}} \cdot \underline{\underline{\Gamma}}_a^o \right\} , \quad (32)$$

where, from (23), (27), and (30), we have

$$\underline{\underline{\Gamma}}_a^o = N_a^o \mu_a^o \underline{\underline{E}}^o - \mathcal{D}_a^o \underline{\underline{\nabla}} Q_a^o \quad (33a)$$

$$\underline{\underline{\Gamma}}_a^o = -\mathcal{D}_a^o \underline{\underline{\Xi}}_a^o , \quad (33b)$$

where we have defined, for notational simplicity,

$$\underline{\underline{\Xi}}_a^o \equiv S_a \frac{Q_a^o}{Q_e^o} \underline{\underline{\nabla}} Q_e^o + \underline{\underline{\nabla}} Q_a^o . \quad (34)$$

We substituted (30) into (33a) to obtain (33b). The perturbation flux relative to the air flow is obtained from (28) minus (29), which gives

$$\underline{\underline{\Gamma}}_a' = -S_a \mathcal{D}_a^o \frac{Q_a^o}{Q_e^o} \underline{\underline{\nabla}} Q_e' - \mathcal{D}_a^o \underline{\underline{\nabla}} Q_a' - S_a \mathcal{D}_a^o (\underline{\underline{\nabla}} Q_e^o) \left( \frac{Q_a}{Q_e} \right)' + \mathcal{D}_a^o \underline{\underline{\Xi}}_a^o c_{va} \frac{T'}{T^o} . \quad (35)$$

The divergence of (33b) is

$$\underline{\underline{\nabla}} \cdot \underline{\underline{\Gamma}}_a^o = -\mathcal{D}_a^o \underline{\underline{\nabla}} \cdot \underline{\underline{\Xi}}_a^o - \underline{\underline{\Xi}}_a^o \cdot \underline{\underline{\nabla}} \mathcal{D}_a^o . \quad (36)$$

From (34) we obtain

$$\underline{\nabla} \cdot \underline{\Xi}_\alpha^o = S_\alpha \left( \underline{\nabla} \frac{Q_\alpha^o}{Q_e^o} \right) \cdot (\underline{\nabla} Q_e^o) + S_\alpha \frac{Q_\alpha^o}{Q_e^o} \nabla^2 Q_e^o + \nabla^2 Q_\alpha^o.$$

For use in (36), we have from (25) that

$$\underline{\nabla} \mathcal{D}_\alpha^o = -c_{v\alpha} \mathcal{D}_\alpha^o \frac{\underline{\nabla} T^o}{T^o}. \quad (37)$$

We also define

$$c'_{v\alpha} \equiv \frac{T^{o2}}{v_\alpha^o} \frac{\partial^2 v_\alpha^o}{\partial T^{o2}} \Big|_P. \quad (38)$$

To simplify notation, we define

$$\Omega_\alpha^o \equiv \frac{D_\alpha^o}{T^o} \left[ (1 - c_{v\alpha}) \underline{\nabla} \cdot \underline{\Xi}_\alpha^o + (2c_{v\alpha}^2 - c_{v\alpha} - c'_{v\alpha}) \underline{\Xi}_\alpha^o \cdot \frac{\underline{\nabla} T^o}{T^o} \right] \quad (39)$$

$$\Upsilon_\alpha^o \equiv c_{v\alpha} \frac{D_\alpha^o}{T^o} \underline{\Xi}_\alpha^o. \quad (40)$$

Clearly,  $\Omega_\alpha^o$  and  $\Upsilon_\alpha^o$  are to be calculated from ambient conditions. Note that  $c_{v\alpha}$  and  $c'_{v\alpha}$  are functions of  $T^o$  and are not functions of  $P$ .

When the divergence of (35) is performed, there are gradient terms proportional to  $\underline{\nabla} Q_e'$ ,  $\underline{\nabla} Q_\alpha'$ , and  $\underline{\nabla} (Q_\alpha/Q_e)'$ . Those terms vanish at a subsequent step where we average over an isotropic ensemble; this will be made evident by retaining the term proportional to  $\underline{\nabla} T'$ . Moreover, relative to terms proportional to  $\nabla^2 Q_e'$  and  $\nabla^2 Q_\alpha'$ , these gradient terms are of the order of the ratio of the small scale on which diffusion is effective to the large scale on which the ambient quantities vary. Consequently, we neglect these gradient terms. Also, a term proportional to  $(Q_\alpha/Q_e)'$  arises from the divergence of (35). This term is of the order of the square of the aforementioned scale ratio relative to terms proportional to  $\nabla^2 Q_e'$  and  $\nabla^2 Q_\alpha'$ . Consequently, we neglect the term proportional to  $(Q_\alpha/Q_e)'$ . With the aforementioned approximations, we substitute the divergence of (35) and (36) into (32) to obtain

$$\frac{DQ_\alpha'}{Dt} = S_\alpha D_\alpha^o \frac{Q_\alpha^o}{Q_e^o} \nabla^2 Q_e' + D_\alpha^o \nabla^2 Q_\alpha' - \Upsilon_\alpha^o \cdot \underline{\nabla} T' + T' \Omega_\alpha^o. \quad (41)$$

The next step is to use Poisson's equation to obtain an expression for  $Q'_e$  and eliminate  $Q'_e$  from (41). The spatial Fourier transform is needed for this step. From Poisson's equation (13), after division by  $N^o$ , we have to first order,

$$\frac{T^o}{-e N_e^o} \left( \nabla^2 Q'_e + \frac{N'_e}{N_e^o} \frac{\nabla N_e^o}{N_e^o} \cdot \nabla Q'_e \right) = 4\pi \sum_{\beta} q_{\beta} Q'_{\beta} . \quad (42)$$

On the rhs of (42), we have used the fact that to first order,  $Q'_{\beta} = N'_{\beta}/N^o + N_{\beta}^o (T'/T^o N^o)$ , such that

$$\sum_{\beta} q_{\beta} Q'_{\beta} = \frac{1}{N^o} \sum_{\beta} q_{\beta} N'_{\beta} + \left( \frac{T'}{T^o N^o} \right) \sum_{\beta} q_{\beta} N_{\beta}^o ,$$

and that the right-most term above vanishes by charge neutrality. We neglected from the lhs of (42) terms containing  $\nabla Q'_e$  and  $\nabla N'_e$ ; as is the case with (41), these terms vanish at a later stage when an average over an isotropic ensemble is performed. Dividing by  $4\pi e$  and adding  $Q'_e$  to both sides, (42) gives

$$Q'_e - \lambda_e^2 \left( \nabla^2 Q'_e + \frac{N'_e}{N_e^o} \frac{\nabla N_e^o}{N_e^o} \cdot \nabla Q'_e \right) = \sum_{\beta \neq e} S_{\beta} Q'_{\beta} , \quad (43)$$

where we have recognized the electron Debye length,  $\lambda_e$ . The subscript  $\beta \neq e$  indicates summation over all the ions. Next, the Fourier transform is applied; in so doing, only fluctuating quantities are transformed, and quantities that depend only on ambient values are treated as constants. A quantity in French braces  $\{ \}$  indicates the Fourier transform of the quantity. The Fourier transform of (43) gives

$$\{Q'_e\} [1 + (k\lambda_e)^2] - \lambda_e^2 \frac{\{N'_e\}}{N_e^o} \frac{\nabla N_e^o}{N_e^o} \cdot \nabla Q'_e = \sum_{\beta \neq e} S_{\beta} \{Q'_{\beta}\} , \quad (44)$$

where  $\underline{k}$  is the wave vector and  $k$  is the wavenumber. The last term on the lhs is seen to be of the order of the square of  $\lambda_e$  divided by the scale height of  $N_e^o$  (i.e., roughly, the square of  $10^{-5}$ ) and is therefore neglected. Thus, we have

$$\{Q'_e\} = \frac{\sum_{\beta \neq e} S_{\beta} \{Q'_{\beta}\}}{1 + (k\lambda_e)^2} . \quad (45)$$

These equations express approximate charge neutrality, and (45) is essentially the same as equation (23) by Hill (1978a). The free diffusion of the electrons causes the charge neutrality to be only approximate. By free diffusion of electrons, we mean that their tendency to diffuse is counteracted only by the electric field and that the electron's collisional drag is unimportant. The denominator  $1 + (k\lambda_e)^2$  in (45) is the Debye shielding factor. The Fourier transform of (41) gives, after substitution of (45),

$$\begin{aligned} \frac{\partial \{Q'_\alpha\}}{\partial t} + \{\underline{V} \cdot \underline{\nabla} Q'_\alpha\} = & -k^2 D_\alpha^o \{Q'_\alpha\} - k^2 D_\alpha^o \frac{N_\alpha^o}{N_e^o} S_\alpha \frac{\sum_{\beta \neq e} S_\beta \{Q'_\beta\}}{1 + (k\lambda_e)^2} \\ & + \{T'\} i\vec{k} \cdot \underline{Y}_\alpha^o + \{T'\} \Omega_\alpha^o . \end{aligned} \quad (46)$$

Of course, (46) applies only for the ions, i.e.,  $\alpha \neq e$ . This constitutes coupled linear equations for the ions' mixing-ratio Fourier transforms. The electron's mixing-ratio transforms are subsequently obtained from those of the ions by use of (45). Without the terms proportional to  $\{T'\}$ , (46) is essentially equation (25) by Hill (1978a).

## 5. EQUATIONS FOR SPECTRA AND COSPECTRA

The next step is to use (46) to obtain equations for cospectra and autospectra (i.e., power spectra) of the mixing ratios. To do so, it is useful to choose the special coordinate system that is moving with the ambient velocity  $\underline{V}^o$ . There are two reasons for this. First, the turbulence advection model, as applied in section 6, pertains to the locally stationary case. We desire to apply the advection model for local volumes that are either radar-resolution volumes or a fraction thereof. If the turbulent medium is rapidly advected by velocity  $\underline{V}^o$  through the local volume under consideration, then local stationarity is inaccurate because regions of strong dissipation can be advected into or out of the local volume. Dissipation is highly intermittent at small scales in turbulent flow and becomes more intermittent as the Reynolds number increases. Thus, the smaller the local volume under consideration, the more rapidly the volume-averaged dissipation can change if dissipation structures are swept through the volume by an ambient flow velocity  $\underline{V}^o$ . Dissipation structures tend to move with the local flow, so the choice of the local coordinate system moving with the local flow velocity  $\underline{V}^o$  mitigates the effect of advecting dissipation structures. Therefore, we henceforth define the ambient velocity  $\underline{V}^o$  and all of the other ambient quantities (e.g.,  $T^o$ ,  $N_e^o$ , etc.) to be averages over the local volume of interest. Of course, these

ambient quantities change with time as the flow evolves. The second reason for the choice of coordinate system is that when we formulate the nonstationary case in section 6.3, we make an approximation [neglecting the time derivative of the scaled spectrum in (91)] that can be inaccurate unless the time derivative is taken for spatial coordinates fixed in the coordinate system moving with ambient velocity  $\underline{V}^o$ . That is, the advection of dissipation structures into or out of the local volume of interest can cause inaccuracy of the approximation in section 6.3. Therefore, all time derivatives in the equations for spectra and cospectra (as distinguished from the continuity equations) in the remainder of this report are with respect to the special coordinate system that moves with the local-volume-averaged ambient velocity.

The cospectrum is defined by

$$\Phi_{\alpha\gamma}(\underline{k}) \equiv \frac{1}{2} \left[ \{Q'_\gamma\}^* \{Q'_\alpha\} + \{Q'_\gamma\} \{Q'_\alpha\}^* \right] = \text{Re} \left[ \{Q'_\gamma\}^* \{Q'_\alpha\} \right], \quad (47)$$

where Re denotes the real part and the superscript asterisk denotes the complex conjugate. If  $\alpha = \gamma$ , then this definition gives the autospectrum:

$$\Phi_{\alpha\alpha}(\underline{k}) \equiv \text{Re} \left[ \{Q'_\alpha\}^* \{Q'_\alpha\} \right]. \quad (48)$$

In (47) and (48), the argument  $\underline{k}$  is a mnemonic for arguments  $\underline{k}_\alpha$  and  $\underline{k}_\gamma$ , which are the independent wave vectors for the Fourier transforms in (47). Namely, Fourier transforms  $\{Q'_\alpha\}$  and  $\{Q'_\alpha\}^*$  in (47) have  $\underline{k}_\alpha$  as their argument, and  $\{Q'_\gamma\}$  and  $\{Q'_\gamma\}^*$  have  $\underline{k}_\gamma$  as their argument. When we let  $\alpha = \gamma$  in (47) in order to obtain (48), one of the Fourier transforms [say,  $\{Q'_\alpha\}^*$  in (48)] retains  $\underline{k}_\gamma$  as its argument, while the other Fourier transform [say,  $\{Q'_\alpha\}$  in (48)] has  $\underline{k}_\alpha$  as its argument. Thus, we must take the real part in (48) because the two Fourier transforms have different arguments. The mnemonic that  $\underline{k}$  means dependence on two independent wave vectors applies to all subsequent equations where  $\underline{k}$  is the argument of a function symbolized by  $\Phi$  or by  $\mathcal{J}$ .

The cospectrum of potential temperature and mixing ratio is  
and the autospectrum of potential temperature is

$$\Phi_{\alpha T}(\underline{k}) \equiv \text{Re} \left[ \{T'\}^* \{Q'_\alpha\} \right], \quad (49)$$

To form equations for power spectra and cospectra, we multiply (46) by  $\{Q'_\gamma\}^*$  and add

$$\Phi_{TT}(\underline{k}) \equiv \text{Re} \left[ \{T'\}^* \{T'\} \right]. \quad (50)$$

the equation obtained by multiplying  $\{Q'_\alpha\}$  by the equation for  $\{Q'_\gamma\}^*$ ; this latter equation for  $\{Q'_\gamma\}^*$  is obtained from (46) by replacing  $\alpha$  with  $\gamma$  and obtaining the complex conjugate of the equation. To the resultant equation we add the complex conjugate of the resultant equation and divide by 2. The procedure gives

$$\begin{aligned} \frac{\partial \Phi_{\alpha\gamma}(\underline{k})}{\partial t} - \mathcal{J}_{\alpha\gamma}(\underline{k}) = & -k^2 (D_\alpha + D_\gamma) \Phi_{\alpha\gamma}(\underline{k}) \\ & - k^2 \sum_{\beta \neq e} \left[ c_{\alpha\beta}(k) \Phi_{\gamma\beta}(\underline{k}) + c_{\gamma\beta}(k) \Phi_{\alpha\beta}(\underline{k}) \right] \\ & + \left[ \Phi_{\alpha T}(\underline{k}) + \Phi_{\gamma T}(\underline{k}) \right] (i \underline{k} \cdot \underline{Y}_\alpha + \Omega_\alpha) , \end{aligned} \quad (51)$$

where we define the coefficient as

$$c_{\alpha\beta}(k) \equiv S_\alpha S_\beta D_\alpha \frac{N_\alpha}{N_e} \frac{1}{1 + (k\lambda_e)^2} \quad (52)$$

and  $\mathcal{J}_{\alpha\gamma}$  is the sum of all terms containing the fluctuations of the velocity of the neutral gas,  $\underline{V}' \equiv \underline{V} - \underline{V}^o$ ;  $\mathcal{J}_{\alpha\gamma}$  is known as a transfer spectrum. For simplicity, the superscript  $o$  has been deleted from the coefficients involving only ambient quantities. Next, we average over an isotropic ensemble of realizations (this average is denoted by angle brackets). Averaging over an isotropic ensemble (which is necessarily a homogeneous ensemble) requires the condition  $\underline{k}_\alpha = -\underline{k}_\gamma$  and also requires dependence on only the magnitude of the argument, namely,  $k = |\underline{k}_\alpha| = |-\underline{k}_\alpha|$ . Also, we integrate over spherical shells in wave vector space, which introduces a factor of  $4\pi k^2$ . The averaged and sphere-integrated spectrum depends only on  $k$  and is given by

$$\Gamma_{\alpha\gamma}(k) = 4\pi k^2 \langle \Phi_{\alpha\gamma}(\underline{k}) \rangle \quad (53a)$$

$$\mathcal{T}_{\alpha\gamma}(k) = 4\pi k^2 \langle \mathcal{J}_{\alpha\gamma}(\underline{k}) \rangle , \quad (53b)$$

with analogous relationships for  $\Gamma_{\alpha T}(k)$  and  $\Gamma_{TT}(k)$ . In terms of the mixing-ratio covariance,  $\Gamma_{\alpha\gamma}(k)$  is given by

$$\Gamma_{\alpha\gamma}(k) = \iint k^2 d\Omega_k \iiint \frac{d^3r}{(2\pi)^3} \langle Q_\alpha(\underline{x}) Q_\gamma(\underline{x} + \underline{r}) \rangle \exp(-i\mathbf{k} \cdot \underline{r}) ,$$

where  $d\Omega_k$  is the differential solid angle in  $\underline{k}$ -space. Thus, the cospectrum is normalized such that

$$\langle Q_\alpha(\underline{x}) Q_\gamma(\underline{x}) \rangle = \int_0^\infty \Gamma_{\alpha\gamma}(k) dk .$$

That is,  $\Gamma_{\alpha\gamma}(k)$  is the wavenumber budget of the single-point covariance, and for  $\alpha = \gamma$ ,  $\Gamma_{\alpha\alpha}(k)$  is the wavenumber budget of mean-squared mixing-ratio fluctuations of species  $\alpha$ .

Applying the averaging operation to (51), we obtain

$$\begin{aligned} \frac{\partial \Gamma_{\alpha\gamma}(k)}{\partial t} - \mathcal{T}_{\alpha\gamma}(k) = & -k^2 (D_\alpha + D_\gamma) \Gamma_{\alpha\gamma}(k) \\ & - k^2 \sum_{\beta \neq \epsilon} [c_{\alpha\beta}(k) \Gamma_{\gamma\beta}(k) + c_{\gamma\beta}(k) \Gamma_{\alpha\beta}(k)] \\ & + \Omega_\alpha [\Gamma_{\alpha T}(k) + \Gamma_{\gamma T}(k)] . \end{aligned} \quad (54)$$

The term containing  $\underline{k} \cdot \underline{Y}_\alpha$  vanishes on averaging over an isotropic ensemble because  $\underline{Y}_\alpha$  has a fixed direction, whereas  $\underline{k}$  takes on all directions.

## 6. APPLICATION OF THE TURBULENCE ADVECTION MODEL

### 6.1 Locally Stationary Case With No Coupling to Temperature Fluctuations

For simplicity and clarity, we begin with the locally stationary case, such that the time derivative is neglected, and also neglect the coupling to  $T'$  by setting  $\Omega_\alpha = 0$ . We return to those cases in subsequent sections.

We use a spectral transfer function from the model by Hill and Bowhill (1976) that was refined and compared with data by Hill (1978b). That comparison with data shows that this model accurately gives the wavenumber position and breadth of the transition between inertial-convective and viscous-convective ranges. Such a model was first demonstrated to be capable of

computing cospectra by Hill (1978c). The model was first used to calculate coupled equations by Hill (1981), where the coupling was caused by photochemistry and ambipolar diffusion. It is the ability of the spectral transfer model to produce spectra and cospectra for the case of coupled equations that is its essential advantage over a formula for a given spectrum that fits data for that one spectrum.

The spectral transfer model by Hill and Bowhill (1976) with its parameters  $[(k^*\eta)$  and  $a]$  determined by Hill (1978b) is used; it is

$$-T_{\alpha\gamma}(k) = \frac{d[s(k) \Gamma_{\alpha\gamma}(k)]}{dk}, \quad (55)$$

$$s(k) \equiv \beta^{-1} \varepsilon^{1/3} k^{5/3} [(k/k^*)^{2a} + 1]^{-1/(3a)}, \quad (56)$$

where  $\beta$  is the Obukhov-Corrsin constant, and

$$k^*\eta = 0.074 \quad \text{and} \quad a = 1.4. \quad (57)$$

Equation (54) is recast in terms of the dimensionless spectra and cospectra as defined by

$$G_{\alpha\gamma}(x) \equiv \frac{s(k) \Gamma_{\alpha\gamma}(k)}{\chi_{\alpha\gamma}} \quad (58)$$

and the dimensionless wavenumber as defined by

$$x \equiv k\eta. \quad (59)$$

The  $\chi_{\alpha\gamma}$  are the cospectral dissipation rates. We define  $F(x)$  such that, from (56),

$$s(x) = \frac{\beta^{-1} \varepsilon^{1/3} \eta^{-5/3}}{F(x)} \quad (60)$$



and

$$F(x) \equiv x^{-5/3} \left[ (x/(k^* \eta)^{2a} + 1) \right]^{+1/(3a)} . \quad (61)$$

In an inertial-convective range, wherein  $k \ll k^*$ ,

$$\Gamma_{\alpha\gamma}(k) \approx \beta \varepsilon^{-1/3} \chi_{\alpha\gamma} k^{-5/3} , \quad (62)$$

so

$$G_{\alpha\gamma}(x) \approx 1.0 \quad (63)$$

is the boundary condition at small  $x$ . In terms of  $G_{\alpha\gamma}(x)$ , (54) becomes [one must divide (54) by  $\eta \chi_{\alpha\gamma}$ , neglect the time-dependent term, and set  $\Omega_\alpha = 0$ ]

$$\frac{dG_{\alpha\gamma}(x)}{dx} = -x^2 P_{\alpha\gamma} F(x) \left\{ G_{\alpha\gamma}(x) + \left[ 1 + (x\lambda_e/\eta)^2 \right]^{-1} \sum_{\beta \neq e} \left[ c_{\alpha\gamma\beta} G_{\gamma\beta}(x) + c_{\gamma\alpha\beta} G_{\alpha\beta}(x) \right] \right\} , \quad (64)$$

where we have organized a coefficient that can be precomputed from ambient quantities, namely,

$$c_{\alpha\gamma\beta} \equiv S_\alpha S_\beta \frac{D_\alpha}{D_\alpha + D_\gamma} \frac{N_\alpha}{N_e} \frac{\chi_{\gamma\beta}}{\chi_{\alpha\gamma}} , \quad (65)$$

and one of many Schmidt numbers,

$$P_{\alpha\gamma} \equiv \beta \frac{(D_\alpha + D_\gamma)}{\nu} . \quad (66)$$

Given values for  $c_{\alpha\gamma\beta}$ ,  $P_{\alpha\gamma}$ , and  $\lambda_e/\eta$  and using the initial condition (63), (64) constitutes coupled, linear, first-order differential equations that can be integrated toward and through

dissipation wavenumbers by means of a predictor-corrector algorithm. Recall that

$G_{\alpha\gamma}(x) = G_{\gamma\alpha}(x)$ ; therefore, the number of independent  $G_{\alpha\gamma}(x)$  and the number of independent equations is  $n(n+1)/2$ , where  $n$  is the number of ion species.

## 6.2 Locally Stationary Case With Coupling to Temperature Fluctuations

Next, we turn to the locally stationary case with nonzero  $\Omega_\alpha$ . Recall that  $\Gamma_{\alpha T}(k)$  is a cospectrum of potential temperature and ion-concentration mixing ratio. As with  $G_{\alpha\gamma}(k)$ , we define

$$G_{\alpha T}(x) = \frac{s(k) \Gamma_{\alpha T}(k)}{\chi_{\alpha T}}, \quad (67)$$

where  $\chi_{\alpha T}$  is the dissipation rate of the covariance of potential temperature and ion-concentration mixing ratio. Following from (54), an additional term must be added to the rhs of (64). The additional term is

$$\text{TERM} \equiv +F(x) \left[ B_{\alpha T\gamma} G_{\alpha T}(k) + B_{\gamma T\alpha} G_{\gamma T}(k) \right], \quad (68)$$

where the coefficients are

$$B_{\alpha T\gamma} \equiv \beta \frac{\Omega_\alpha}{(\varepsilon/\nu)^{1/2}} \frac{\chi_{\alpha T}}{\chi_{\alpha\gamma}}, \quad (69)$$

which can be computed prior to integrating the coupled equations. The units of  $\Omega_\alpha$  are  $(\text{seconds}^{-1})(\text{kelvin}^{-1})$ , and  $(\varepsilon/\nu)^{1/2}$  is a rate of strain of the small-scale turbulent motions having units of  $(\text{seconds}^{-1})$ . Hence, the coefficient  $B_{\alpha T\gamma}$  represents a competition between the generation of mixing-ratio fluctuations by temperature fluctuations as parameterized by  $\Omega_\alpha \chi_{\alpha T}$  and the direct production of mixing-ratio fluctuations parameterized by  $(\varepsilon/\nu)^{1/2} \chi_{\alpha\gamma}$ .

However, with (68) added to the rhs of (64), we must have additional equations to determine the  $G_{\alpha T}(k)$ ; this requires one such equation for each species of ion. We turn to the conservation equation for potential temperature  $\theta$ :

$$\frac{\partial \theta}{\partial t} + \underline{V} \cdot \underline{\nabla} \theta = D_T \nabla^2 \theta, \quad (70)$$

where  $D_T$  is the thermal diffusivity; the approximation for the diffusion term on the rhs of (70) is discussed by Hill (1978c).

The potential temperature has an ambient value  $\theta^o$  and a fluctuation  $\theta'$ . As previously noted, at the small scales of interest we do not distinguish between  $\theta'$  and  $T'$ . From (70), we have for the fluctuations,

$$\frac{\partial T'}{\partial t} + \underline{V} \cdot \underline{\nabla} T' = D_T \nabla^2 T' , \quad (71)$$

the spatial Fourier transform of which is

$$\frac{\partial \{T'\}}{\partial t} + \{\underline{V} \cdot \underline{\nabla} T'\} = -k^2 D_T \{T'\} . \quad (72)$$

By multiplying (72) by  $\{T'\}^*$  and adding the complex conjugate of the resultant equation, we obtain an equation for the power spectrum  $\Phi_{TT}(\underline{k})$ . After further implementing the average as in (53a,b) and using the spectral transfer model as in (55), we obtain

$$\frac{\partial \Gamma_{TT}(k)}{\partial t} + \frac{\partial s(k) \Gamma_{TT}(k)}{\partial k} = -2k^2 D_T \Gamma_{TT}(k) . \quad (73)$$

Recall from section 5 that the time derivative in (73) is the time rate of change as observed from the coordinate system moving with the ambient velocity  $\underline{V}^o$ . Introducing the dimensionless spectrum,

$$G_{TT}(x) = \frac{s(k) \Gamma_{TT}(k)}{\chi_{TT}} , \quad (74)$$

and treating the locally stationary case (such that the time-derivative term is neglected), we have from (73),

$$\frac{dG_{TT}(x)}{dx} = -x^2 P_{TT} F(x) G_{TT}(x) , \quad (75)$$

where

$$P_{TT} \equiv \frac{2\beta D_T}{\nu} = \frac{2\beta}{0.72} . \quad (76)$$

The Prandtl number for air,  $\nu/D_T$ , has the value 0.72.

To obtain an equation for  $\Phi_{aT}(k)$ , we obtain the complex conjugate of (72), multiply it by  $\{Q'_a\}$ , multiply (46) by  $\{T'\}^*$ , add these two equations, add to the resultant equation its complex conjugate, and divide by 2. We then have

$$\frac{\partial \Phi_{aT}(k)}{\partial t} - \mathcal{J}_{aT}(k) = -k^2(D_T + D_a) \Phi_{aT}(k) - k^2 \sum_{\beta \neq e} c_{a\beta}(k) \Phi_{\beta T}(k) + \Omega_a \Phi_{TT}(k) . \quad (77)$$

After averaging over the isotropic ensemble as in (53a,b), we have

$$\frac{\partial \Gamma_{aT}(k)}{\partial t} - \mathcal{T}_{aT}(k) = -k^2(D_T + D_a) \Gamma_{aT}(k) - k^2 \sum_{\beta \neq e} c_{a\beta}(k) \Gamma_{\beta T}(k) + \Omega_a \Gamma_{TT}(k) . \quad (78)$$

Recall that  $c_{a\beta}(k)$  is defined in (52). We introduce the spectral transfer model as in (55) and define the dimensionless cospectra as

$$G_{aT}(x) \equiv \frac{s(k) \Gamma_{aT}(k)}{\chi_{aT}} . \quad (79)$$

Then, for the locally stationary case, (78) becomes

$$\frac{dG_{aT}(x)}{dx} = -x^2 P_{aT} F(x) \left[ G_{aT}(x) + \frac{1}{1 + (x\lambda_e/\eta)^2} \sum_{\beta \neq e} c_{aT\beta} G_{\beta T}(x) \right] + B_{aT} F(x) G_{TT}(x) \quad (80)$$

$$P_{aT} \equiv \beta \frac{(D_T + D_a)}{\nu} \quad (81)$$

$$c_{\alpha T \beta} \equiv \frac{D_{\alpha}}{(D_T + D_{\alpha})} \frac{N_{\alpha}}{N_e} S_{\alpha} S_{\beta} \frac{\chi_{\beta T}}{\chi_{\alpha T}} \quad (82)$$

$$B_{\alpha T} \equiv \beta \frac{\Omega_{\alpha}}{(\varepsilon/v)^{1/2}} \frac{\chi_{TT}}{\chi_{\alpha T}} . \quad (83)$$

Consequently, when  $\Omega_{\alpha}$  is not neglected, we must solve  $[n(n+1)/2] + n + 1$  coupled, linear, first-order differential equations where  $n$  is the number of species of ions. That is, with the term (68) added to the rhs of (64), we have  $n(n+1)/2$  equations that are coupled through the  $G_{\alpha T}(x)$  [which appear in (68)] to the  $n$  equations (80), which, in turn, are coupled through the last term in (80) to the one equation (75) for  $G_{TT}(x)$ .

### 6.3 The Nonstationary Case

We now turn to the complication caused by nonstationarity at a fixed spatial location; that is, we consider the time-derivative term in (54), (73), and (78). Limitations of our theory for the nonstationary case are discussed in section 9. We have neglected from the lhs of (64) the term

$$\frac{1}{\eta \chi_{\alpha \gamma}} \frac{\partial \Gamma_{\alpha \gamma}}{\partial t} , \quad (84)$$

and we neglected analogous terms from (75) and (80). Differentiating (58) with respect to time, we have

$$\frac{\partial G_{\alpha \gamma}(x)}{\partial t} = \frac{s(k)}{\chi_{\alpha \gamma}} \frac{\partial \Gamma_{\alpha \gamma}(k)}{\partial t} + G_{\alpha \gamma}(x) \frac{\partial \ln [s(k)]}{\partial t} - G_{\alpha \gamma}(x) \frac{\partial \ln \chi_{\alpha \gamma}}{\partial t} . \quad (85)$$

The time derivative was with respect to spatial position held fixed in the coordinate system moving with the ambient velocity  $\underline{V}^o$  and, hence, is now with respect to  $k$  held fixed. Then,  $x = k\eta$  varies with time because changes in  $\varepsilon$  cause  $\eta$  to vary. Since  $k^* \eta$  is a constant, we have, from differentiating the definition of  $s(k)$ ,

$$\frac{\partial \ln [s(k)]}{\partial t} = \frac{1}{3} \frac{\partial \ln \varepsilon}{\partial t} \left\{ 1 + \frac{1}{2} \left[ 1 + (x/k^* \eta)^{-2a} \right]^{-1} \right\} \equiv \beta^{-1} (\varepsilon/\nu)^{1/2} E h(x) , \quad (86)$$

wherein  $h(x)$  is introduced for notational convenience. For simplicity, we define the following dimensionless quantities,

$$E \equiv \frac{\beta}{(\varepsilon/\nu)^{1/2}} \frac{\partial \ln \varepsilon}{\partial t} \quad (87)$$

and

$$X_{\alpha\gamma} \equiv \frac{\beta}{(\varepsilon/\nu)^{1/2}} \frac{1}{\chi_{\alpha\gamma}} \frac{\partial \chi_{\alpha\gamma}}{\partial t} . \quad (88)$$

The time derivatives in (87) and (88) are with respect to the coordinate system moving with the ambient velocity  $\underline{V}^o$  as discussed at the beginning of Section 5. Dividing (85) by  $\eta s(k)$ , we obtain the term (84),

$$\frac{1}{\eta \chi_{\alpha\gamma}} \frac{\partial \Gamma_{\alpha\gamma}(k)}{\partial t} = \left[ \frac{\beta}{(\varepsilon/\nu)^{1/2}} \frac{\partial G_{\alpha\gamma}(x)}{\partial t} - E h(x) G_{\alpha\gamma}(x) + G_{\alpha\gamma}(x) X_{\alpha\gamma} \right] F(x) . \quad (89)$$

Recall that  $k$  is held fixed for the partial derivatives with respect to time. The time derivative with  $k$  held fixed is related to the time derivative with  $x$  held fixed by

$$\left. \frac{\partial}{\partial t} \right|_k = \left. \frac{\partial}{\partial t} \right|_x - \frac{x}{4} \frac{(\varepsilon/\nu)^{1/2}}{\beta} E \frac{\partial}{\partial x} , \quad (90)$$

where we used, for  $k$  held fixed,  $\partial x / \partial t = x \partial \ln \eta / \partial t$ . Substituting (90) in (89) gives

$$\frac{1}{\eta \chi_{\alpha\gamma}} \frac{\partial \Gamma_{\alpha\gamma}(k)}{\partial t} = \left\{ \frac{\beta}{(\varepsilon/\nu)^{1/2}} \left. \frac{\partial G_{\alpha\gamma}(x)}{\partial t} \right|_x - \frac{E}{4} x \frac{\partial G_{\alpha\gamma}(x)}{\partial x} + [-E h(x) + X_{\alpha\gamma}] G_{\alpha\gamma}(x) \right\} F(x) . \quad (91)$$

Now consider the time-derivative term on the rhs of (91).  $G_{\alpha\gamma}(x)$  does not change with time at fixed  $x$  within any convective range. At least one spectrum or cospectrum must be in a diffusive range for  $G_{\alpha\gamma}(x)$  to change with time at fixed  $x$ . In a diffusive range,  $G_{\alpha\gamma}(x)$  can change because of temporal changes in the dissipation ratios  $\chi_{\gamma\beta}/\chi_{\alpha\gamma}$  that appear in  $c_{\alpha\gamma\beta}$ . Changes in  $\lambda_e/\eta$  cause temporal changes in  $G_{\alpha\gamma}(x)$  only at extremely large  $x$ . If we consider the coupling to temperature fluctuations by the expression (68), then  $G_{\alpha\gamma}(x)$  can change because of changes in the dissipation ratios in (69), (82), and (83) as well as changes in  $E$  and  $X_{\alpha\gamma}$ . We assume that all the rates of change of these quantities are small compared with the turbulence strain rate  $(\varepsilon/\nu)^{1/2}$ . The time-derivative term in (91) is neglected because  $(\varepsilon/\nu)^{1/2}$  appears in the denominator of the remaining time-derivative term in (91). The resulting approximate equation for the temporal slow-varying case is

$$\frac{dG_{\alpha\gamma}}{dx} = \frac{\left\{ \text{rhs} - \left[ -E h(x) + X_{\alpha\gamma} \right] F(x) G_{\alpha\gamma}(x) \right\}}{\left[ 1 - \frac{E}{4} x F(x) \right]}, \quad (92)$$

where “rhs” is the right-hand side of (64), with or without (68) included. We now note that the alteration needed for the nonstationarity case is the same for (75) and (80) as in (92). One need only define the analogous quantities  $X_{TT}$  and  $X_{\alpha T}$ , replace  $G_{\alpha\gamma}(x)$  with  $G_{TT}(x)$  or  $G_{\alpha T}(x)$ , and let rhs be the right-hand side of (75) or (80), respectively.

After this work was completed, Chasnov (1998) published an equation for the nonstationary case that is similar to (92). He considered the case of the viscous-convective and viscous-diffusive ranges of a single passive scalar whose diffusion coefficient is  $D$ . He did not consider the inertial-convective range and the transition to the viscous ranges as we do here. Hence, to obtain Chasnov’s result from (92) we must make the viscous-range approximations:

$$\begin{aligned} F(x) &\approx x^{-1} (k^* \eta)^{-2/3} && \text{for } k \gg k^* \\ s(x) &\approx q^{-1} (\varepsilon/\nu)^{1/2} k && \text{for } k \gg k^* \\ h(x) &\approx \frac{1}{2} && \text{for } k \gg k^* , \end{aligned}$$

where  $q$  is Batchelor's constant, which is denoted as  $\alpha^{-1}$  by Chasnov (1998). Now  $q$  is related to our other parameters by Hill (1978b):

$$q = \beta (k^* \eta)^{-2/3} .$$

Chasnov (1998) used different scaled spectra  $\hat{E}_\theta(\hat{k})$  and wavenumber  $\hat{k}$ , which are related to our notation as follows:

$$G(x) = q^{-1} \hat{k} \hat{E}_\theta \quad \text{for } k \gg k^*$$

$$x = (\nu/D)^{1/2} \hat{k} .$$

We eliminate subscripts on  $G(x)$  and other quantities because we are presently considering a single scalar. Chasnov (1998) defined the parameters  $\chi$  and  $y$  that are related to our (87) and (88) by

$$E = -4 \beta \chi$$

$$X = \beta y .$$

Our (90) is the same as Chasnov's equation (4). He neglected the equivalent of the time-derivative term on the right-hand side of (91), just as we do. To obtain Chasnov's result, we must neglect from (64) the coupling caused by the electric field. Then (66) becomes  $P = 2 \beta D/\nu$ ; thus rhs in (92) becomes, for Chasnov's case,

$$\text{rhs} = -2 \beta x^2 (D/\nu) F(x) G(x) .$$

Substitution of the above into (92) produces Chasnov's (1998) equation (17), which provides a check of (92).

## 7. THE POWER SPECTRUM OF ELECTRON-CONCENTRATION FLUCTUATIONS

The electrons scatter radio waves. Hence, the electron power spectrum is of primary interest. Multiplying (45) by its complex conjugate, we obtain



$$\Phi_{ee}(k) = \frac{\sum_{\alpha \neq e} \sum_{\gamma \neq e} S_{\alpha} S_{\gamma} \Phi_{\alpha\gamma}(k)}{[1 + (k\lambda_e)^2]^2} . \quad (93)$$

Applying the averaging in (53a) to (93) gives

$$\Gamma_{ee}(k) = \frac{\sum_{\alpha \neq e} \sum_{\gamma \neq e} S_{\alpha} S_{\gamma} \Gamma_{\alpha\gamma}(k)}{[1 + (k\lambda_e)^2]^2} . \quad (94)$$

In terms of the dimensionless spectra and cospectra defined in (58), (94) becomes

$$\chi_{ee} G_{ee}(x) = \frac{\sum_{\alpha \neq e} \sum_{\gamma \neq e} S_{\alpha} S_{\gamma} \chi_{\alpha\gamma} G_{\alpha\gamma}(x)}{[1 + (x\lambda_e/\eta)^2]^2} , \quad (95)$$

where  $\chi_{ee}$  is the dissipation rate of the electron-concentration mixing ratio. For  $x \ll 1$ , in which case  $x\lambda_e/\eta \ll 1$  is an excellent approximation, (95) becomes

$$\chi_{ee} = \sum_{\alpha \neq e} \sum_{\gamma \neq e} S_{\alpha} S_{\gamma} \chi_{\alpha\gamma} , \quad (96)$$

which can also be obtained from (94) by substitution of the inertial-convective range formulas.

The cospectrum of potential temperature and electron-concentration mixing ratio can be obtained from (45). By multiplying (45) by  $\{T'\}^*$ , adding the complex conjugate of the resultant equation, and applying the average (53a), we have

$$\Gamma_{eT}(k) = \frac{\sum_{\alpha \neq e} S_{\alpha} \Gamma_{\alpha T}(k)}{1 + (k\lambda_e)^2} . \quad (97)$$

Similar to (96), the cospectral dissipation rate obtained from (97) is

$$\chi_{eT} = \sum_{a \neq e} S_a \chi_{aT} . \quad (98)$$

Also, from (97) we have

$$\chi_{eT} G_{eT}(x) = \frac{\sum_{a \neq e} S_a \chi_{aT} G_{aT}(x)}{1 + (x \lambda_e / \eta)^2} . \quad (99)$$

In the foregoing,  $\Gamma_{ee}(k)$  and  $\Gamma_{eT}(k)$  are spectra and cospectra of the electron mixing-ratio fluctuations,  $Q'_e$ . For application to radio-wave scattering, one needs the power spectrum of  $N'_e$ , i.e., of electron-concentration fluctuations. Of course,  $Q'_e$  has contributions from both  $N'_e$  and  $N'$ , as shown in (101).

According to our definitions,  $N_e = N_e^o + N'_e$  and  $N = N^o + N'$ , such that, to first order,

$$N_e = N Q_e = N^o Q_e^o + N^o Q'_e + Q_e^o N' . \quad (100)$$

Using the ideal gas law and negligible pressure fluctuations, we have  $N' T^o = -N^o T'$ . Consequently, at zero order (100) gives  $N_e^o = N^o Q_e^o$ , and at first order (100) gives

$$N'_e = N^o Q'_e - \frac{N_e^o}{T^o} T' . \quad (101)$$

After Fourier transformation of (101), multiplication by its complex conjugate, and implementing the average as in (53a), the power spectrum of electron-concentration fluctuations,  $\Gamma(k)$ , is

$$\Gamma(k) = N^{o^2} \Gamma_{ee}(k) - 2 \frac{N^o N_e^o}{T^o} \Gamma_{eT}(k) + \left( \frac{N_e^o}{T^o} \right)^2 \Gamma_{TT}(k) . \quad (102)$$

The units of  $\Gamma(k)$  are length times the square of electrons per unit volume. The connection between  $\Gamma(k)$  and the Bragg-scattering cross section is given in section 12.

## 8. BOUNDARY CONDITIONS

The boundary condition (63) represents a balance between the production rate of fluctuations at large scales which determines the level of the inertial-convective range and the diffusive dissipation rate of fluctuations. For the cases of coupling to temperature fluctuations (section 6.2), nonstationarity (section 6.3), or both cases together (section 6.3), the balance between the production rate and the diffusive dissipation rate is upset. In such cases, to maintain the meaning of  $\chi_{TT}$ ,  $\chi_{aT}$ , and  $\chi_{ay}$  as diffusive dissipation, the boundary condition at small  $x$  must be derived. The derivation is necessarily approximate in that it requires separation in the wavenumber space between the production and the dissipation.

### 8.1 Boundary Conditions for the Stationary Case With Coupling to Temperature Fluctuations

The coupling to temperature fluctuations requires a boundary condition that differs from (63). Equation (75) for  $G_{TT}(x)$  is not coupled to other equations. Thus, the boundary condition for numerical integration of (75) remains (63), namely,  $G_{TT}(x_i) = 1.0$ , where  $x_i$  is the initial value of  $x$  for integration of the equations toward large  $x$ .

In the inertial-convective range (i.e.,  $x \ll k^* \eta$  and, hence,  $x \ll 1$ ), the diffusion terms in (80) can be neglected,  $F(x) \approx x^{-5/3}$ , and  $G_{TT}(x) \approx 1.0$ ; therefore, (80) is approximated by

$$\frac{dG_{aT}(x)}{dx} = B_{aT} x^{-5/3} . \quad (103)$$

The integral of this approximate equation from  $x_i$  to some  $x_h$  at the high-wavenumber terminus of the inertial-convective range is

$$G_{aT}(x_h) - G_{aT}(x_i) = -\frac{3}{2} B_{aT} (x_h^{-2/3} - x_i^{-2/3}) . \quad (104)$$

For  $x_h \gg x_i$ , we have

$$G_{\alpha T}(x_i) = G_{\alpha T}(x_h) - \frac{3}{2} B_{\alpha T} x_i^{-2/3} , \quad (105)$$

from which we see that the effect of the coupling decays as  $x_h$  increases. Thus, for  $x_h$  that are large enough, we can take  $G_{\alpha T}(x_h) \approx 1$ , in which case (105) becomes

$$G_{\alpha T}(x_i) = 1 - \frac{3}{2} B_{\alpha T} x_i^{-2/3} . \quad (106)$$

This is our approximation for the initial condition. Note that if the coupling is removed by requiring  $B_{\alpha T} = 0$ , then this initial condition (106) reverts to (63), as it should.

Now we must obtain the initial condition for  $G_{\alpha\gamma}(x)$ . With the term (68) added to (64), we neglect the diffusion term for  $x \ll k^* \eta$  and approximate  $F(x) \approx x^{-5/3}$  to obtain

$$\frac{dG_{\alpha\gamma}(x)}{dx} = x^{-5/3} [B_{\alpha T\gamma} G_{\alpha T}(x) + B_{\gamma T\alpha} G_{\gamma T}(x)] . \quad (107)$$

Solution of (103) for  $x$  in the inertial-convective range is essentially (104) with  $x_h$  replaced by  $x$  such that

$$G_{\alpha T}(x) = G_{\alpha T}(x_i) - \frac{3}{2} B_{\alpha T} (x^{-2/3} - x_i^{-2/3}) \quad (108a)$$

$$= 1 - \frac{3}{2} B_{\alpha T} x^{-2/3} , \quad (108b)$$

where (108b) follows from (108a) by substituting (106). We now follow the same reasoning that led to (106). We substitute (108b) into (107), integrate from  $x_i$  to  $x_h$ , neglect terms on the basis that  $x_h \gg x_i$ , and approximate  $G_{\alpha\gamma}(x_h) \approx 1$ ; we thereby obtain

$$G_{\alpha\gamma}(x_i) = 1 - \frac{3}{2} (B_{\alpha T\gamma} + B_{\gamma T\alpha}) x_i^{-2/3} + \frac{9}{8} (B_{\alpha T\gamma} B_{\alpha T} + B_{\gamma T\alpha} B_{\gamma T}) x_i^{-4/3} . \quad (109)$$

This is our approximation to the initial condition for  $G_{\alpha\gamma}(x)$ . If the coupling is removed, i.e.,  $B_{\alpha T\gamma} = 0$  for all  $\alpha$  and  $\gamma$ , then (109) becomes (63), as it should.

## 8.2 Boundary Conditions for the Nonstationary Case With No Coupling to Temperature Fluctuations

The nonstationary case poses a problem in the choice of a boundary condition at small  $x$  for the subsequent solution of the equations toward large  $x$ . The boundary condition (63) for the stationary case follows from (64) because at sufficiently small  $x$  the rhs of (64) is negligible such that (64) is approximately  $dG_{\alpha\gamma}(x)/dx = 0$ . Now we must use (92) to find a consistent formula for the boundary condition for the nonstationary case.

First, let  $x$  be within the inertial-convective range such that  $x \ll 1$  and  $x \ll k^* \eta$ . Then the effects of diffusion, denoted by rhs in (92), are negligible, and  $h(x)$  and  $F(x)$  can be approximated by their formulas for  $x \ll k^* \eta$ . Equation (92) then becomes

$$\frac{dG_{\alpha\gamma}(x)}{dx} = \frac{2 d_{\alpha\gamma}}{3 x_s} \frac{(x/x_s)^{-5/3}}{1 \pm (x/x_s)^{-2/3}} G_{\alpha\gamma}(x) , \quad (110)$$

where we have defined

$$d_{\alpha\gamma} \equiv -\frac{3}{2} \left( -\frac{E}{3} + X_{\alpha\gamma} \right) x_s^{-2/3} \quad (111)$$

and

$$x_s \equiv \left( \frac{|E|}{4} \right)^{3/2} . \quad (112)$$

The upper and lower signs in the denominator of (110) correspond to cases  $E \leq 0$  and  $E > 0$ , respectively. For the case  $E > 0$ , the denominator in (110) has a zero on the positive  $x$  axis at  $x = x_s$ ; hence, the differential equations (92) and (110) have a singularity on the positive  $x$  axis. Thus, if  $E > 0$ , integration of (92) toward large positive  $x$  must begin at a value of  $x$  that is substantially greater than  $x_s$ . In addition, the boundary condition must apply for  $x$  in the inertial-

convective range, which limits how large  $x_s$  can be if  $E > 0$  and, hence, how large  $E$  can be and yet obtain a solution of (92).

If we define  $\mathcal{Y} \equiv \ln [G_{\alpha\gamma}(x)]$  and  $z \equiv \ln [(x/x_s)^{2/3}]$ , then (110) becomes

$$\frac{d\mathcal{Y}}{dz} = \frac{d_{\alpha\gamma}}{e^z \pm 1} . \quad (113)$$

This can be integrated from our initial boundary position  $z_i$  (corresponding to  $x = x_i$ ) to infinity. The result is

$$\mathcal{Y}(z_i) - \mathcal{Y}(\infty) = \mp d_{\alpha\gamma} \ln (\pm e^{-z_i} + 1) , \quad (114)$$

where our convention is that upper and lower signs correspond to cases  $E \leq 0$  and  $E > 0$ , respectively. For an infinitely extensive convective range, we have  $G_{\alpha\gamma}(x) \rightarrow 1$  as  $x \rightarrow \infty$ , from which it follows that  $\mathcal{Y}(\infty) = 0$ . Therefore, we have from (114) that the boundary condition at  $x = x_i$  is

$$G_{\alpha\gamma}(x_i) = \left[ 1 \pm (x_i/x_s)^{-2/3} \right]^{\mp d_{\alpha\gamma}} . \quad (115)$$

For the case  $E \leq 0$ , Taylor series expansion of the logarithm in (114) for very large  $z_i$  leads to the boundary condition for  $E = 0$ , namely,

$$G_{\alpha\gamma}(x_i) = \exp \left( \frac{3}{2} X_{\alpha\gamma} x_i^{-2/3} \right) \quad \text{for } E = 0 . \quad (116)$$

If, in addition to  $E = 0$ , we have  $X_{\alpha\gamma} = 0$ , then (116) becomes the initial condition (63) corresponding to the stationary case.

As we will see in the next section,  $G_{TT}(x)$  and  $G_{\alpha T}(x)$  also have (115) as their initial condition with  $d_{\alpha\gamma}$  replaced by  $d_{TT}$  and  $d_{\alpha T}$ , respectively. However, there is no need to calculate  $G_{TT}(x)$  and  $G_{\alpha T}(x)$  for the purpose of calculating  $G_{\alpha\gamma}(x)$  because the case in question has no coupling to temperature fluctuations.

### 8.3 Boundary Conditions for the Nonstationary Case With Coupling to Temperature Fluctuations

As noted below (92), for the nonstationary case, (75) is replaced by

$$\frac{dG_{TT}(x)}{dx} = \frac{-x^2 P_{TT} F(x) G_{TT}(x) - [-E h(x) + X_{TT}] F(x) G_{TT}(x)}{\left[ 1 - \frac{E}{4} x F(x) \right]}. \quad (117)$$

By the same method that gave (110), we obtain (110) with  $G_{\alpha T}(x)$  replaced by  $G_{TT}(x)$ . It follows from the reasoning leading to (115) that the boundary condition for  $G_{TT}(x)$  is

$$G_{TT}(x_i) = \left[ 1 \pm (x_i/x_s)^{-2/3} \right]^{\mp d_{TT}}, \quad (118)$$

where  $d_{TT}$  is defined as in (111) with  $X_{\alpha T}$  replaced by  $X_{TT}$ . As with (115), (118) reduces to (63) for  $E = 0$  and  $X_{TT}(x) = 0$ .

Now  $G_{\alpha T}(x)$  also satisfies (92) with  $X_{\alpha T}$  replaced by  $X_{\alpha T}$ , but rhs in (92) now includes the last term in (80). Thus, the equation analogous to (110) is

$$\frac{dG_{\alpha T}(x)}{dx} = \frac{B_{\alpha T} x^{-5/3} [1 \pm (x/x_s)^{-2/3}]^{\mp d_{TT}} + \frac{2}{3} \frac{d_{\alpha T}}{x_s} (x/x_s)^{-5/3} G_{\alpha T}(x)}{1 \pm (x/x_s)^{-2/3}}, \quad (119)$$

wherein  $G_{TT}(x)$  is approximated by (118) with  $x_i$  replaced by  $x$ , and  $d_{\alpha T}$  is defined as in (111) with  $X_{\alpha T}$  replaced by  $X_{\alpha T}$ . Define the following as

$$u \equiv \ln [1 \pm (x/x_s)^{-2/3}] = \ln [1 \pm (x_s/x)^{2/3}] \quad (120a)$$

$$a \equiv \mp d_{TT} \quad (120b)$$

$$b \equiv b_a \equiv \mp d_{aT} \quad (120c)$$

$$c \equiv c_a \equiv \mp \frac{3}{2} B_{aT} x_s^{-2/3} . \quad (120d)$$

The right-most formula in (120a) can be computed even when  $E = 0$ . Then (119) becomes

$$\frac{dG_{aT}}{du} = c e^{au} + b G_{aT} . \quad (121)$$

Solution of an equation like (121) is the sum of a solution of the homogeneous equation (i.e., with  $c = 0$ ) and a particular solution of the inhomogeneous equation. The solution of the homogeneous equation that satisfies (63) in the stationary limit has already been given in (115). It is

$$e^{bu} = [1 \pm (x/x_s)^{-2/3}]^{\mp d_{aT}} . \quad (122)$$

A particular solution of (121) can be found by substituting  $G_{aT} \propto e^{au}$  into (121); the resulting particular solution is

$$\frac{c}{a-b} e^{au} = -B_{aT} (X_{TT} - X_{aT})^{-1} [1 \pm (x/x_s)^{-2/3}]^{\mp d_{TT}} . \quad (123)$$

As required, for vanishing coupling to temperature fluctuations, i.e., for  $B_{aT} = 0$ , the particular solution (123) vanishes. Note that (123) is not a valid solution if  $X_{TT} - X_{aT} = 0$ . Using  $a = b$  in (121), we find that the particular solution for the case  $X_{TT} - X_{aT} = 0$  is

$$\begin{aligned} c u e^{au} &= \mp \frac{3}{2} B_{aT} x_s^{-2/3} \ln [1 \pm (x/x_s)^{-2/3}] [1 \pm (x/x_s)^{-2/3}]^{\mp d_{TT}} \\ &= -\frac{3}{2} B_{aT} x^{-2/3} \exp \left( \frac{3}{2} X_{TT} x^{-2/3} \right) \quad \text{for } E = 0 . \end{aligned} \quad (124)$$



The solution for  $a \neq b$  is the sum of (123) and some coefficient times (122); consider the coefficient  $1 - [c/(a-b)]$  such that

$$G_{aT}(x) = e^{bu} + \frac{c}{a-b} e^{bu} [e^{(a-b)u} - 1] . \quad (125)$$

As  $(a-b) \rightarrow 0$ , this solution becomes

$$G_{aT}(x) = e^{bu} + c u e^{au} , \quad (126)$$

which is (122) plus the particular solution (124). If  $B_{aT} = 0$ , then  $c = 0$  such that (125) becomes (122), which has the same correct properties as (115) and (116). If  $E \rightarrow 0$ , then, using (116), (125) becomes

$$G_{aT}(x) = \exp \left( \frac{3}{2} X_{aT} x^{-2/3} \right) \left[ 1 - \frac{B_{aT}}{X_{TT} - X_{aT}} \left\{ -1 + \exp \left[ \frac{3}{2} x^{-2/3} (X_{TT} - X_{aT}) \right] \right\} \right] . \quad (127)$$

As  $X_{TT}$  and  $X_{aT}$  approach zero, (127) becomes

$$G_{aT}(x) = 1 - \frac{3}{2} B_{aT} x^{-2/3} , \quad (128)$$

which is the correct stationary limit in (106).

Therefore, (125) is the correct solution for both  $a \neq b$  and the limit  $a = b$ . However, for substitution of values, the limiting formula for  $a = b$  must be stated separately. From (125) and (126) the boundary conditions are

$$G_{aT}(x_i) = [1 \pm (x_i/x_s)^{-2/3}]^{\mp d_{aT}} \left[ 1 - \frac{B_{aT}}{X_{TT} - X_{aT}} \left\{ -1 + [1 \pm (x_i/x_s)^{-2/3}]^{\mp (d_{TT} - d_{aT})} \right\} \right] \quad \text{for } X_{TT} \neq X_{aT} \quad (129)$$

and

$$G_{aT}(x_i) = [1 \pm (x_i/x_s)^{-2/3}]^{\mp d_{aT}} \left\{ 1 \mp \frac{3}{2} B_{aT} x_s^{-2/3} \ln [1 \pm (x_i/x_s)^{-2/3}] \right\} \quad \text{for } X_{TT} = X_{aT} \quad (130)$$

If  $E = 0$  then (129) and (130) become

$$G_{\alpha T}(x_i) = \exp\left(\frac{3}{2} x_i^{-2/3} X_{\alpha T}\right) \left[ 1 - \frac{B_{\alpha T}}{X_{TT} - X_{\alpha T}} \left\{ -1 + \exp\left[\frac{3}{2} x_i^{-2/3} (X_{TT} - X_{\alpha T})\right] \right\} \right] \quad \text{for } X_{TT} \neq X_{\alpha T} \text{ and } E = 0$$

and

$$G_{\alpha T}(x_i) = \exp\left(\frac{3}{2} x_i^{-2/3} X_{\alpha T}\right) \left[ 1 - \frac{3}{2} B_{\alpha T} x^{-2/3} \right] \quad \text{for } X_{TT} = X_{\alpha T} \text{ and } E = 0 .$$

Next we turn to the boundary condition for  $G_{\alpha\gamma}(x)$ . For the case in hand, rhs in (92) includes the term (68). For an inertial-convective range, we substitute (125) into (68) to obtain the following approximation for the additional term in (68):

$$\text{TERM} \approx x^{-5/3} \frac{\left\{ I_{\alpha} e^{b_{\alpha} u} + I_{\gamma} e^{b_{\gamma} u} + J e^{au} \right\}}{\mp \frac{3}{2} x_s^{-2/3}}, \quad (131)$$

where

$$I_{\alpha} \equiv \left[ B_{\alpha T \gamma} \left( 1 - \frac{c_{\alpha}}{a - b_{\alpha}} \right) \right] \left( \mp \frac{3}{2} x_s^{-2/3} \right), \quad (132a)$$

$$J \equiv \left[ B_{\alpha T \gamma} \frac{c_{\alpha}}{a - b_{\alpha}} + B_{\gamma T \alpha} \frac{c_{\gamma}}{a - b_{\gamma}} \right] \left( \mp \frac{3}{2} x_s^{-2/3} \right), \quad (132b)$$

and  $I_{\gamma}$  is obtained from  $I_{\alpha}$  by interchanging  $\alpha$  and  $\gamma$ . In (131) and (132a,b) we have included subscripts in the definitions (120c,d) to distinguish between the two species denoted by  $\alpha$  and  $\gamma$ . For small enough  $x$  in the inertial-convective range, the rhs in (92) approximately equals TERM in (131). Hence, (92) gives

$$\frac{d G_{\alpha\gamma}(x)}{dx} = \frac{\text{TERM} + \frac{2}{3} \frac{d_{\alpha\gamma}}{x_s} (x/x_s)^{-5/3} G_{\alpha\gamma}(x)}{1 \pm (x/x_s)^{-2/3}} . \quad (133)$$

Using the substitution (120a) and using (131) for TERM, (133) becomes

$$\frac{dG_{\alpha\gamma}}{du} = I_{\alpha} e^{b_{\alpha}u} + I_{\gamma} e^{b_{\gamma}u} + J e^{au} + dG_{\alpha\gamma} , \quad (134)$$

where

$$d \equiv \mp d_{\alpha\gamma} . \quad (135)$$

The solution to the homogeneous equation is

$$e^{du} = [1 \pm (x/x_s)^{-2/3}]^{\mp d_{\alpha\gamma}} . \quad (136)$$

The particular solution is the sum of three terms of the same form as the lhs of (123). For instance, the first term of the particular solution, corresponding to the first term on the rhs of (134), is

$$\frac{I_{\alpha}}{b_{\alpha} - d} e^{b_{\alpha}u} . \quad (137)$$

Constructing the solution with the correct limiting properties follows from the analysis of (125). The solution is

$$\begin{aligned} G_{\alpha\gamma}(x) = e^{du} + e^{du} \left\{ \frac{I_{\alpha}}{b_{\alpha} - d} [-1 + e^{(b_{\alpha} - d)u}] \right. \\ + \frac{I_{\gamma}}{b_{\gamma} - d} [-1 + e^{(b_{\gamma} - d)u}] \\ \left. + \frac{J}{a - d} [-1 + e^{(a - d)u}] \right\} . \end{aligned} \quad (138)$$

Of course, if any of the three denominators vanish in (138), then the term can be replaced by its asymptotic formula. The three asymptotic formulas are  $I_{\alpha}u$ ,  $I_{\gamma}u$ , and  $Ju$ . For the purpose

of computation, we must find explicit limiting formulas for cases when zeros appear in the denominators in (138). For this purpose,  $J$  in (132b) is separated into its two terms such that the last term in (138) is added to the first and second terms in (138) to give

$$G_{\alpha\gamma}(x) = [1 \pm (x/x_s)^{-2/3}]^{\mp d_{\alpha\gamma}} \left\{ 1 + B_{\alpha T\gamma} K_{\alpha\gamma}(u) + B_{\gamma T\alpha} K_{\gamma\alpha}(u) \right\}, \quad (139)$$

where

$$K_{\alpha\gamma}(u) = g_{\alpha T}(w) + \frac{B_{\alpha T}}{X_{TT} - X_{\alpha T}} [g_{\alpha T}(w) - g_{TT}(w)] \quad \text{for } X_{TT} \neq X_{\alpha T}, \quad (140)$$

$$\begin{aligned} w &\equiv \mp \frac{3}{2} x_s^{-2/3} u \\ &= -\frac{3}{2} x^{-2/3} \quad \text{if } E = 0, \end{aligned}$$

$$g_{TT}(w) = \begin{cases} \frac{1 - \exp[-(X_{TT} - X_{\alpha\gamma})w]}{X_{TT} - X_{\alpha\gamma}} & \text{if } X_{TT} \neq X_{\alpha\gamma} \\ w & \text{if } X_{TT} = X_{\alpha\gamma}, \end{cases} \quad (141)$$

and  $g_{\alpha T}(w)$  is obtained from (141) by replacing  $X_{TT}$  with  $X_{\alpha T}$ . In (141) the case  $X_{TT} = X_{\alpha\gamma}$  is obtained from the case  $X_{TT} \neq X_{\alpha\gamma}$  by the Taylor series expansion in  $(X_{TT} - X_{\alpha\gamma})w$ .

For the case  $X_{TT} = X_{\alpha T}$ , we must express (140) differently. The exponential in (141) is expressed as

$$\exp[-(X_{TT} - X_{\alpha\gamma})w] = \exp[-(X_{TT} - X_{\alpha T})w] \exp[-(X_{\alpha T} - X_{\alpha\gamma})w]; \quad (142)$$

the exponential containing  $(X_{TT} - X_{aT})$  in (142) is expanded in small values of its argument; and  $g_{TT}(w) - g_{aT}(w)$  in (140) is expressed with a common denominator. We thereby obtain as  $X_{TT} \rightarrow X_{aT}$  that

$$\frac{g_{aT}(w) - g_{TT}(w)}{X_{TT} - X_{aT}} = \frac{1 - e^{Aw} + Aw e^{Aw}}{A^2}, \quad (143)$$

where

$$A = -(X_{TT} - X_{aT}) = -(X_{aT} - X_{aT}) . \quad (144)$$

If  $A \rightarrow 0$ , then (143) approaches  $w^2/2$ . Therefore, to complement (140), we have

$$K_{aT}(u) = g_{aT}(w) + B_{aT} L(w) \quad \text{for } X_{TT} = X_{aT}, \quad (145)$$

where

$$L(w) = \begin{cases} \frac{1 - e^{Aw} + Aw e^{Aw}}{A^2} & \text{for } A \neq 0 \\ \frac{w^2}{2} & \text{for } A = 0 . \end{cases} \quad (146)$$

Finally, our boundary condition for  $G_{aT}(x)$  is (139) evaluated at  $x = x_i$ . For evaluation of (139), we have the two cases (140) and (145). Note that for the stationary case [i.e.,  $E = X_{TT} = X_{aT} = X_{aT} = 0$ ], substitution of (140), (141), (145), and (146) in (139) gives the correct stationary limit (109).

## 9. LIMITATIONS OF THE NONSTATIONARY CASE

The theory of the viscous-convective range originated by Batchelor (1959) is for the stationary case. All subsequent theories and models, including those by Hill (1978b) that we use here, are for the stationary case as well. The stationary case is a case for which mechanical turbulence has always been active at a steady level of energy input, and scalar variance has always been maintained by a steady level of input. The relevance of such an unrealistic case to real turbulent flow is obtained from the concept of local stationarity. Local stationarity means that statistics of the inertial and/or viscous ranges are nearly the same in nonstationary cases as in stationary cases because the small scales approach statistical equilibrium much more rapidly than the statistics' rate of change at large scales. For the velocity field, the case of very large Reynolds numbers and very small spatial scales is also the locally stationary case.

On the other hand, the viscous-convective range has the special property that it contains infinite scalar variance for the stationary case with an infinite Schmidt number. This is because the integral over all wavenumbers of a viscous-convective range's  $k^{-1}$  power law diverges logarithmically at its upper limit. It is the viscous-diffusive range that limits the scalar variance to finite values. Thus, if scalar variance is initially injected at large scales, then some time must pass before the viscous-convective range has its steady-state form. For a finite Schmidt number, the scalar variance input at large scales places an upper bound on the level of the viscous-convective range after local stationarity is established.

The derivation of boundary conditions in section 8 employs the assumption that local stationarity is valid and that there are some spatial wavenumbers in the inertial-convective range where the  $k^{-5/3}$  power law is evident. This clearly places a limit on how large the quantities  $E$ ,  $X_{\alpha\gamma}$ ,  $X_{\alpha T}$ , and  $X_{TT}$  can be. These quantities, defined in (87), (88), and the last sentence of section 6, parameterize the temporal rate of change of the dissipation rates. A check of the calculated spectra is needed to assure that some inertial-convective range power law is observed. This is of increasing concern as one decreases the volume in which the dissipation rates are calculated. Because of the spatial intermittency of turbulence, the advection of dissipation into or out of the volume during a temporal increment can cause increasingly large values of  $E$ ,  $X_{\alpha\gamma}$ ,  $X_{\alpha T}$ , and  $X_{TT}$  as the averaging volume decreases.

## 10. DEFINITION OF DISSIPATION RATES

Let an overbar denote an average over a specific volume whose minimum dimension is at least the size of an inertial-range spacing. The average is calculated at a specific time, so there is

no average over time. Then,  $\bar{\underline{V}}$  and  $\bar{T}$  are the volume averages of velocity and potential temperature. The fluctuations from these instantaneous, local averages are denoted by  $\underline{V}'$  and  $T'$ . The equation for the temporal rate of change of  $\bar{T'^2}$ , as derived from (70), is

$$\frac{\partial \bar{T'^2}}{\partial t} + \bar{\underline{V}} \cdot \underline{\nabla}(\bar{T'^2}) + \underline{\nabla} \cdot (\bar{\underline{V}'T'^2}) + 2 \bar{\underline{V}'T'} \cdot \underline{\nabla} \bar{T} - D_T \bar{\nabla^2(T'^2)} = -2 D_T \overline{(\underline{\nabla} T') \cdot (\underline{\nabla} T')} . \quad (147)$$

The term on the rhs is necessarily negative and therefore always represents a loss, never a gain, and is therefore called the dissipation rate of  $\bar{T'^2}$ . The fourth term on the lhs is the production rate of  $\bar{T'^2}$  from the gradient of the average potential temperature. The second term on the lhs is the rate of change of  $\bar{T'^2}$  caused by the locally averaged velocity  $\bar{\underline{V}}$  carrying  $\bar{T'^2}$  into or out of the volume. Using incompressibility, i.e.,  $\underline{\nabla} \cdot \bar{\underline{V}} = 0$ , the second term can be rewritten as

$$\underline{\nabla} \cdot \bar{\underline{V}} \bar{T'^2} = \mathcal{V}^{-1} \int d\underline{S} \cdot \bar{\underline{V}} T'^2 . \quad (148)$$

We have used the fact that the volume integral of a divergence is the surface integral of the component of the vector normal to the surface that bounds the volume. In (148),  $|d\underline{S}|$  is the differential of surface area, the direction of  $d\underline{S}$  is normal to the surface, and  $\mathcal{V}$  is the volume over which the volume average is performed. In (148) we see that the term in question is proportional to the average over the surface of the surface-normal component of  $\bar{\underline{V}} T'^2$ .

Likewise, the third and fifth terms in (147) can be written as

$$\underline{\nabla} \cdot (\bar{\underline{V}'T'^2}) = \mathcal{V}^{-1} \int d\underline{S} \cdot \underline{V}' T'^2 \quad (149)$$

$$- D_T \bar{\nabla^2(T'^2)} = - D_T \mathcal{V}^{-1} \int d\underline{S} \cdot \underline{\nabla} (T'^2) . \quad (150)$$

Just as  $\bar{\underline{V}} T'^2$ , which appears within (148), is the flux of  $T'^2$  caused by the volume-average velocity  $\bar{\underline{V}}$ ,  $\underline{V}' T'^2$ , which appears within (149), is the flux of  $T'^2$  caused by the turbulence fluctuation of velocity  $\underline{V}'$ . Also,  $- D_T \underline{\nabla} T'^2$ , which appears within (150), is the diffusive flux of  $T'^2$  into or out of the volume.

If the turbulence is confined within a box and if the volume average is over the entire box, then the surfaces of integration for (148)–(150) can be beyond the box where  $\underline{V}'$  and  $T'$  vanish such that the right hand sides of (148)–(150) are zero. Then (147) reduces to

$$\frac{\partial \overline{T'^2}}{\partial t} + 2 \overline{\underline{V}' T'} \cdot \underline{\nabla} \overline{T} = -2 D_T \overline{(\underline{\nabla} T') \cdot (\underline{\nabla} T')} . \quad (151)$$

For this simple case, the time rate of change of  $\overline{T'^2}$  is caused by the gradient production and the dissipation. For homogeneous turbulence, the surface-integrated fluxes (148)–(150) become negligible as the volume becomes very large, and (151) becomes a good approximation.

For isotropic turbulence, Taylor series expansion of the structure function gives

$$\lim_{r \rightarrow 0} \langle [T'(\underline{x}) - T'(\underline{x} + \underline{r})]^2 \rangle = \frac{1}{3} \overline{(\underline{\nabla} T') \cdot (\underline{\nabla} T')} r^2 . \quad (152)$$

Thus, the dissipation rate,

$$\chi_{TT} \equiv 2 D_T \overline{(\underline{\nabla} T') \cdot (\underline{\nabla} T')} , \quad (153)$$

determines the structure function at small enough  $r$ . That is, as given by Obukhov (1949),

$$\lim_{r \rightarrow 0} \langle [T'(\underline{x}) - T'(\underline{x} + \underline{r})]^2 \rangle = \frac{\chi_{TT}}{6 D_T} r^2 . \quad (154)$$

Since the spectrum  $\Gamma_{TT}(k)$  is a high-pass transform of the structure function, it follows that  $\Gamma_{TT}(k)$  is proportional to  $\chi_{TT}$  for  $k$  in the dissipation range of  $\Gamma_{TT}(k)$ . Integration toward lower  $k$  of the spectral transfer model (73) produces  $\Gamma_{TT}(k)$  proportional to  $\chi_{TT}$  at all  $k$  where local stationarity is accurate. This agrees with the classic result, based on dimensional analysis, that  $\Gamma_{TT}(k)$  is proportional to  $\chi_{TT}$  in the inertial-convective range [see (62)]. Determining the dissipation rate from (153) is called the direct dissipation method.

We conclude that the dissipation rate defined in (153) is the same as is required in the denominator of (74). At small length scales such that local stationarity is accurate, for any scalar satisfying the continuity equation (70), and for locally isotropic turbulence, the structure function and spectrum are proportional to the dissipation rate defined in (153).

A similar analysis can be performed for the temporal rate of change of turbulent kinetic energy. In the analysis, one identifies advective and viscous transport of energy across the volume's surface. The analysis leads to an expression for the average rate of dissipation of turbulent kinetic energy per unit mass of fluid as given by



$$\varepsilon = \nu \left( \overline{\frac{\partial V_i}{\partial x_j} \frac{\partial V_i}{\partial x_j}} + \overline{\frac{\partial V_i}{\partial x_j} \frac{\partial V_j}{\partial x_i}} \right), \quad (155)$$

where  $\nu$  is the kinematic viscosity and repeated indices are summed. This expression for  $\varepsilon$  is equal to the volume average of the local and instantaneous rate of viscous dissipation of mechanical energy, per unit mass of fluid, as given by Batchelor (1970, p. 153). Batchelor's expression is  $\varepsilon = 2\nu e_{ij} e_{ij}$ , where the stress tensor is

$$e_{ij} = \frac{1}{2} \left( \frac{\partial V_i}{\partial x_j} + \frac{\partial V_j}{\partial x_i} \right). \quad (156)$$

The dissipation rates are actually determined by large-scale production and the rate of change of variance, as shown by the gradient-production term and time-derivative terms on the lhs of (151). For energy dissipation,  $\varepsilon$ , Sreenivasan (1998) has determined the minimum Reynolds number for which  $\varepsilon$  scales with the velocity variance and the integral scale; this is the same as determining the Reynolds number for which there is negligible advective and viscous transport across the averaging volume's surface. Analogously, for scalar dissipation, the advection effects, as given in (148)–(150), modify the relationship between production and dissipation if the averaging volume is small. Even with the advection effects, the dissipation rate in (153) determines the level of the spectrum at high wavenumbers in the manner described above with respect to (154). This is the property of  $\chi_{TT}$  that is exploited in the scaling in (74). The same scaling is used in (58) and (79); hence,  $\chi_{\alpha\gamma}$  and  $\chi_{\alpha T}$  must also determine the level of their respective spectra at high wavenumbers.

The dissipation rates  $\chi_{\alpha\gamma}$  and  $\chi_{\alpha T}$  are needed in (65), (69), (82), and (83) for the purpose of calculating  $G_{\alpha\gamma}(x)$  and  $G_{\alpha T}(x)$ . These dissipation rates are also needed in (58) and (79) for the purpose of calculating  $\Gamma_{\alpha\gamma}(k)$  and  $\Gamma_{\alpha T}(k)$  so that the electron-concentration power spectrum can be obtained from (94), (97), and (102). Recall that in the introduction we described advection of initial ionization profiles by simulation of the dynamics of breaking internal waves and Kelvin-Helmholtz instabilities. The question at hand is, “How do we determine the  $\chi_{\alpha\gamma}$  and  $\chi_{\alpha T}$  from these simulations such that we can implement the subgrid-scale calculation using the turbulence advection model?” A related question is, “How many of the phenomena described by (11), (12), and (13) must be retained in the simulation?”

The grid scale of the simulations is larger than the scale at which even the fastest diffusion mode affects the ionization. The ambipolar electric field is generated by the diffusion

of the ionization, and no large-scale phenomena that generate electric fields (e.g., the geomagnetic field) are included in the simulation. Hence, we can require that the ionization obey charge neutrality such that (13) gives

$$\underline{E} = 0 \quad (157)$$

and

$$N_e = \sum_{\beta \neq e} S_\beta N_\beta . \quad (158)$$

Then the divergence of (11) substituted into (12) gives the equations for the ions as follows:

$$\frac{\partial Q_\alpha}{\partial t} + \underline{V} \cdot \underline{\nabla} Q_\alpha = \frac{1}{N} \underline{\nabla} \cdot \mathcal{D}_\alpha \underline{\nabla} Q_\alpha . \quad (159)$$

The simulation must smooth the advected ionization at scales approaching the grid scale in order to avoid numerical artifacts. Therefore, we cannot use the geophysical values of  $\mathcal{D}_\alpha$  in (159). Instead, we must use values that are nearly the same as the effective kinematic viscosity used to smooth the velocity fields in the simulation. This effective viscosity is greater than the geophysical viscosity. Thus, we need not, and from the point of view of efficient calculation we should not, include any spatial dependence in the diffusion coefficient. Consequently,  $\mathcal{D}_\alpha$  in (159) must be replaced with a constant that commutes with the divergence operator in (159). Furthermore, we will show that charge neutrality (158) requires that all the ions have the same diffusion coefficient. Therefore, (159) must be replaced by

$$\frac{\partial Q_\alpha}{\partial t} + \underline{V} \cdot \underline{\nabla} Q_\alpha = D_S \nabla^2 Q_\alpha , \quad (160)$$

where  $D_S$  is the diffusion coefficient used in the simulation. Reasonable values of the effective diffusion coefficient  $D_S$  to use in the simulation are between about 0.5 and 1.0 times the effective kinematic viscosity. Next, we verify that (160) maintains charge neutrality if charge neutrality exists initially. Multiply (160) by  $q_\alpha$  and sum over all  $\alpha \neq e$ ; divide (158) by  $N$  and apply the

co-moving derivative  $D/Dt$  to it. Comparison of the two resultant equations shows that  $Q_e$  also satisfies (157) as a consequence of charge neutrality. Next, multiply (157) by  $q_\alpha$  and sum over all  $\alpha$  (including  $\alpha = e$ ) to obtain

$$\frac{\partial Q}{\partial t} + \underline{V} \cdot \underline{\nabla} Q = D_S \nabla^2 Q , \quad (161)$$

where  $Q \equiv \sum_\alpha q_\alpha Q_\alpha$  is the mixing ratio of charge density. Now (161) shows that the charge mixing ratio is always zero if it is initially zero. That is, charge neutrality is maintained. The reason that charge neutrality is maintained is that all the ions are assigned the same diffusion coefficient  $D_S$ .

Now (160) is the same as (70), and the discussion regarding (147)–(154) applies to the ion-dissipation rates. The dissipation rate of a cross-structure function (i.e., of a cospectrum) must be determined. For this purpose, we can use (70) and (160) to obtain an equation analogous to (147) for the quantity  $\overline{T' Q'_\alpha}$ . The dissipation term on the rhs of this equation is

$$\chi_{\alpha T} = (D_T + D_S) \overline{(\underline{\nabla} T') \cdot (\underline{\nabla} Q'_\alpha)} . \quad (162)$$

The discussion regarding (147)–(154) also holds for (162). If we use (160) to formulate the covariance of two different ions and momentarily distinguish their diffusion coefficients by  $D_{\alpha S}$  and  $D_{\gamma S}$ , then we likewise obtain that the dissipation rate corresponding to their cross-structure function and cospectrum is

$$\chi_{\alpha\gamma} = (D_{\alpha S} + D_{\gamma S}) \overline{(\underline{\nabla} Q'_\alpha) \cdot (\underline{\nabla} Q'_\gamma)} . \quad (163)$$

where we note that in the simulation we use  $D_{\alpha S} = D_{\gamma S} = D_S$ . Thus, (153), (155), (162), and (163) are the dissipation rates needed for the turbulence advection modeling.

Up to this point, it has been implied that  $D_T$  in (153) is the geophysical thermal diffusion coefficient. Because the grid scale of the simulation is greater than the geophysical scale on which heat diffuses, the simulation must smooth the potential temperature at a greater scale than the geophysical thermal-diffusion scale. Hence, an effective diffusion coefficient must be chosen for use in the simulation. A reasonable choice is to let  $D_T = D_S$ , which is the same value as is

used to smooth the ion variations in the simulation. However, whereas  $D_\alpha = D_S$  for all  $\alpha$  is necessary to maintain charge neutrality in the simulation,  $D_T = D_S$  is not required.

As long as there is significant separation of production and dissipation scales, that is, for a sufficiently large Reynolds number, the dissipation rates calculated from (153), (155), (162), and (163) by means of the simulation will be the same as the dissipation rates in a corresponding geophysical flow that has the same large-scale properties. The reason is that the dissipation rates are determined by the large-scale flow properties, and the calculation of local dissipation rates by means of the gradients is a useful convenience. The small geophysical diffusion coefficients cause large gradients to exist in the geophysical flow, whereas the large diffusion coefficients of the simulation cause small gradients such that the product of the diffusion coefficient and the mean-squared gradient is the same in simulated and geophysical flows.

Another possible method for determining dissipation rates is called the spectral method (also called the inertial-dissipation method). The spectral method involves spectra and cospectra of scalars in their inertial-convective range and of velocity spectra in their inertial range. In the inertial-convective range, the ion-ion power spectra and cospectra  $\Gamma_{\alpha\gamma}(k)$  are related to their corresponding dissipation rates, as in (62), and  $\Gamma_{\alpha T}(k)$  and  $\Gamma_{TT}(k)$  are analogously related to their dissipation rates. Similarly, velocity spectra are proportional to  $\varepsilon^{2/3}$  in their inertial range. Therefore, if spectra and cospectra are calculated for volumes the size of a radar's scattering volume, if inertial-convective ranges can be identified in all the scalar spectra and cospectra, and if an inertial range can be identified in the velocity spectra, then averaging over the identified inertial range can produce the dissipation rates. The quantities to be averaged are the spectra and cospectra multiplied by  $k^{5/3}$ . However, there are several disadvantages to this method. One is that laborious examination of numerous spectra and cospectra for each scattering volume must be done. Second, one must have local isotropy at spatial scales substantially greater than the dissipation scales that determine the scalar and velocity gradients; thus, the Reynolds number of the simulation must be greater for the spectral method than for the direct-dissipation method. Third, the dissipation fields as calculated by the direct-dissipation method can be output during the computer execution of a simulation, whereas the spectral method requires processing of output files. Fourth, because of the larger volume that must be averaged for the spectral method as compared with the direct-dissipation method, it is unlikely that one can subdivide the radar's scattering volume for the purpose of calculating Doppler spectral width by means of local velocity weighted by local reflectivity. On the other hand, use of the direct dissipation method requires that the simulation can accurately produce gradients; that is, numerical artifacts of the finite grid size must be avoided.

## 11. CALCULATIONS OF SPECTRA AND COSPECTRA

We have calculated the  $G_{ay}(x)$ ,  $G_{aT}(x)$ ,  $G_{TT}(x)$ ,  $\chi_{ee} G_{ee}(x)$ , and  $\chi_{eT} G_{eT}(x)$  for various multi-ion cases, both with and without coupling to temperature fluctuations and nonstationarity. Graphs of these spectra are presented in this section. Recall that the scaled spectra and cospectra ( $G$ ) are constant in a convective range. The variation with wavenumber of the spectra and cospectra ( $\Gamma$ ) is proportional to  $F(x)$  times the corresponding scaled spectra or cospectra. That is,  $F(x)$  from (61) contains the inertial-convective range power law  $x^{-5/3}$ , the viscous-convective range power law  $x^{-1}$ , and the gradual transition between these power laws. In Fig. 1, we show  $F(x)$ . It must be kept in mind that the  $G$  that we show must be multiplied by  $F(x)$  to obtain the behavior of  $\Gamma$ .

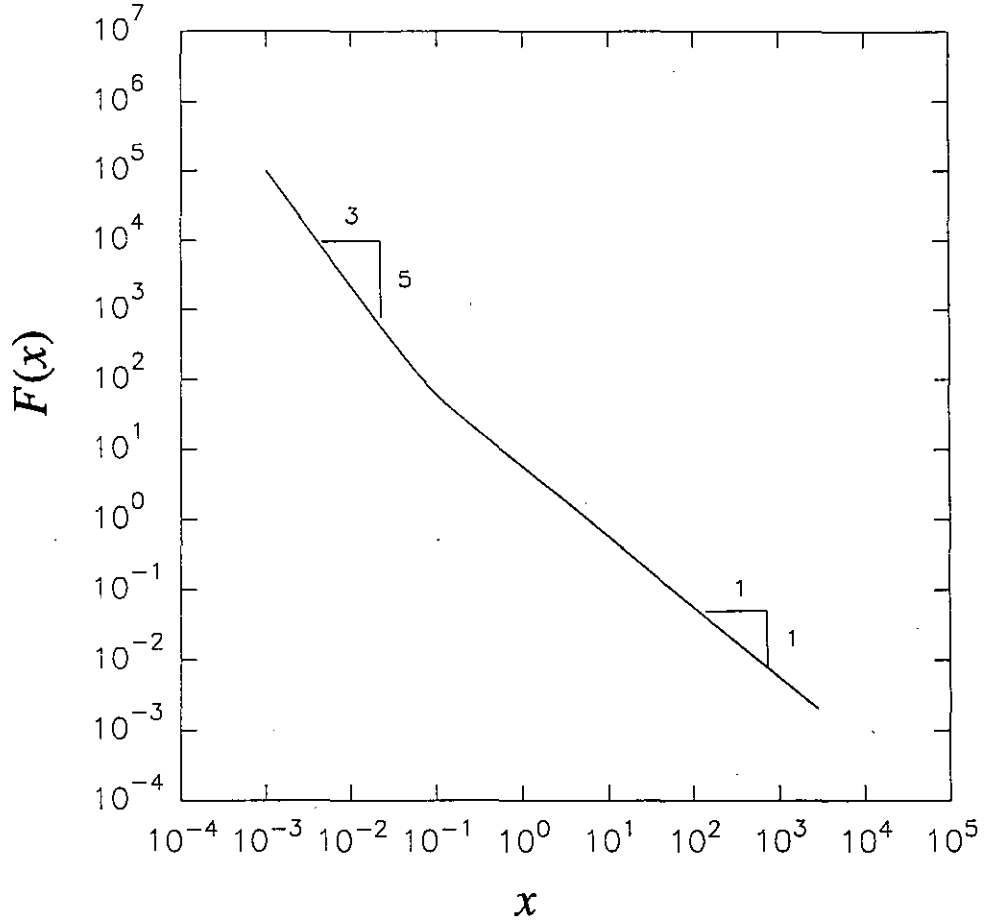


FIGURE 1. The function  $F(x)$  showing the  $x^{-5/3}$  and  $x^{-1}$  convective-range power laws and the transition between them.

To delineate the calculated cases, a table of input values is given for each case as printed by the computer. To interpret the symbols of these computer printouts, the corresponding symbols from the text and the units of the tabulated values are given in Table 1. Tables 1-11 and Figures 2-11 are grouped together at the end of this section.

If, in a printout of input, the values of  $dt\ \epsilon$ ,  $dt\ \chi(n, n)$ , and  $dt\ \chi_t(n)$  are all zero, then the stationary case is calculated; otherwise, a nonstationary case is calculated. If, in a printout of input, the values  $\omega(n)$  are all zero, then there is no coupling to temperature fluctuations; otherwise, there is such coupling.

The subsequent figures are composed of three graphs labeled *a*, *b*, and *c*, and are referred to in the text as “*a* graphs,” “*b* graphs,” and “*c* graphs.” The *a* graphs show the ion-ion mixing-ratio spectra and cospectra. The *b* graphs show the temperature spectrum and ion-temperature cospectra. The *c* graphs show the electron mixing-ratio spectrum and the electron-temperature cospectrum multiplied by their respective dissipation rates  $\chi_{ee}$  and  $\chi_{eT}$ . That is, the *c* graphs show the calculation of (95) and (99). The reason that the factors  $\chi_{ee}$  and  $\chi_{eT}$  are included on the ordinates of the *c* graphs is that  $\chi_{ee}$  and  $\chi_{eT}$  can be zero, in which case (95) and (99) show that  $G_{ee}(x)$  and  $G_{eT}(x)$  are undefined, whereas the products  $\chi_{ee} G_{ee}(x)$  and  $\chi_{eT} G_{eT}(x)$  are defined and do not vanish at all  $x$ .

Table 2 gives the printout of input for Figs. 2a–c. There are eight ions, four that are negatively charged and four that are positively charged. These ions have very diverse diffusion coefficients, as expected from the input parameters  $wn(n)$ . Figure 2a shows only the eight spectra because including the 20 cospectra would cause a confused graph. From left to right in Fig. 2a (i.e., for increasing  $x$ ), one sees the effect of progressively smaller diffusion coefficients of the progressively more massive ions. The right-most diffuse decrease at  $x > 10^3$  is caused by the diffusion of the most massive ion.

For all of our cases,  $\eta = 435\text{ cm}$  and  $\lambda_e = 2.93\text{ cm}$  so that  $\lambda_e/\eta = 6.7 \times 10^{-3}$ . Thus, the Debye shielding factor  $[1 + (x\lambda_e/\eta)^2]^{-1}$  is 0.5 at  $x = 148$  and the square of this factor is only  $4.7 \times 10^{-4}$  at  $x = 1000$ . Thus, in Fig. 2a there is a transition from nearly charge-neutral diffusion below  $x = 100$  to nearly free-ion diffusion at  $x = 1000$ . A consequence of this transition is that in Fig. 2c the electron spectrum does not extend to as great a wavenumber as does the spectrum in Fig. 2a of the most massive ion. In Fig. 2a, note that charge neutrality causes the spectra of all of the light ions to maintain some reduced level beyond the  $x$  at which they would diffuse in the absence of coupling by the electric field.

In Fig. 2b the temperature spectrum is the dashed curve and the eight ion-temperature cospectra lie nearly upon one another, blending into one wide curve. The ion-temperature cospectra all decrease rapidly at  $x$  much smaller than the  $x$  at which their corresponding ion

spectra decrease. The reason is that the governing parameter in (80) is  $P_{aT}$  in (81), and for  $D_a \ll D_T$ ,  $P_{aT}$  approaches  $\beta D_T / \nu = P_{TT}/2$ . Thus, for  $D_a \ll D_T$ , the ion-temperature cospectra all decrease rapidly at  $x$  only about  $\sqrt{2}$  greater than the  $x$  at which the temperature spectrum decreases. Figure 2b and all subsequent *b* graphs show that if  $\Omega_a \neq 0$ , the effect of coupling to temperature fluctuations vanishes as  $x$  increases beyond unity. For the same reasons, the electron-temperature cospectrum decreases rapidly beyond  $x = 1$ , which is seen in Fig. 2c and all subsequent figures labeled *c*.

The electron mixing-ratio spectrum in Fig. 2c does not have a range in which it is nearly constant; such a range would correspond to a viscous-convective range. The reason is clear from Fig. 2a, as follows: The electron spectrum follows from the spectrum of ionic net charge; that is, the electron spectrum is what it must be on the basis of approximate charge neutrality.

Table 3 and Figs. 3a–c show the case of a light positive ion and a very massive negative ion. The ion-ion cospectrum is included in Fig. 3a. (Such cospectra are included on all subsequent *a* graphs.) The light ion's spectrum and the cospectrum decrease rapidly beyond  $x = 100$  because the Debye shielding becomes small beyond  $x = 100$  such that charge neutrality is relaxed. This is also the reason for the decrease of the electron spectrum for  $x$  beyond 100 in Fig. 3c.

In Figs. 3b,c the cospectra decrease rapidly beyond  $x = 1$  for the same reasons as given for Figs. 2b,c. This is true for all subsequent graphs of ion-temperature and electron-temperature cospectra. Therefore, this point need not be repeated.

For Figs. 2c and 3c, the electron spectrum (and the electron-temperature spectrum, as well) is zero at our initial  $x$  value of  $10^{-3}$ . This is because the parameters in Tables 2 and 3 give, from (96) and (98),  $\chi_{ee} = 0$  and  $\chi_{eT} = 0$ . Thus,  $\chi_{ee} G_{ee}(x)$  [and also  $\chi_{eT} G_{eT}(x)$ ] increases from zero to attain appreciable values only at large enough  $x$  such that some diffusion process requires the electrons to establish approximate charge neutrality.

Table 4 and Figs. 4a–c show a case with the same input parameters as Table 3 except that the cospectral dissipation rate is negative such that  $\chi_{ee}$  is no longer zero, as is evident from Fig. 4c. Figure 4a is similar to Fig. 3a except that the cospectrum in Fig. 4a crosses zero at  $x = 0.537$  to become negative at  $x > 0.537$ . The resultant effect on the electron spectrum in Fig. 4c is the downward step. For  $x > 1$ , the curves in Figs. 3a–c and 4a–c are the same (and have the same interpretation) except for the opposite sign of the ion-ion cospectrum.

If the cospectral dissipation rate  $\chi_{ay}$  is negative, then  $\Gamma_{ay}(k)$  is negative at the initial  $x$  value. Then,  $G_{ay}(x)$  is initially positive because, according to (58), it is the ratio of two negative numbers. That  $G_{ay}(x)$  is initially positive corresponds to the initial value of unity in (63). Since the cospectrum  $G_{ay}(x)$  in Fig. 4a is positive for  $x < 0.537$  and negative for  $x > 0.537$ ,

it follows that  $\Gamma_{\alpha\gamma}(x)$  is negative for  $x < 0.537$ , as required by a negative  $\chi_{\alpha\gamma}$ , and positive for  $x > 0.537$ . A negative value of the cospectral dissipation rate can arise from turbulent mixing in the presence of ambient gradients of a different sign for the two mixing ratios.

Table 5 and Figs. 5a–c give a nonstationary case with all other parameters the same as in Table 4. At small  $x$ , one can see in Figs. 5a–c the effect of the boundary conditions for the nonstationary case. The boundary conditions are (115) for  $G_{\alpha\gamma}$ , (118) for  $G_{TT}$ , and (127) with  $B_{\alpha T} = 0$  for  $G_{\alpha T}$ . For  $x > 1$ , the curves in Figs. 5a–c are slightly lower than in Figs. 4a–c, but the two sets of figures can be made congruent at  $x > 1$  by a slight shift of the ordinates. The effect of nonstationarity is most important at low wavenumbers.

Table 6 and Figs. 6a–c show the same stationary case as in Table 4 and Figs. 4a–c except that there is coupling to the temperature fluctuations, i.e.,  $\Omega_a \neq 0$ . For  $x > 1$ , the curves in Fig. 6a are congruent with the curves in Fig. 4a. For Figs. 4b,c and 6b,c, there is congruence for  $x > 0.1$ .

Table 7 and Figs. 7a–c combine the nonstationary case of Table 5 with the same coupling to temperature fluctuations as in Table 6. For  $x > 10^{-2}$ , one can obtain congruence of the curves in Fig. 7a with curves in Figs. 5a and 6a; for Figs. 5b,c, 6b,c, and 7b,c, there is congruence for  $x > 0.1$  with the exception that curves in Fig. 6c are slightly higher than in Fig. 7c. Similar to the comparison of Figs. 5a–c with Figs. 4a–c, Figs. 7a–c become congruent with Figs. 4a–c at  $x > 0.1$ , given a slight shift of the ordinates. The effects of nonstationarity and of coupling to temperature fluctuations change the shape of the curves for  $x < 1$ .

In the previous cases, all the  $\chi_{\alpha\gamma}$  had unit magnitude. Table 8 and Figs. 8a–c show a stationary case with no coupling to temperature fluctuations for a massive negative ion having a dissipation rate much greater than that of a light positive ion and a yet smaller positive cospectral dissipation rate. The negative ion is not so massive as to cause ionic charge density at spatial scales as small as  $\lambda_e$ . Consequently, all spectra in Fig. 8a and the electron spectrum in Fig. 8c decrease rapidly at  $x$  such that the massive negative ion undergoes ambipolar diffusion. The distinctive feature of this case is the increase of the positive-ion spectrum and of the ion-ion cospectrum for  $x$  such that diffusion of the positive ion is effective. When the positive ions diffuse, their electrical attraction to the negative ions causes the positive-ion fluctuations to increase and the electron fluctuations to decrease, which is the opposite of the case in Figs. 3a,c. The relatively large dissipation rate of the negative ions corresponds to relatively large fluctuations of negative ions that can attract the more mobile positive ions.

Table 9 and Figs. 9a–c show a nonstationary case with all other parameters the same as in Table 8. The curves in Figs. 9a–c are congruent with those in Figs. 8a–c for  $x > 0.1$ .



Table 10 and Figs. 10a–c show a stationary case with all parameters the same as in Table 8 except for coupling to temperature fluctuations, i.e.,  $\Omega_\alpha \neq 0$ . With the exception of the electron-temperature and ion-temperature cospectra, the curves in Figs. 10a–c are congruent with those in Figs. 8a–c for  $x > 0.01$ , except for  $\chi_{eT} G_{eT}(x)$ , for which congruence is obtained for  $x > 0.3$ . Table 9 and Figs. 9a–c show a nonstationary case with no coupling to temperature fluctuations, whereas Table 10 and Figs. 10a–c show a stationary case with coupling to temperature fluctuations; all other inputs are the same in these two cases. For  $x > 0.3$ , all curves in Figs. 10a–c are congruent with the curves in Figs. 9a–c.

Our final case is shown in Table 11 and Figs. 11a–c. The case is like those in Tables 8, 9, and 10, except that it includes both nonstationarity and coupling to temperature fluctuations. The case in Figs. 11a–c has features in common with those previous cases, including congruence of the curves with corresponding curves for  $x > 0.1$ , and in some cases there is congruence for  $x < 0.1$ .

Let us return to considering Figs. 5a, 6a, and 7a. The solid curves are negative in the ranges  $0.48 < x < 0.58$ ,  $0.52 < x < 0.55$ , and  $0.48 < x < 0.58$  for these three figures, respectively. These ranges are in the middle of the dip of the curves in these figures. The solid curves are power spectra. Power spectra cannot be negative; therefore, there is an error in the ranges where the solid curves are negative, however brief these ranges may be.

These three figures are the same case as presented in Fig. 4a, except Fig. 5a includes nonstationary input, Fig. 6a includes coupling to temperature fluctuations, and Fig. 7a includes both aspects (compare inputs in Tables 4–7). The approximations made in section 8 in deriving boundary conditions for nonstationary cases and for cases including coupling to temperature fluctuations introduce error that can lead to negative power spectra. The approximation of neglect of the time derivative in (91) can also lead to such error. The cases presented in Figs. 5a, 6a, and 7a have initial conditions that deviate significantly from unity, i.e., from (63). This is especially evident in Figs. 5a and 7a, wherein the solid curve begins nearer to  $10^3$  than to unity. Because of this significant deviation from unity of the boundary condition and the approximation in (91), we obtain some error, including negative power spectra in places.

Clearly, one cannot have very strong nonstationarity or strong coupling to temperature fluctuations if the result is to be accurate. Nevertheless, for  $x > 1$  there is little difference between the curves for Figs. 5a, 6a, and 7a, as compared to the corresponding stationary and uncoupled case in Fig. 4a. Thus, the errors will have little effect on calculation of radar scatter for Bragg wavenumbers that exceed the inverse of Kolmogorov's microscale.

**TABLE 1.** The correspondence between symbols in Tables 2–11 and symbols in the text.

Table Symbols	Corresponding Text Symbols
$n =$	$n$ , number of ion species
$cd =$	$N_e$ (cm <sup>-3</sup> ), electron concentration
$eps =$	$\varepsilon$ (cm <sup>2</sup> s <sup>-3</sup> ), energy-dissipation rate
$nair =$	$N$ (cm <sup>-3</sup> ), neutral's concentration
$temp =$	$T$ (K), absolute temperature
$r(n)^{\S} =$	$N_a/N_e$ , ion-electron concentration ratio
$s(n)^{\S} =$	$S_a$ , charge of ion in units of $e$
$wn(n)^{\S} =$	$n_w$ , number of H <sub>2</sub> O in hydrated-proton ion
$chi(n,n)^{\S} =$	$\chi_{\alpha\gamma}$ (s <sup>-1</sup> ), ion-ion dissipation rate
$chi\ t(n)^{\S} =$	$\chi_{\alpha T}$ (K s <sup>-1</sup> ), ion-temperature dissipation rate
$chi\ tt =$	$\chi_{TT}$ (K <sup>2</sup> s <sup>-1</sup> ), temperature-dissipation rate
$dt\ eps =$	$d\varepsilon/dt$ (cm <sup>2</sup> s <sup>-4</sup> ), time derivative of $\varepsilon$
$dt\ chi(n,n)^{\S} =$	$d\chi_{\alpha\gamma}/dt$ (s <sup>-2</sup> ), time derivative of $\chi_{\alpha\gamma}$
$dt\ chi\ t(n)^{\S} =$	$d\chi_{\alpha T}/dt$ (K s <sup>-2</sup> ), time derivative of $\chi_{\alpha T}$
$dt\ chi\ tt =$	$d\chi_{TT}/dt$ (K <sup>2</sup> s <sup>-2</sup> ), time derivative of $\chi_{TT}$
$omega(n)^{\S} =$	$\Omega_a$ (K <sup>-1</sup> s <sup>-1</sup> ), coupling to temperature fluctuations (39)

<sup>\S</sup>For  $\alpha = 1$  to  $n$  and  $\beta = 1$  to  $n$ , we have the arrays of dimension  $(n)$  and  $(n, n)$ .

**TABLE 2.** Computer inputs for the calculation shown in Figs. 2a–c. See Table 1 for the meaning of the symbols.

---

```

# Each variable is preceded by a comment stating its name.
#
# n
8
# cd
1000
# eps
100
# nair
 $1.654 \times 10^{14}$ 
# temp
180.65
# Arrays. Arrays are listed as x(i) or y(j,i) or z(k,j,i), with the
# first subscript varying fastest, so after y(1,1) comes y(2,1)
# r(n)
#   First, 4 positive ions:
      2.000000000000
      2.000000000000
      2.000000000000
      2.000000000000
#   Next, 4 negative ions:
      2.000000000000
      2.000000000000
      2.000000000000
      1.000000000000
# s(n)
#   First, 4 positive ions:
      1.000000000000
      1.000000000000
      1.000000000000
      1.000000000000
#   Next, 4 negative ions:
      -1.000000000000
      -1.000000000000
      -1.000000000000
      -1.000000000000
# wn(n)
#   First, 4 positive ions:
16.
256.
65536.
4294967296.
#   Next, 4 negative ions:
81.
6561

```

---

TABLE 2. (continued)

---

43046721.  
120000000.  
# chi (n, n)  
# 64.  
[All 64 elements are 1.0]  
# chi t (n)  
# 8 here.  
[All 8 elements are 1.0]  
# chi t t  
1.  
# dt eps  
0.  
# dt chi (n, n)  
[All 64 elements are zero]  
# dt chi t (n)  
[All 8 elements are zero]  
# dt chi t t  
0.  
# omega (n)  
[All 8 elements are zero]

---

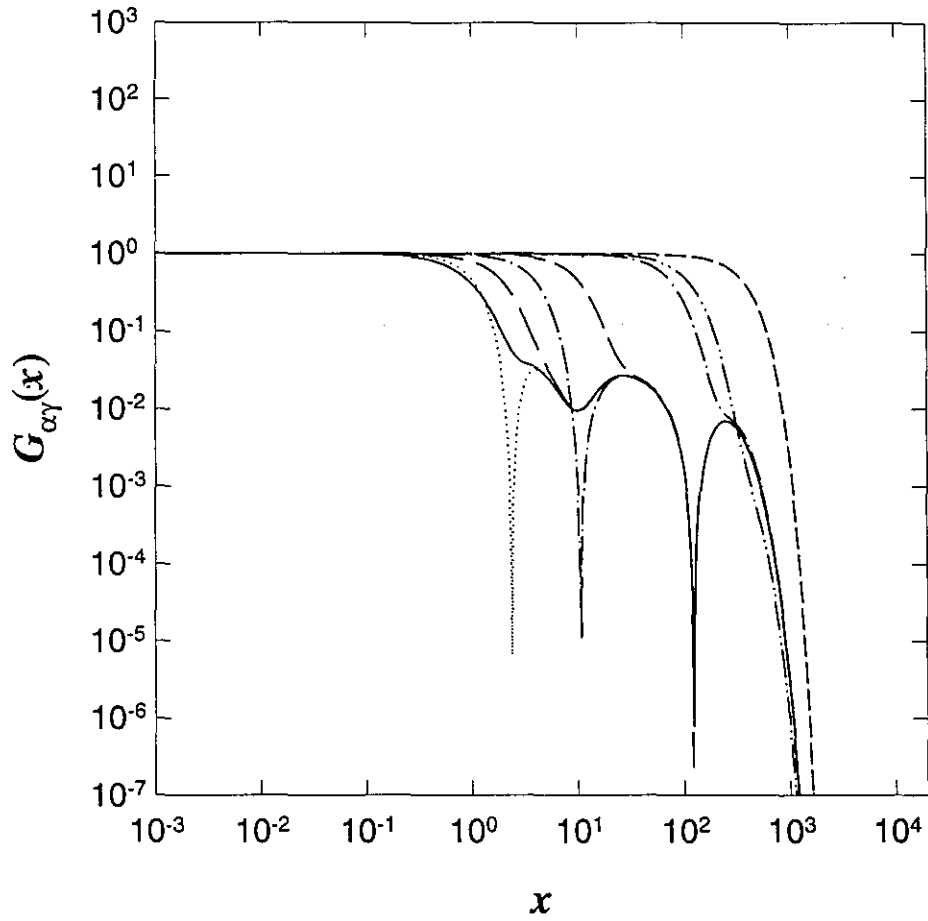


FIGURE 2a. The power spectra of the eight ion species. From left to right, the curves first depart from unity in the order of increasing  $n_w$  [wn(n) in Table 2]. In the order of increasing  $n_w$ , the signs of the charges in Table 2 are +, -, +, -, +, -, -, +. The diffusion modes of the negative ions cause a downward spike in their spectra corresponding to their spectra closely approaching zero. Inputs are listed in Table 2.

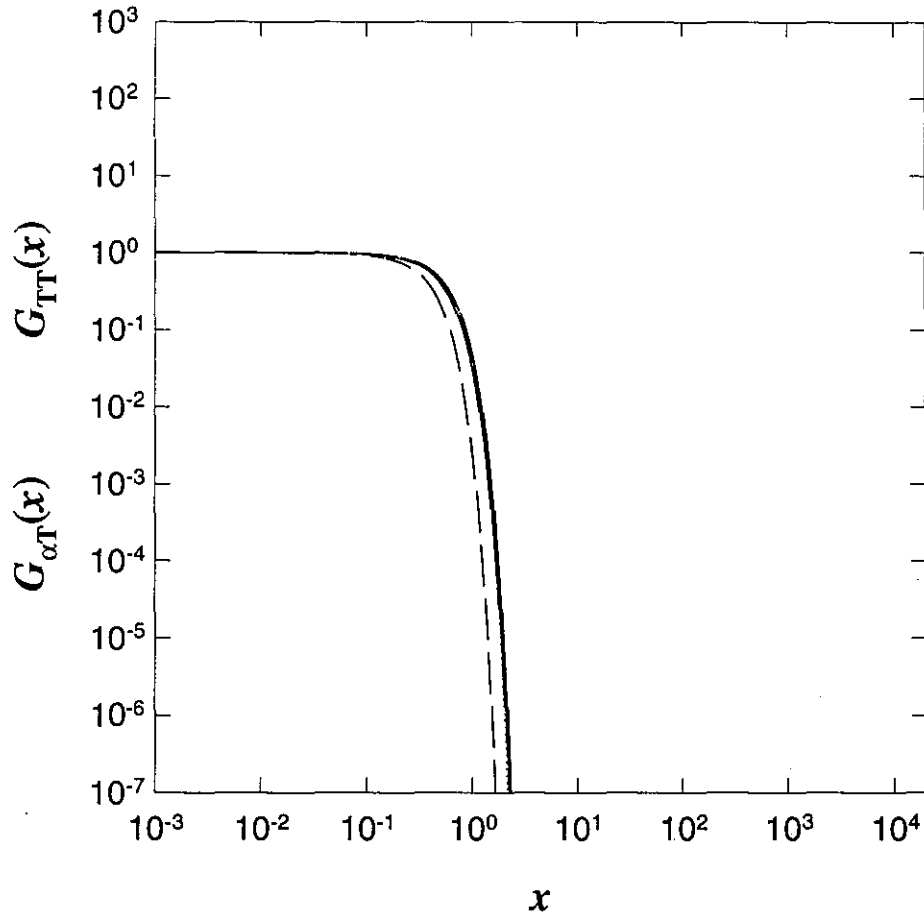


FIGURE 2b. The temperature spectrum (dashed curve) and eight ion-temperature cospectra that lie so near to one another that they blend into the single thick curve. Inputs are listed in Table 2.

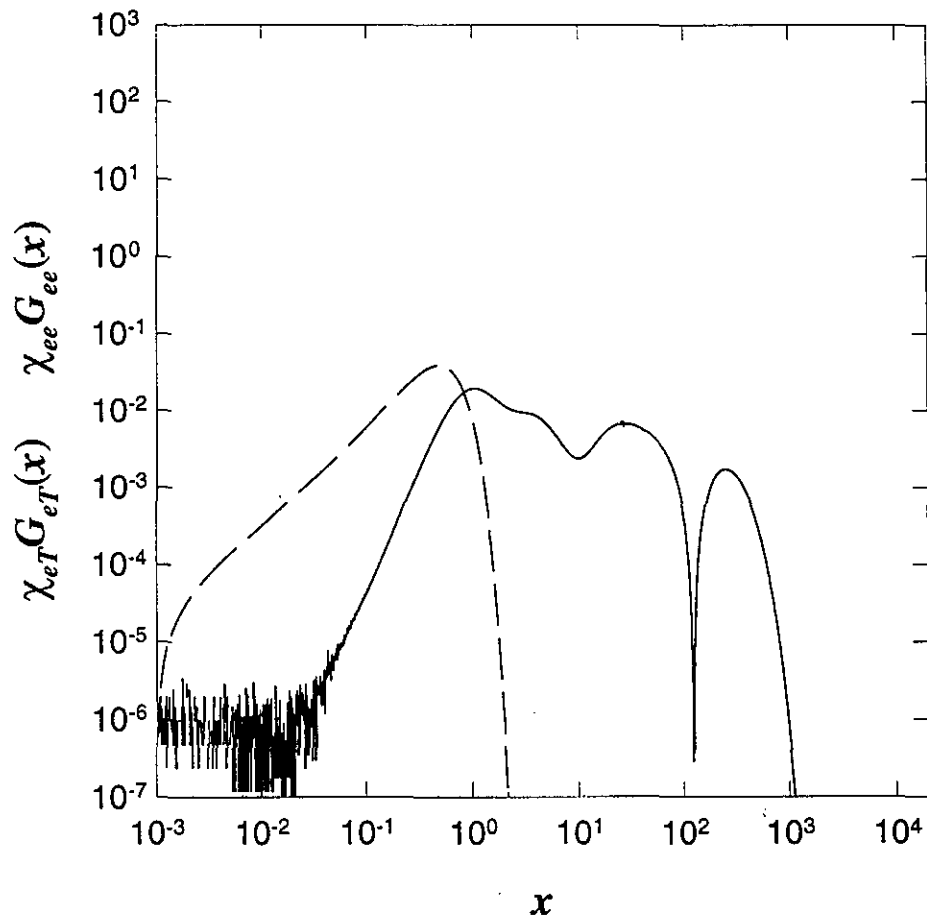


FIGURE 2c. The electron mixing-ratio spectrum (solid curve) and the cospectrum of potential temperature with electron mixing ratio (dashed curve). Inputs are listed in Table 2.

**TABLE 3.** Computer inputs for the calculation shown in Figs. 3a–c. See Table 1 for the meaning of the symbols.

---

```

# Each variable is preceded by a comment stating its name.
# n
2
# cd
1000
# eps
100
# nair
 $1.654 \times 10^{14}$ 
# temp
180.65
# Arrays. Arrays are listed as x(i) or y(j,i) or z(k,j,i), with the
# first subscript varying fastest, so after y(1,1) comes y(2,1)
# r (n)
2.000000000000
1.000000000000
# s (n)
1.000000000000
-1.000000000000
# wn (n)
2.
 $1 \times 10^{12}$ 
# chi (n, n)
1.
1.
1.
1.
# chi t (n)
1.
1.
# chi t t
1.
# dt eps
0.
# dt chi (n, n)
0.
0.
0.
0.
# dt chi t (n)
0.
0.
# dt chi t t
0.
# omega (n)
0.
0.

```

---



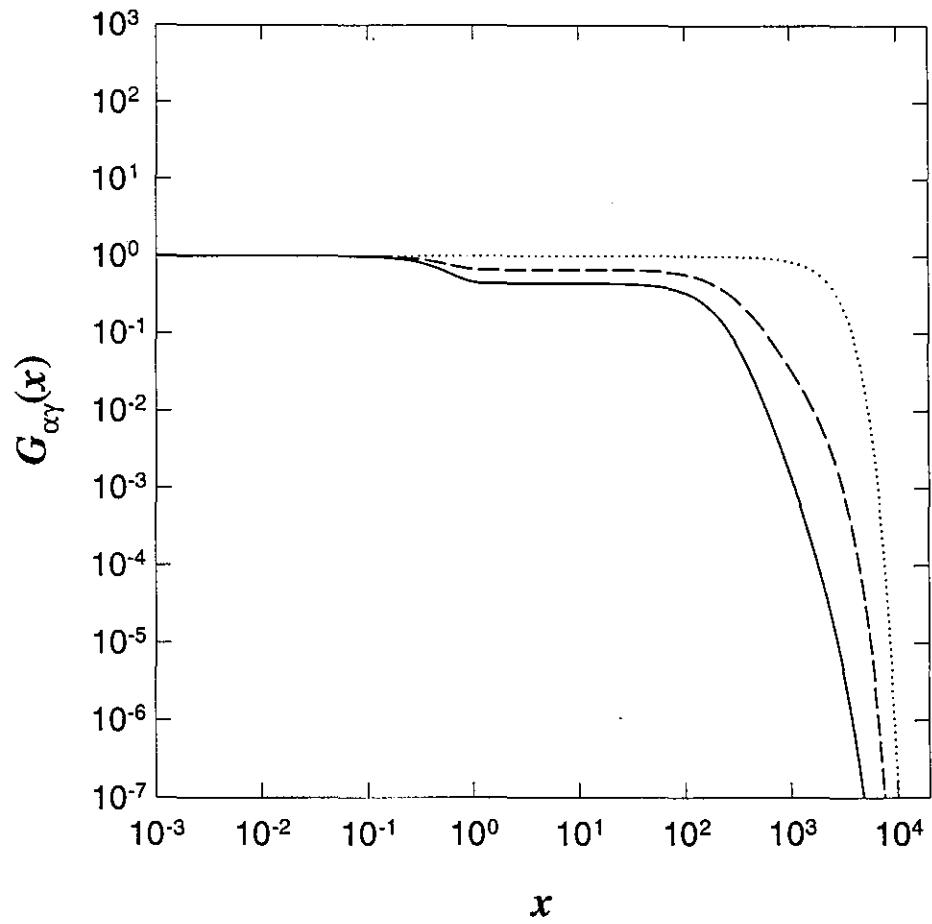


FIGURE 3a. The positive-ion spectrum (solid curve), the negative-ion spectrum (short-dashed curve), and the cospectrum (medium-dashed curve) that is always positive. Inputs are listed in Table 3.

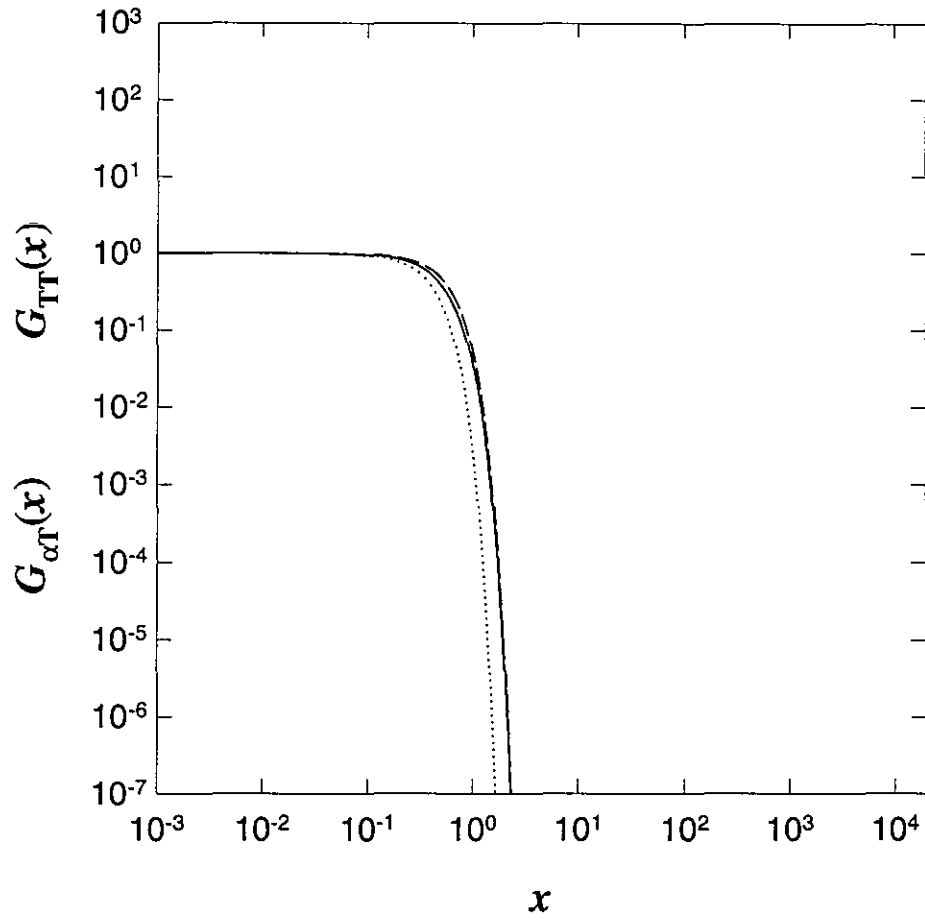


FIGURE 3b. The potential temperature-ion cospectra for the first (solid curve) and second (long-dashed curve) ions. The short-dashed curve is the potential temperature spectrum. Inputs are listed in Table 3.

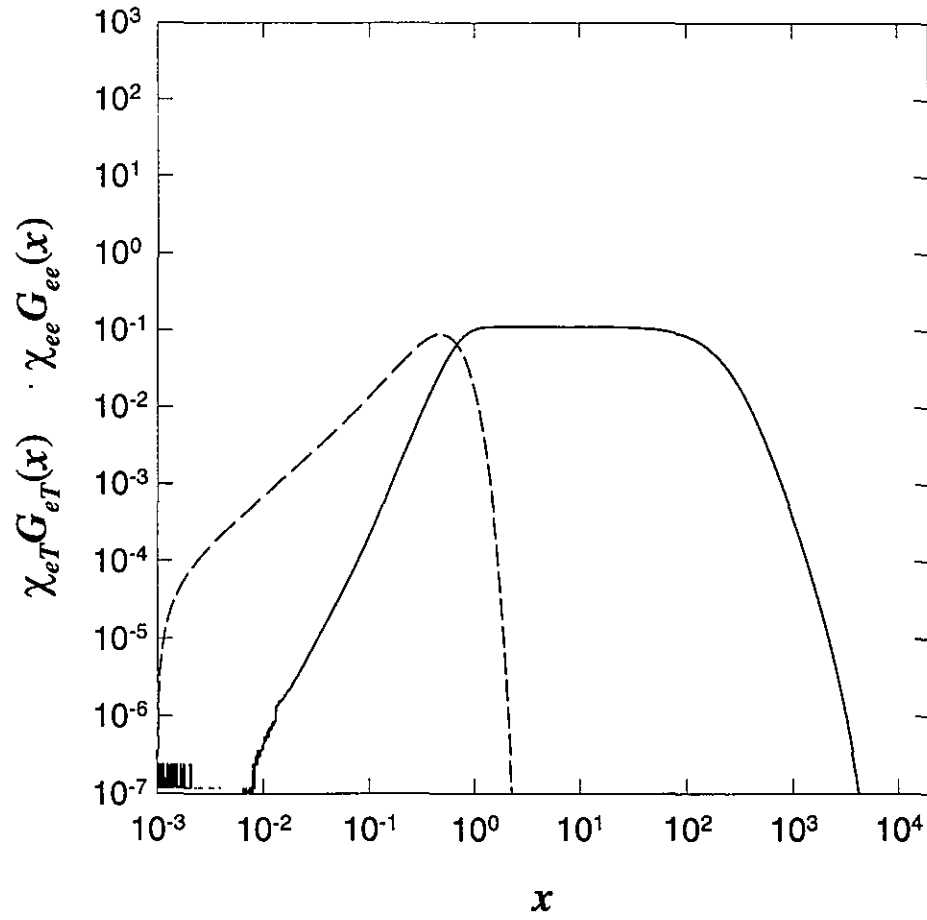


FIGURE 3c. The electron mixing-ratio spectrum (solid curve) and the cospectrum of potential temperature with electron mixing ratio (dashed curve). Inputs are listed in Table 3.

**TABLE 4.** Computer inputs for the calculation shown in Figs. 4a–c. See Table 1 for the meaning of the symbols.

---

```

# Each variable is preceded by a comment stating its name.
# n
2
# cd
1000
# eps
100
# nair
 $1.654 \times 10^{14}$ 
# temp
180.65
# Arrays. Arrays are listed as x(i) or y(j,i) or z(k,j,i), with the
# first subscript varying fastest, so after y(1,1) comes y(2,1)
# r(n)
2.000000000000000
1.000000000000000
# s(n)
1.000000000000000
-1.000000000000000
# wn(n)
2.
 $1 \times 10^{12}$ 
# chi(n,n)
1.
-1.
-1.
1.
# chi t(n)
1.
1.
# chi t t
1.
# dt eps
0.
# dt chi(n,n)
0.
0.
0.
0.
# dt chi t(n)
0.
0.
# dt chi t t
0.
# omega(n)
0.
0.
```

---

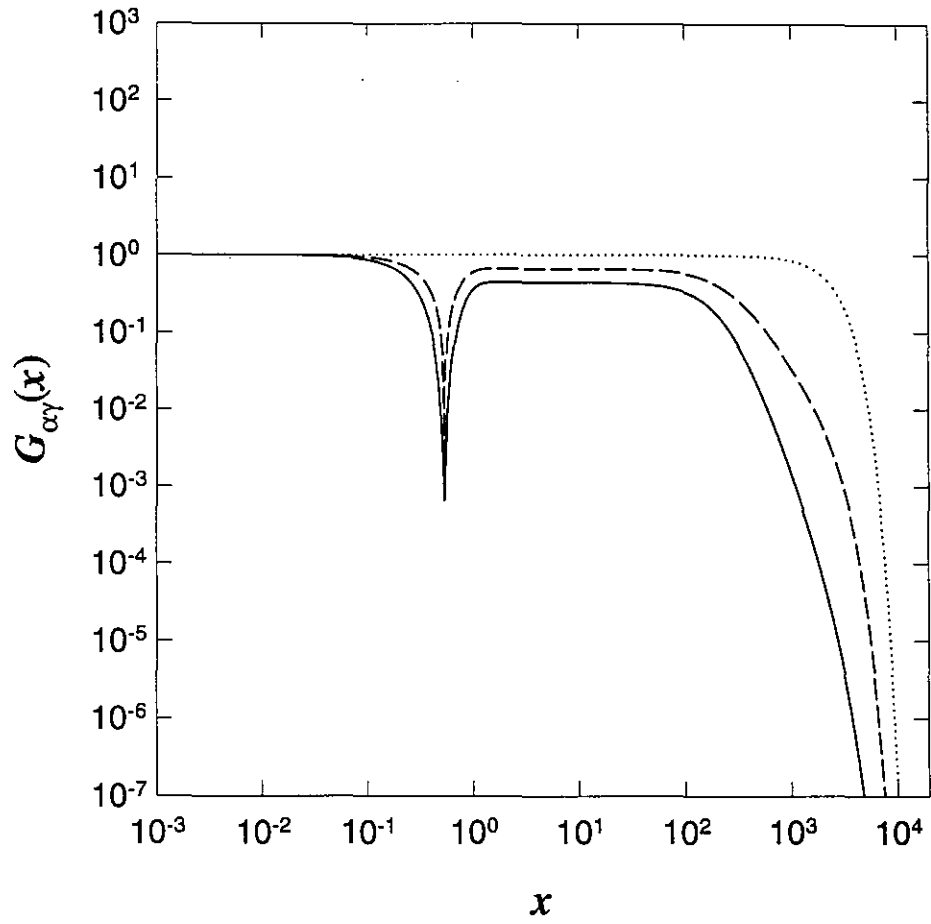


FIGURE 4a. The positive-ion spectrum (solid curve), the negative-ion spectrum (short-dashed curve), and the cospectrum (medium-dashed curve) that is negative for  $x > 0.537$ . Inputs are listed in Table 4.

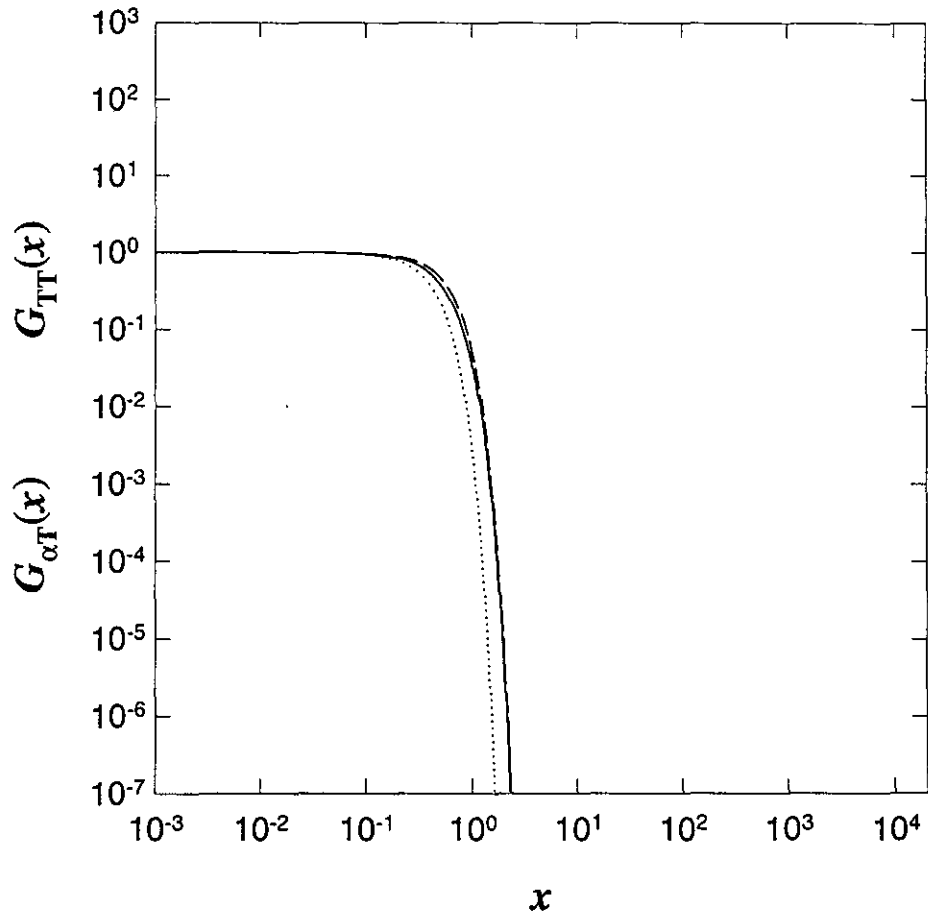


FIGURE 4b. Potential temperature-ion cospectra for the first (solid curve) and second (long-dashed curve) ions. The short-dashed curve is the potential temperature spectrum. Inputs are listed in Table 4.

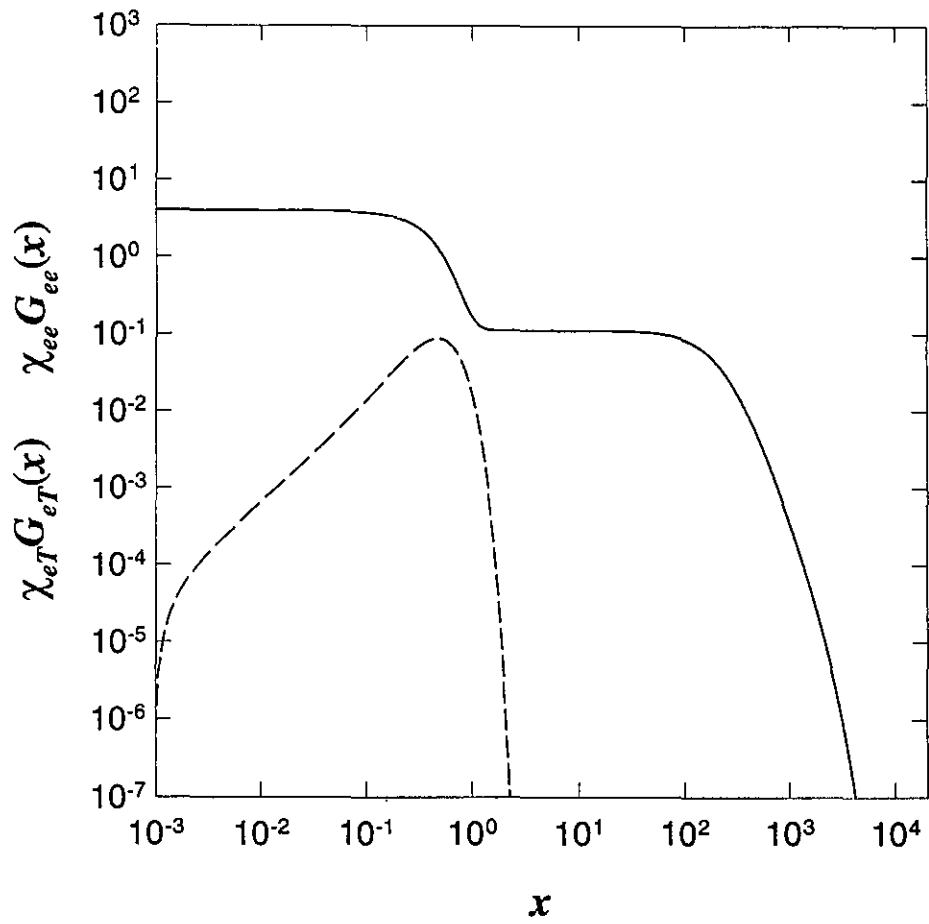


FIGURE 4c. The electron mixing-ratio spectrum (solid curve) and the cospectrum of potential temperature with electron mixing ratio (dashed curve). Inputs are listed in Table 4.

**TABLE 5.** Computer inputs for the calculation shown in Figs. 5a–c. See Table 1 for the meaning of the symbols.

---

```

# Each variable is preceded by a comment stating its name.
# n
2
# cd
1000
# eps
100
# nair
 $1.654 \times 10^{14}$ 
# temp
180.65
# Arrays. Arrays are listed as x(i) or y(j,i) or z(k,j,i), with the
# first subscript varying fastest, so after y(1,1) comes y(2,1)
# r (n)
    2.00000000000000
    1.00000000000000
# s (n)
    1.00000000000000
    -1.00000000000000
# wn (n)
2.
 $1 \times 10^{12}$ 
# chi (n, n)
1.
-1.
-1.
1.
# chi t (n)
1.
1.
# chi t t
1.
# dt eps
 $-1 \times 10^{-1}$ 
# dt chi (n, n)
 $4.5 \times 10^{-3}$ 
 $5 \times 10^{-4}$ 
 $5.3 \times 10^{-4}$ 
 $3 \times 10^{-4}$ 
# dt chi t (n)
 $4 \times 10^{-4}$ 
 $1 \times 10^{-3}$ 
# dt chi t t
 $2.3 \times 10^{-3}$ 
# omega (n)
0.
0.

```

---



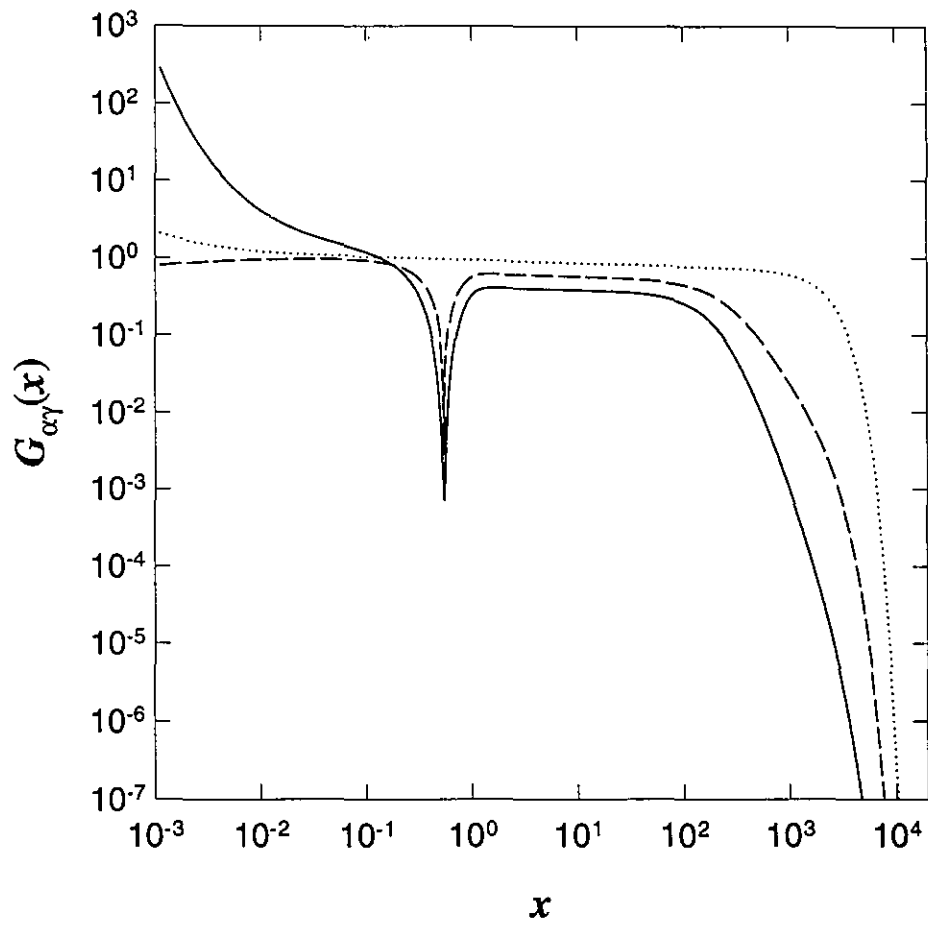


FIGURE 5a. The positive-ion spectrum (solid curve), the negative-ion spectrum (short-dashed curve), and the cospectrum (medium-dashed curve) that is negative for  $x > 0.537$ . Inputs are listed in Table 5.

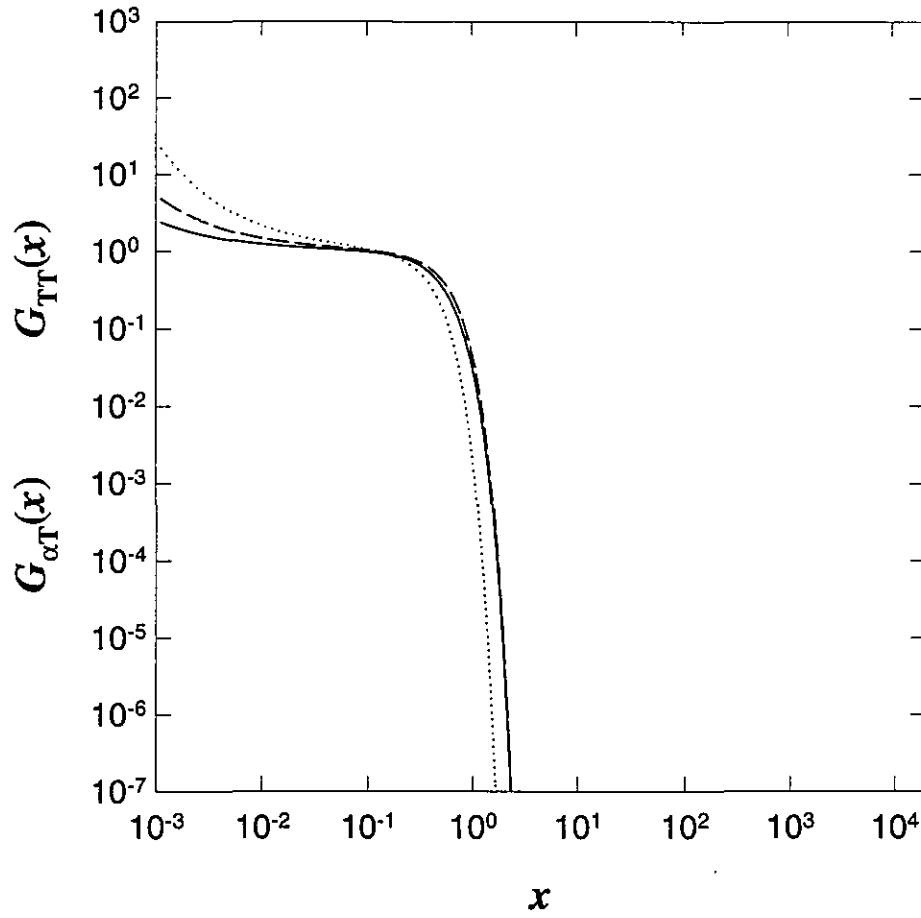


FIGURE 5b. Potential temperature-ion cospectra for the first (solid curve) and second (long-dashed curve) ions. The short-dashed curve is the potential temperature spectrum. Inputs are listed in Table 5.

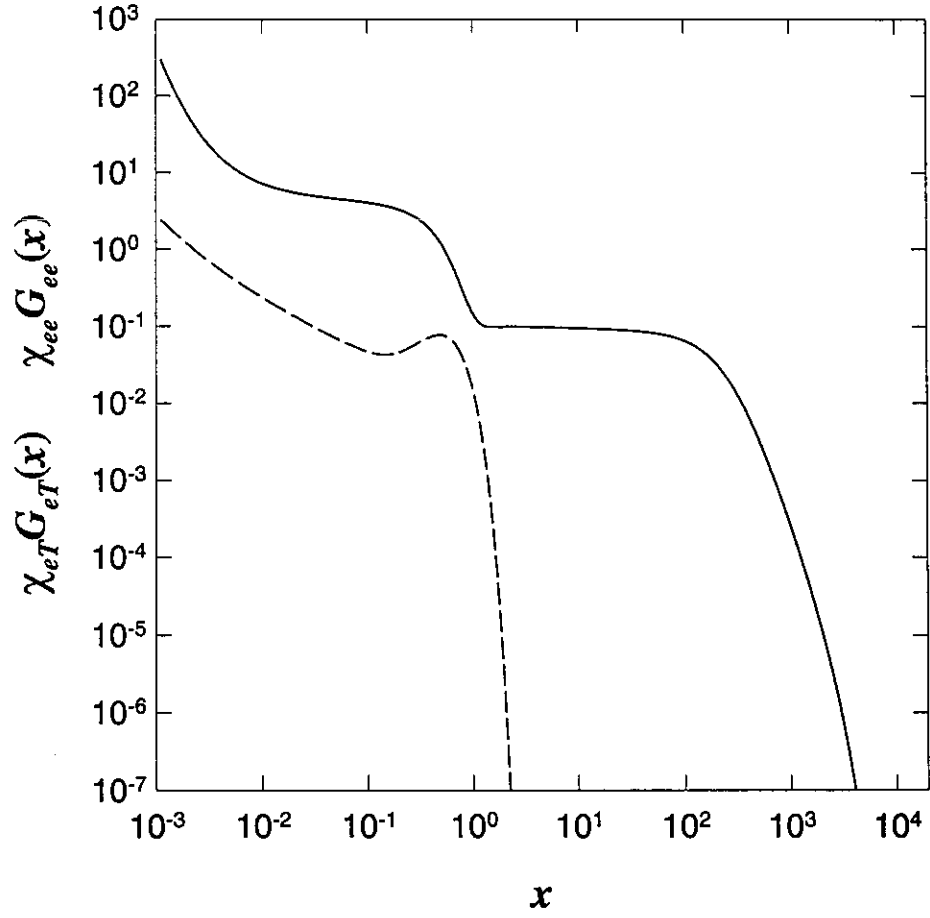


FIGURE 5c. The electron mixing-ratio spectrum (solid curve) and cospectrum of potential temperature with electron mixing ratio (dashed curve) that is negative for  $x > 0.134$ . Inputs are listed in Table 5.

**TABLE 6.** Computer inputs for the calculation shown in Figs. 6a–c. See Table 1 for the meaning of the symbols.

---

```

# Each variable is preceded by a comment stating its name.
# n
2
# cd
1000
# eps
100
# nair
 $1.654 \times 10^{14}$ 
# temp
180.65
# Arrays. Arrays are listed as x(i) or y(j,i) or z(k,j,i), with the
# first subscript varying fastest, so after y(1,1) comes y(2,1)
# r (n)
    2.000000000000
    1.000000000000
# s (n)
    1.000000000000
    -1.000000000000
# wn (n)
2.
 $1 \times 10^{12}$ 
# chi (n, n)
1.
-1.
-1.
1.
# chi t (n)
1.
1.
# chi t t
1.
# dt eps
0.
# dt chi (n, n)
0.
0.
0.
0.
# dt chi t (n)
0.
0.
# dt chi t t
0.
# omega (n)
 $1 \times 10^{-5}$ 
 $3 \times 10^{-3}$ 

```

---

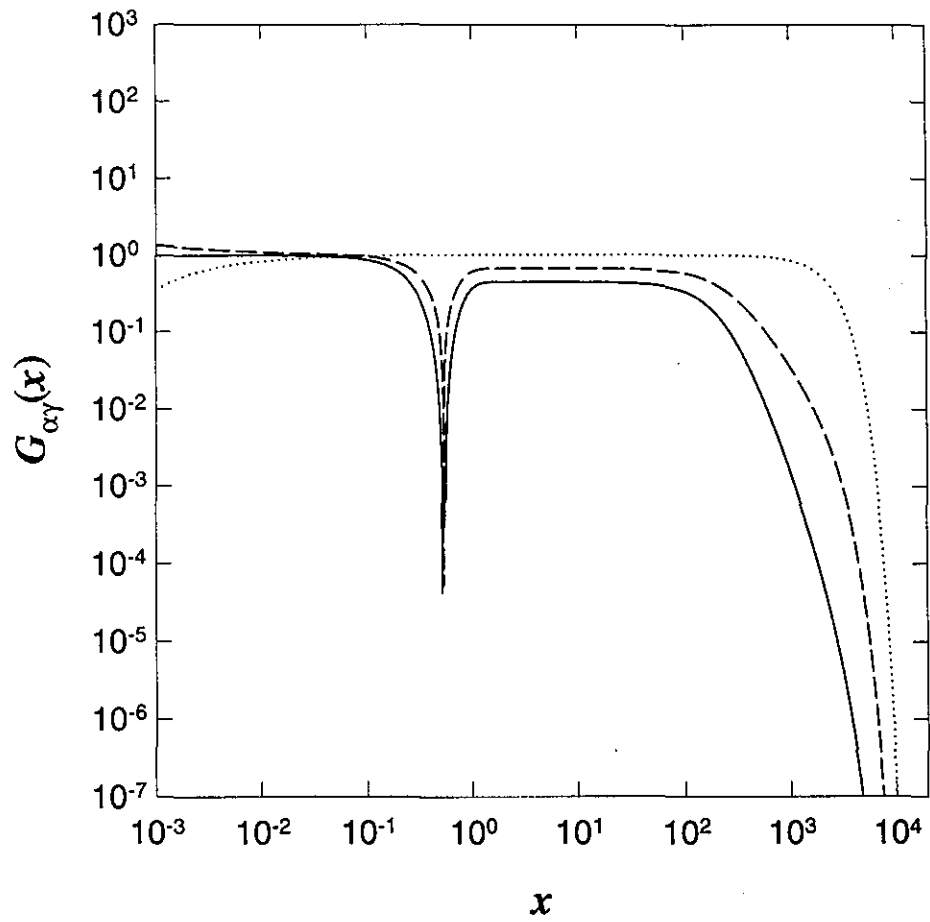


FIGURE 6a. The positive-ion spectrum (solid curve), the negative-ion spectrum (short-dashed curve), and the cospectrum (medium-dashed curve) that is negative for  $x > 0.537$ . Inputs are listed in Table 6.

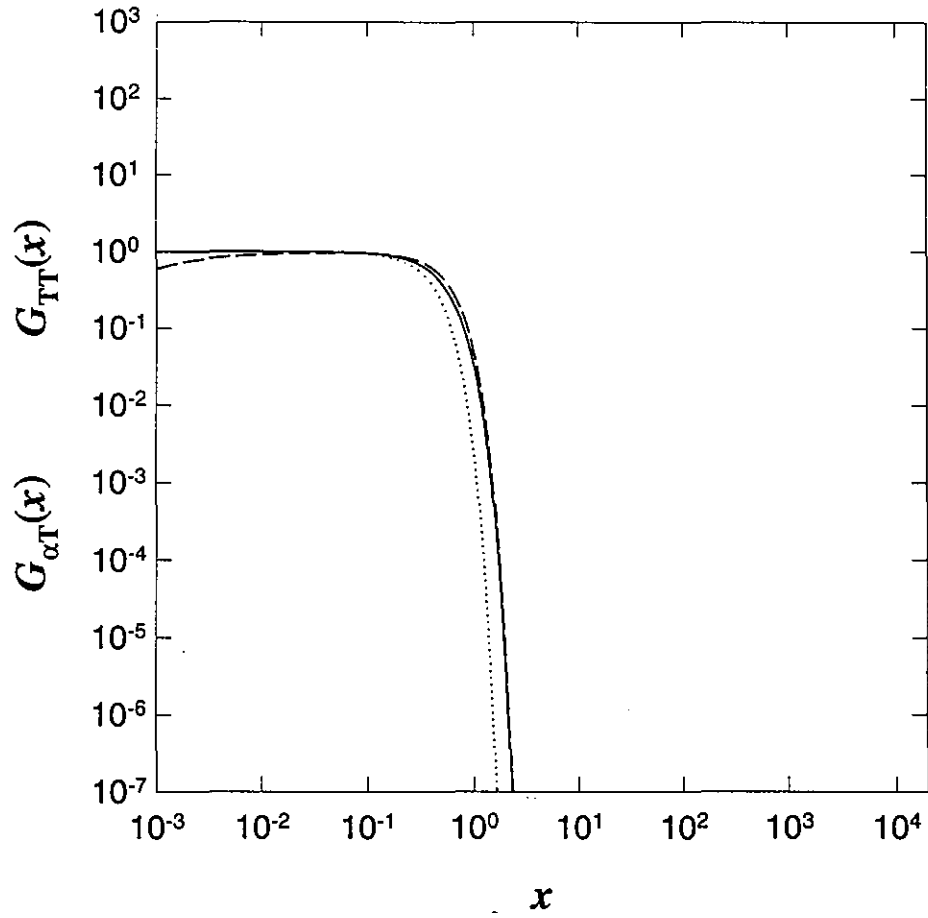


FIGURE 6b. Potential temperature-ion cospectra for the first (solid curve) and second (long-dashed curve) ions. The short-dashed curve is the potential temperature spectrum. Inputs are listed in Table 6.

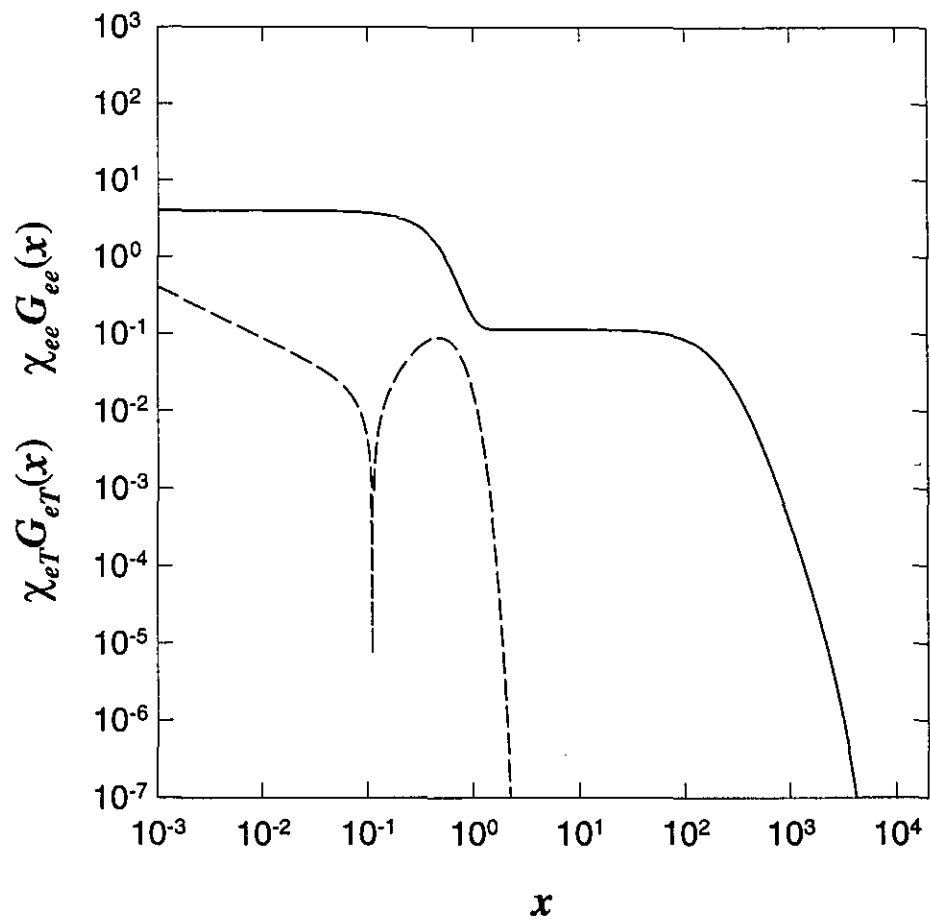


FIGURE 6c. The electron mixing-ratio spectrum (solid curve) and the cospectrum of potential temperature with electron mixing ratio (dashed curve) that is negative for  $x > 0.111$ . Inputs are listed in Table 6.

**TABLE 7.** Computer inputs for the calculation shown in Figs. 7a–c. See Table 1 for the meaning of the symbols.

---

```

# Each variable is preceded by a comment stating its name.
# n
2
# cd
1000
# eps
100
# nair
 $1.654 \times 10^{14}$ 
# temp
180.65
# Arrays. Arrays are listed as x(i) or y(j,i) or z(k,j,i), with the
# first subscript varying fastest, so after y(1,1) comes y(2,1)
# r(n)
2.00000000000000
1.00000000000000
# s(n)
1.00000000000000
-1.00000000000000
# wn(n)
2.
 $1 \times 10^{12}$ 
# chi(n,n)
1.
-1.
-1.
1.
# chi t(n)
1.
1.
# chi t t
1.
# dt eps
 $-1 \times 10^{-1}$ 
# dt chi(n,n)
 $4.5 \times 10^{-3}$ 
 $5 \times 10^{-4}$ 
 $5.3 \times 10^{-4}$ 
 $3 \times 10^{-4}$ 
# dt chi t(n)
 $4 \times 10^{-4}$ 
 $1 \times 10^{-3}$ 
# dt chi t t
 $2.3 \times 10^{-3}$ 
# omega(n)
 $1 \times 10^{-5}$ 
 $3 \times 10^{-3}$ 

```

---



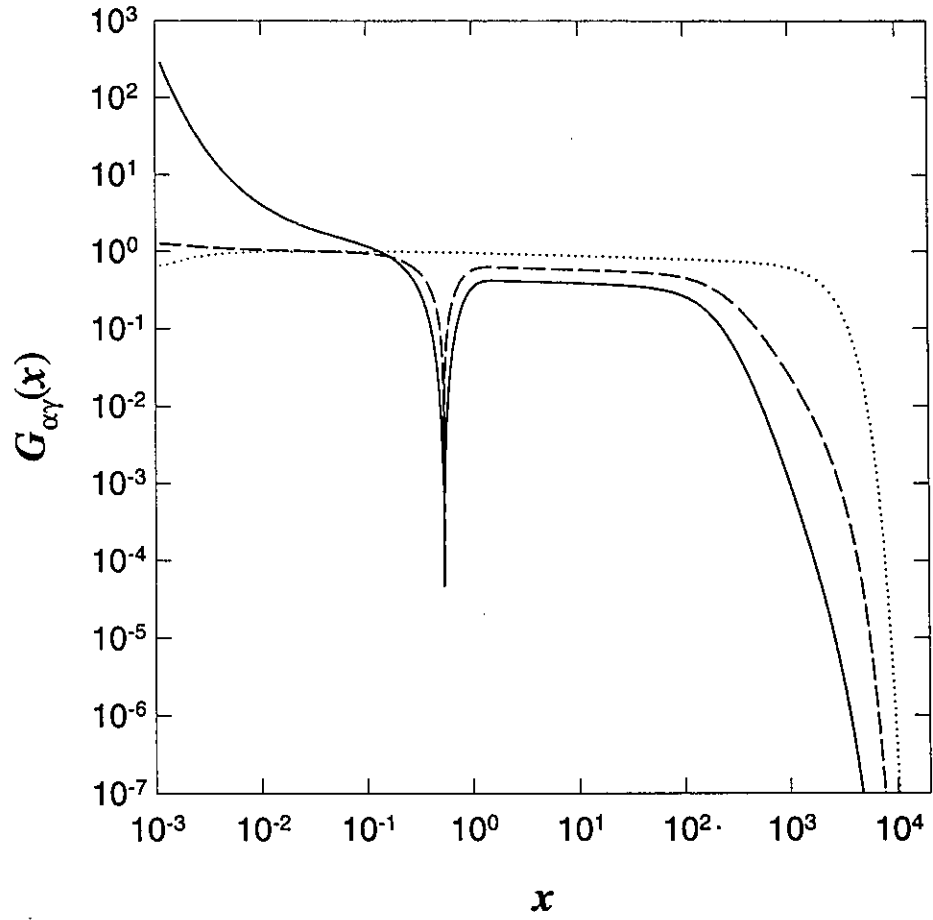


FIGURE 7a. The positive-ion spectrum (solid curve), the negative-ion spectrum (short-dashed curve), and the cospectrum (medium-dashed curve) that is negative for  $x > 0.534$ . Inputs are listed in Table 7.

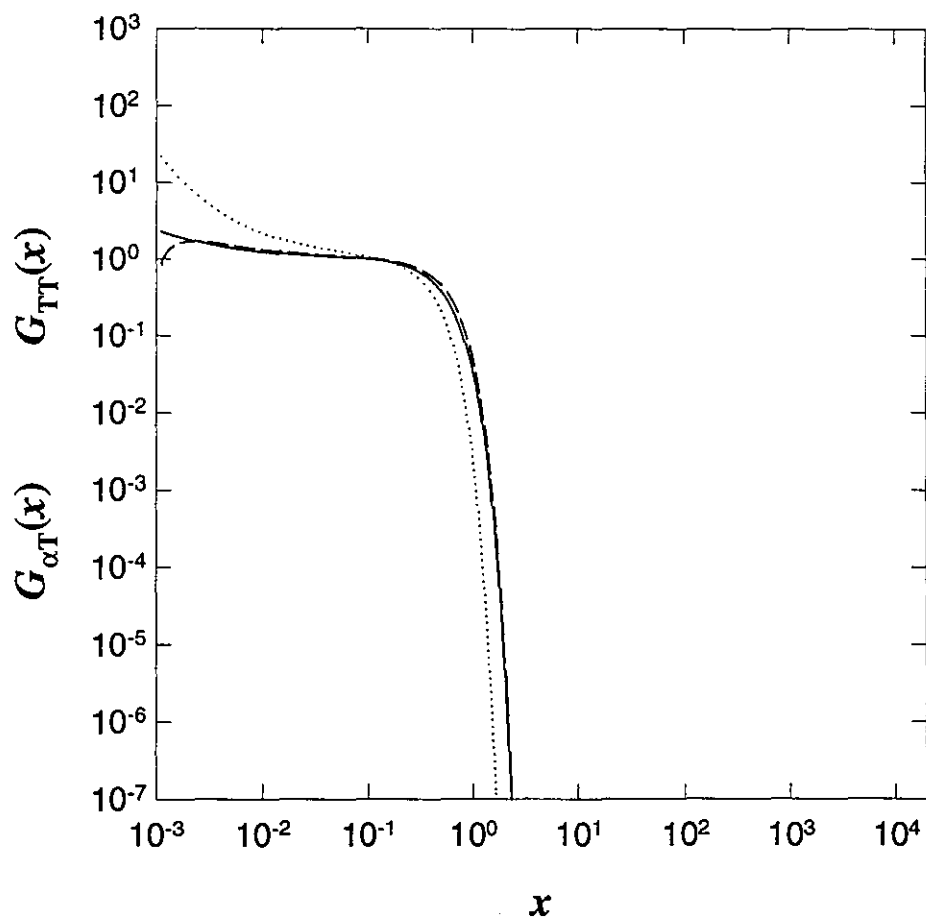


FIGURE 7b. Potential temperature-ion cospectra for the first (solid curve) and second (long-dashed curve) ions. The short-dashed curve is the potential temperature spectrum. Inputs are listed in Table 7.

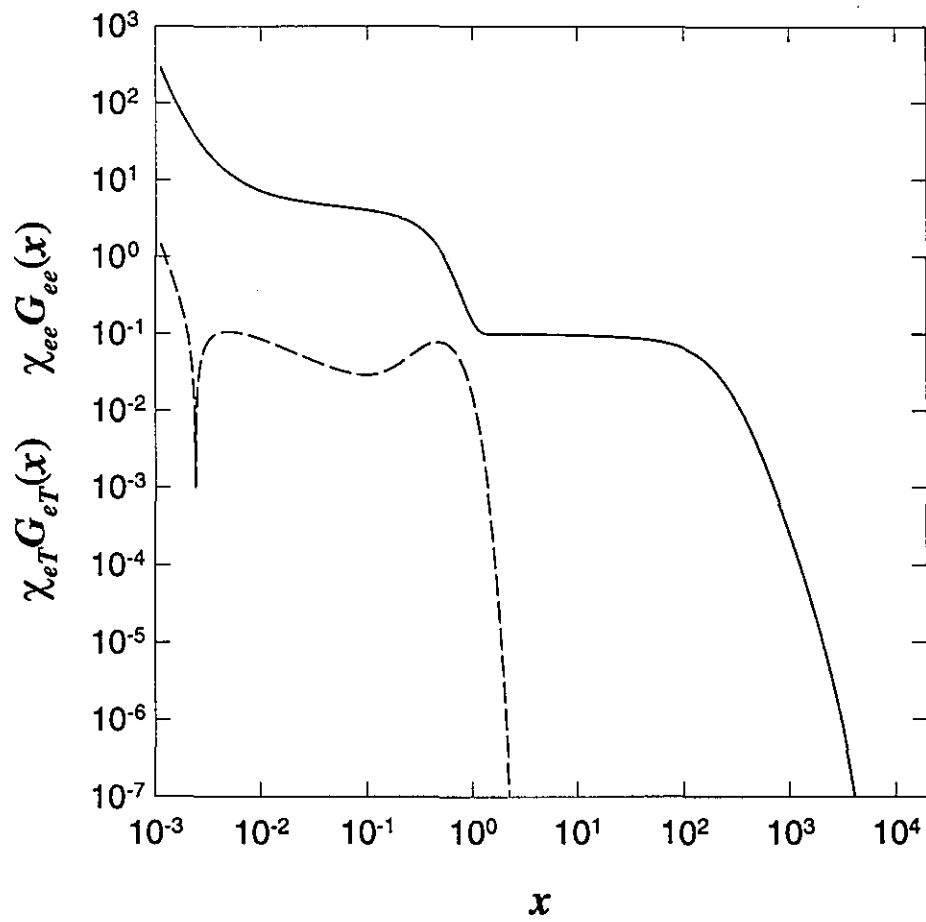


FIGURE 7c. The electron mixing-ratio spectrum (solid curve) and the cospectrum of potential temperature with electron mixing ratio (dashed curve) that is negative for  $x > 0.151$ . Inputs are listed in Table 7.

**TABLE 8.** Computer inputs for the calculation shown in Figs. 8a–c. See Table 1 for the meaning of the symbols.

---

```

# Each variable is preceded by a comment stating its name.
# n
2
# cd
1000
# eps
100
# nair
 $1.654 \times 10^{14}$ 
# temp
180.65
# Arrays. Arrays are listed as x(i) or y(j, i) or z(k, j, i), with the
# first subscript varying fastest, so after y(1, 1) comes y(2, 1)
# r (n)
    2.00000000000000
    1.00000000000000
# s (n)
    1.00000000000000
    -1.00000000000000
# wn (n)
2.
 $1 \times 10^6$ 
# chi (n, n)
2.7
1.
1.
100.
# chi t (n)
1.
1.
# chi t t
1.
# dt eps
0.
# dt chi (n, n)
0.
0.
0.
0.
# dt chi t (n)
0.
0.
# dt chi t t
0.
# omega (n)
0.
0.

```

---

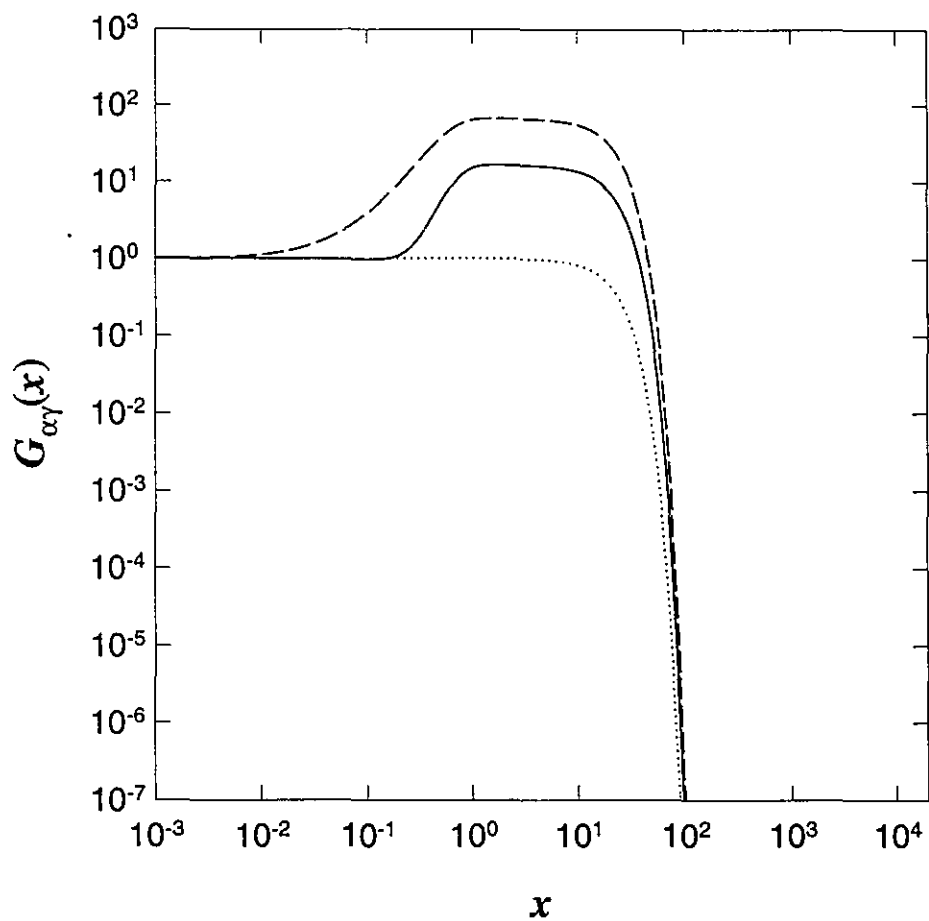


FIGURE 8a. The positive-ion spectrum (solid curve), the negative-ion spectrum (short-dashed curve), and the the cospectrum (medium-dashed curve) that is always positive. Inputs are listed in Table 8.

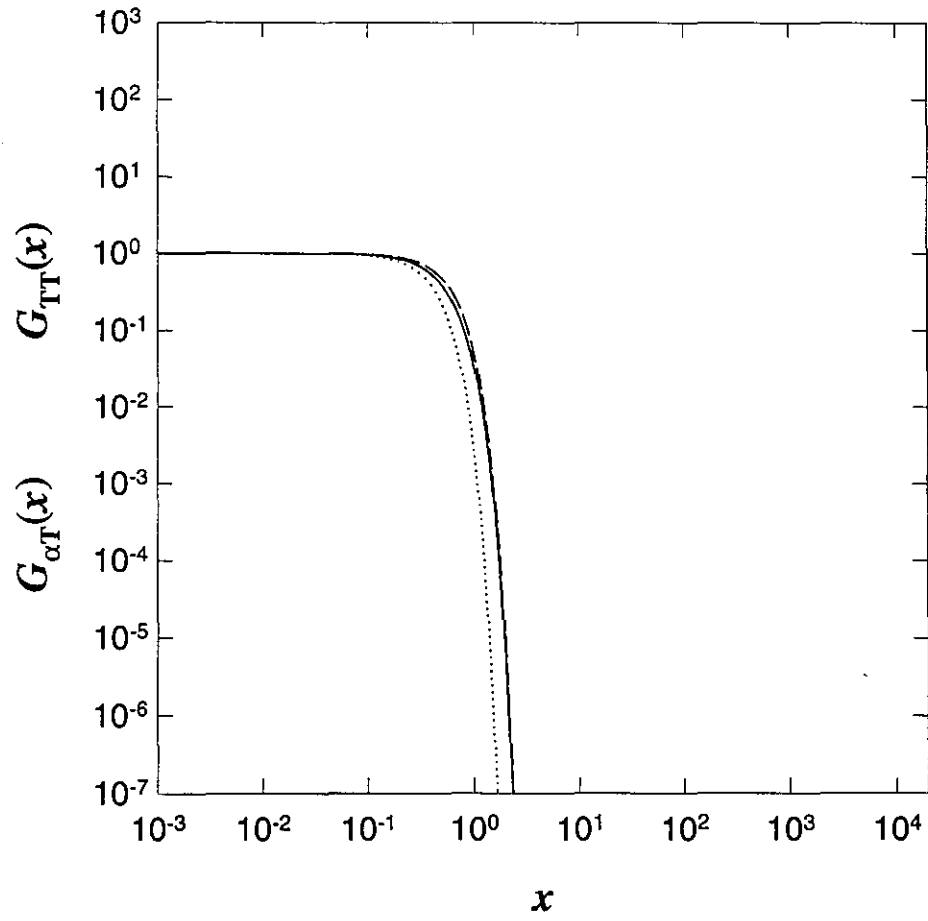


FIGURE 8b. Potential temperature-ion cospectra for the first (solid curve) and second (long-dashed curve) ions. The short-dashed curve is the potential temperature spectrum. Inputs are listed in Table 8.

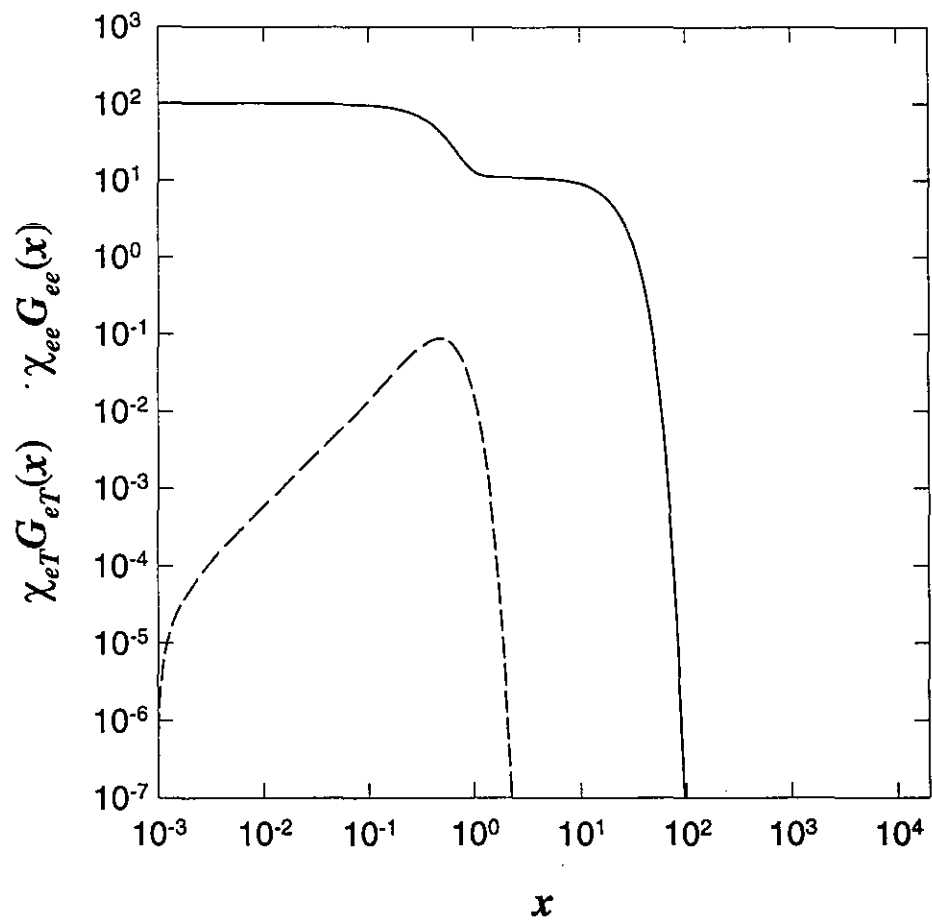


FIGURE 8c. The electron mixing-ratio spectrum (solid curve) and the cospectrum of potential temperature with electron mixing ratio (dashed curve). Inputs are listed in Table 8.

**TABLE 9.** Computer inputs for the calculation shown in Figs. 9a–c. See Table 1 for the meaning of the symbols.

---

```

# Each variable is preceded by a comment stating its name.
# n
2
# cd
1000
# eps
100
# nair
 $1.654 \times 10^{14}$ 
# temp
180.65
# Arrays. Arrays are listed as x(i) or y(j,i) or z(k,j,i), with the
# first subscript varying fastest, so after y(1,1) comes y(2,1)
# r(n)
2.00000000000000
1.00000000000000
# s(n)
1.00000000000000
-1.00000000000000
# wn(n)
2.
 $1 \times 10^6$ 
# chi(n,n)
2.7
1.
1.
100.
# chi t(n)
1.
1.
# chi t t
1.
# dt eps
 $-1 \times 10^{-1}$ 
# dt chi(n,n)
 $4.5 \times 10^{-3}$ 
 $5 \times 10^{-4}$ 
 $5.3 \times 10^{-4}$ 
 $3 \times 10^{-4}$ 
# dt chi t(n)
 $4 \times 10^{-4}$ 
 $1 \times 10^{-3}$ 
# dt chi t t
 $2.3 \times 10^{-3}$ 
# omega(n)
0.
0.

```

---



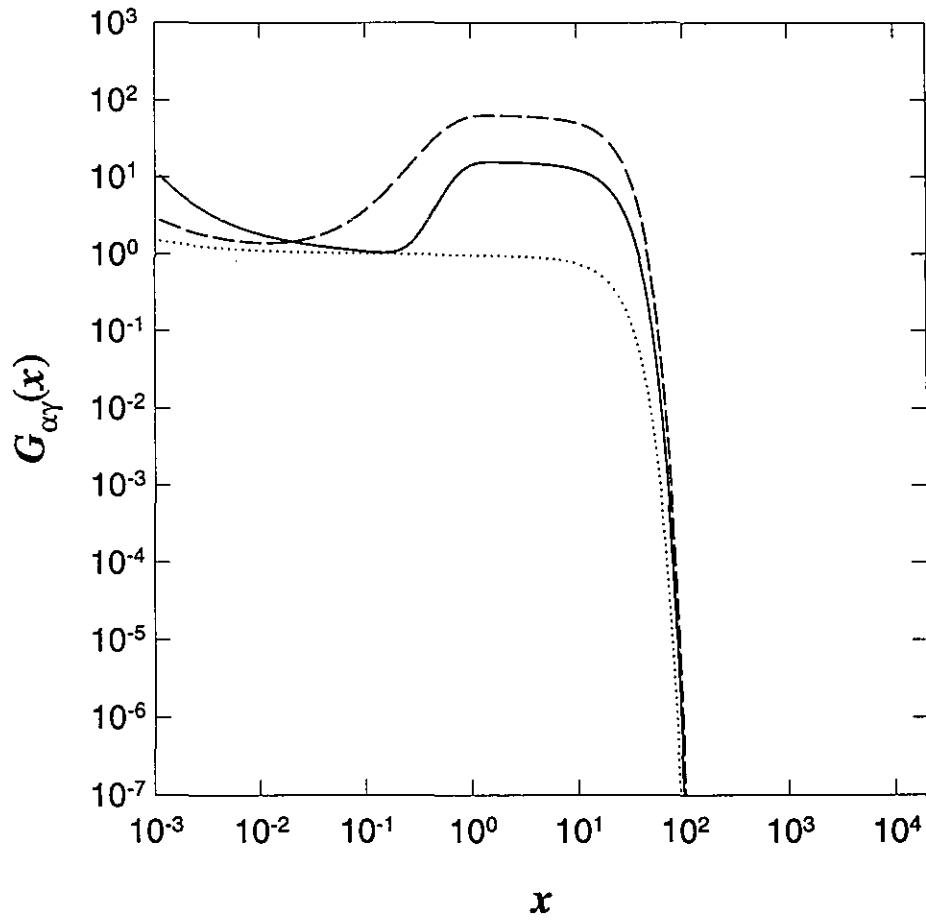


FIGURE 9a. The positive-ion spectrum (solid curve), the negative-ion spectrum (short-dashed curve), and the cospectrum (medium-dashed curve) that is always positive. Inputs are listed in Table 9.

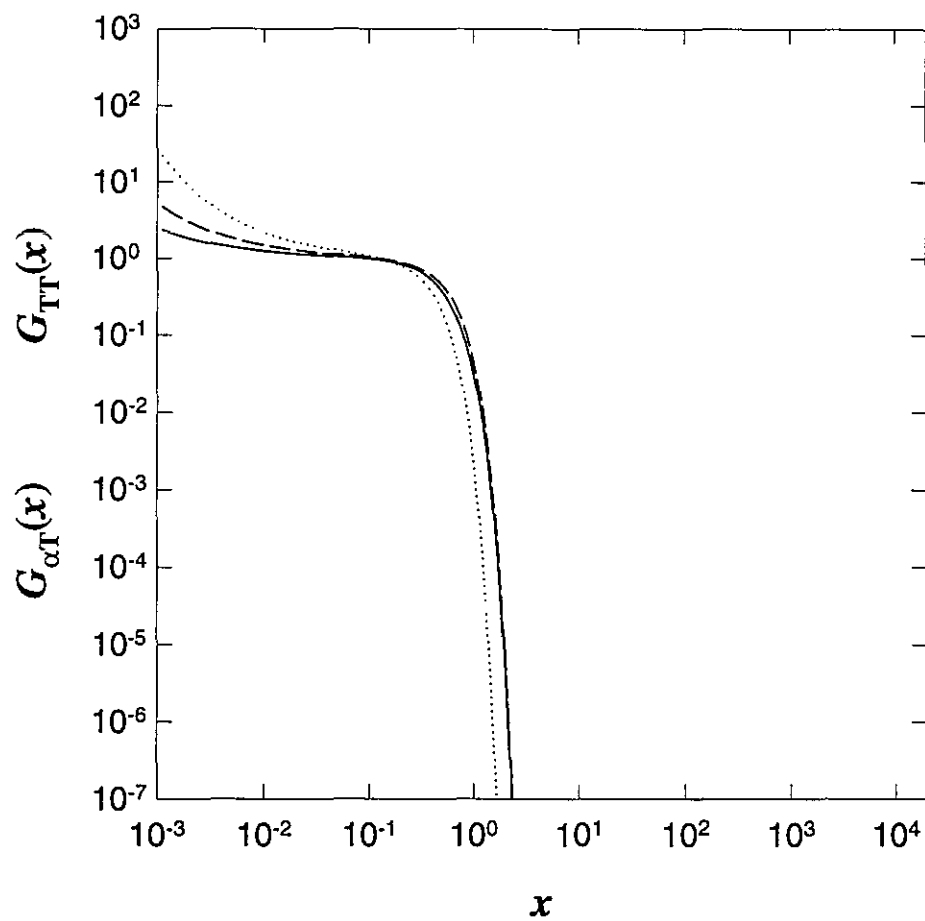


FIGURE 9b. Potential temperature-ion cospectra for the first (solid curve) and second (long-dashed curve) ions. The short-dashed curve is the potential temperature spectrum. Inputs are listed in Table 9.

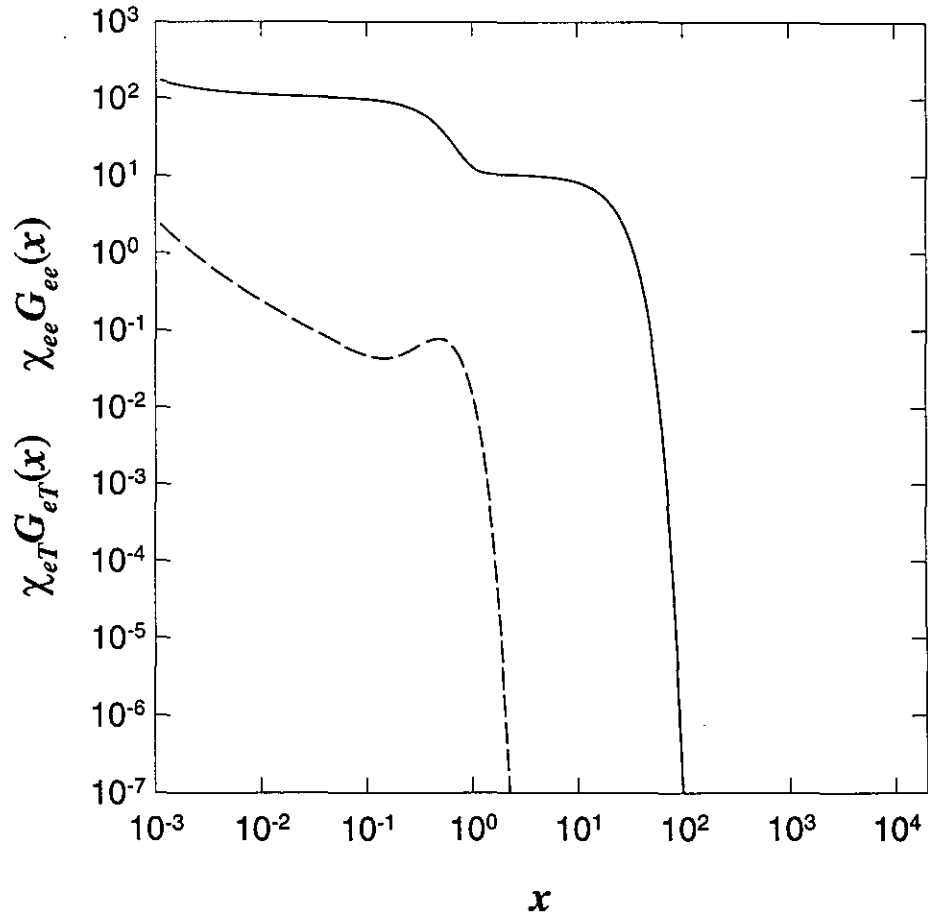


FIGURE 9c. The electron mixing-ratio spectrum (solid curve) and the cospectrum of potential temperature with electron mixing ratio (dashed curve) that is negative for  $x > 0.134$ . Inputs are listed in Table 9.

**TABLE 10.** Computer inputs for the calculation shown in Figs. 10a–c. See Table 1 for the meaning of the symbols.

---

```

# Each variable is preceded by a comment stating its name.
# n
2
# cd
1000
# eps
100
# nair
 $1.654 \times 10^{14}$ 
# temp
180.65
# Arrays. Arrays are listed as x(i) or y(j,i) or z(k,j,i), with the
# first subscript varying fastest, so after y(1,1) comes y(2,1)
# r (n)
    2.000000000000
    1.000000000000
# s (n)
    1.000000000000
    -1.000000000000
# wn (n)
2.
 $1 \times 10^6$ 
# chi (n, n)
2.7
1.
1.
100.
# chi t (n)
1.
1.
# chi t t
1.
# dt eps
0.
# dt chi (n, n)
0.
0.
0.
0.
# dt chi t (n)
0.
0.
# dt chi t t
0.
# omega (n)
 $1 \times 10^{-5}$ 
 $3 \times 10^{-3}$ 

```

---

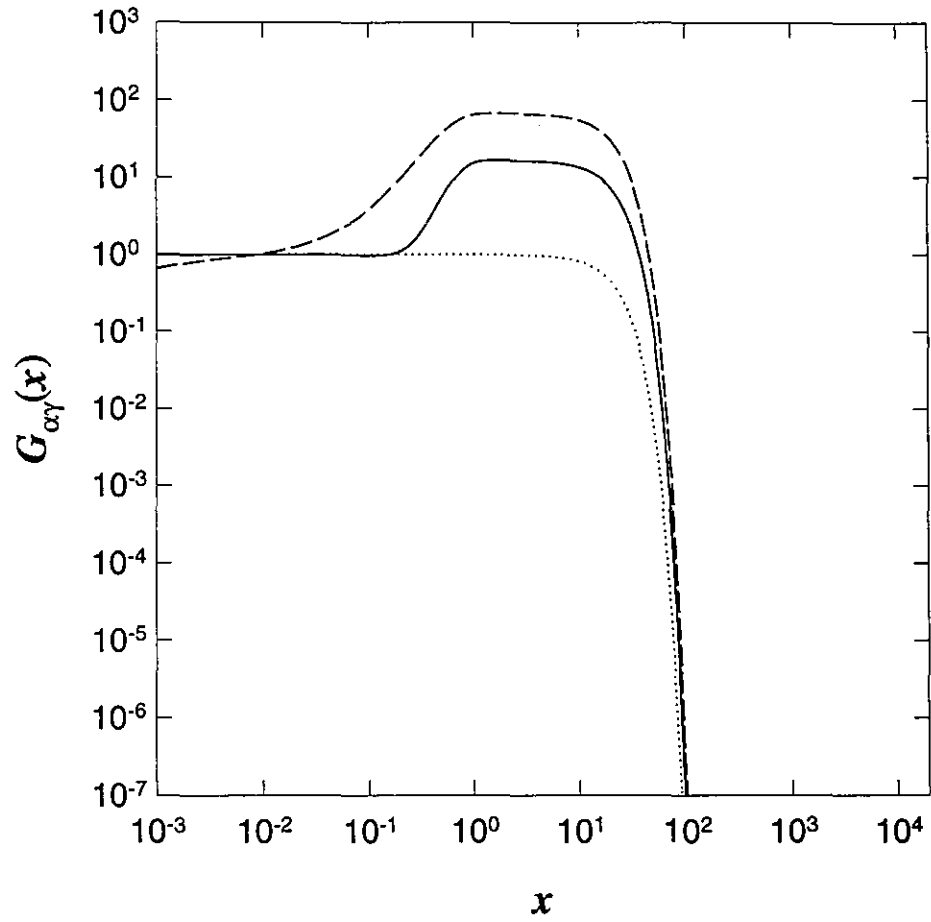


FIGURE 10a. The positive-ion spectrum (solid curve), the negative-ion spectrum (short-dashed curve), and the cospectrum (medium-dashed curve) that is always positive. Inputs are listed in Table 10.

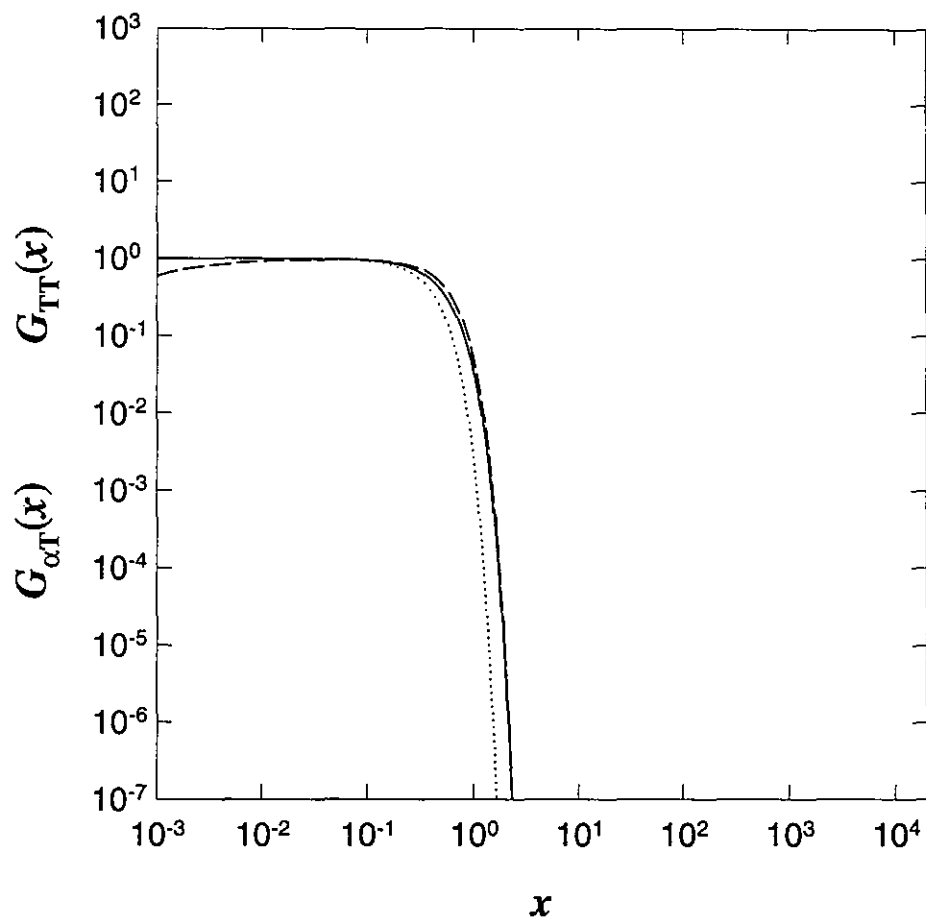


FIGURE 10b. Potential temperature-ion cospectra for the first (solid curve) and second (long-dashed curve) ions. The short-dashed curve is the potential temperature spectrum. Inputs are listed in Table 10.

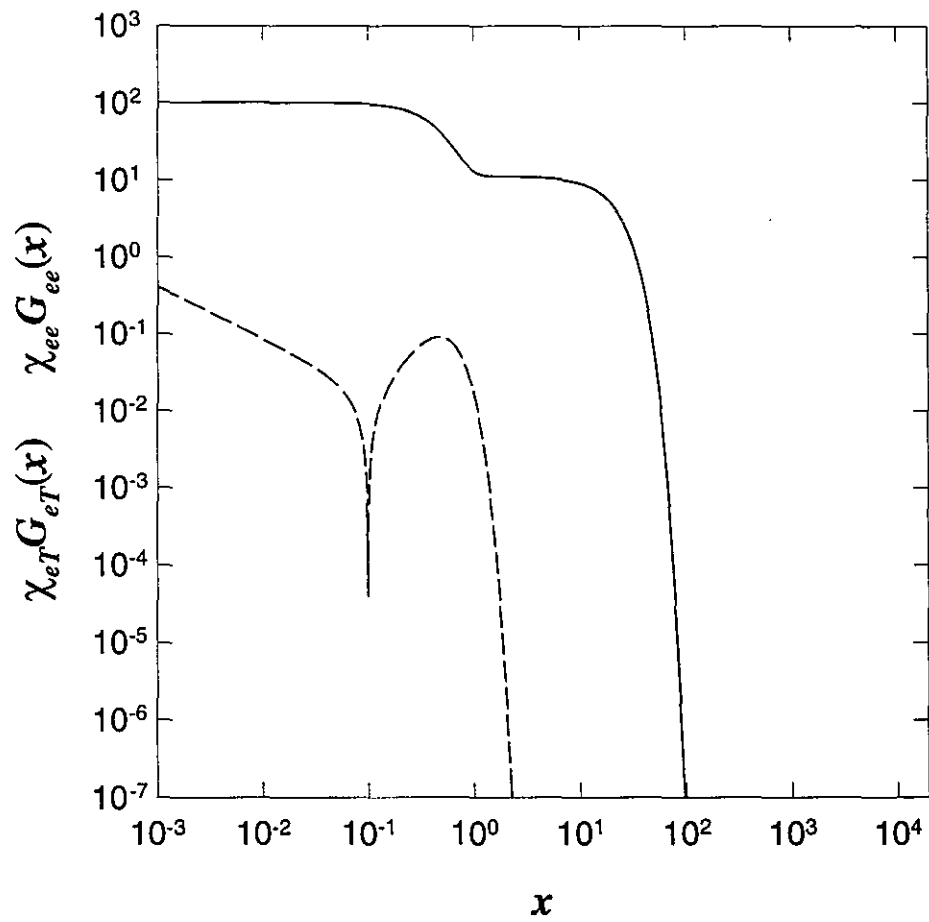


FIGURE 10c. The electron mixing-ratio spectrum (solid curve) and the cospectrum of potential temperature with electron mixing ratio (dashed curve) that is negative for  $x > 0.100$ . Inputs are listed in Table 10.

**TABLE 11.** Computer inputs for the calculation shown in Figs. 11a–c. See Table 1 for the meaning of the symbols.

---

```

# Each variable is preceded by a comment stating its name.
# n
2
# cd
1000
# eps
100
# nair
 $1.654 \times 10^{14}$ 
# temp
180.65
# Arrays. Arrays are listed as x(i) or y(j,i) or z(k,j,i), with the
# first subscript varying fastest, so after y(1,1) comes y(2,1)
# r (n)
2.00000000000000
1.00000000000000
# s (n)
1.00000000000000
-1.00000000000000
# wn (n)
2.
 $1 \times 10^6$ 
# chi (n, n)
2.7
1.
1.
100.
# chi t (n)
1.
1.
# chi t t
1.
# dt eps
 $-1 \times 10^{-1}$ 
# dt chi (n, n)
 $4.5 \times 10^{-3}$ 
 $5 \times 10^{-4}$ 
 $5.3 \times 10^{-4}$ 
 $3 \times 10^{-4}$ 
# dt chi t (n)
 $4 \times 10^{-4}$ 
 $1 \times 10^{-3}$ 
# dt chi t t
 $2.3 \times 10^{-3}$ 
# omega (n)
 $1 \times 10^{-5}$ 
 $3 \times 10^{-3}$ 

```

---



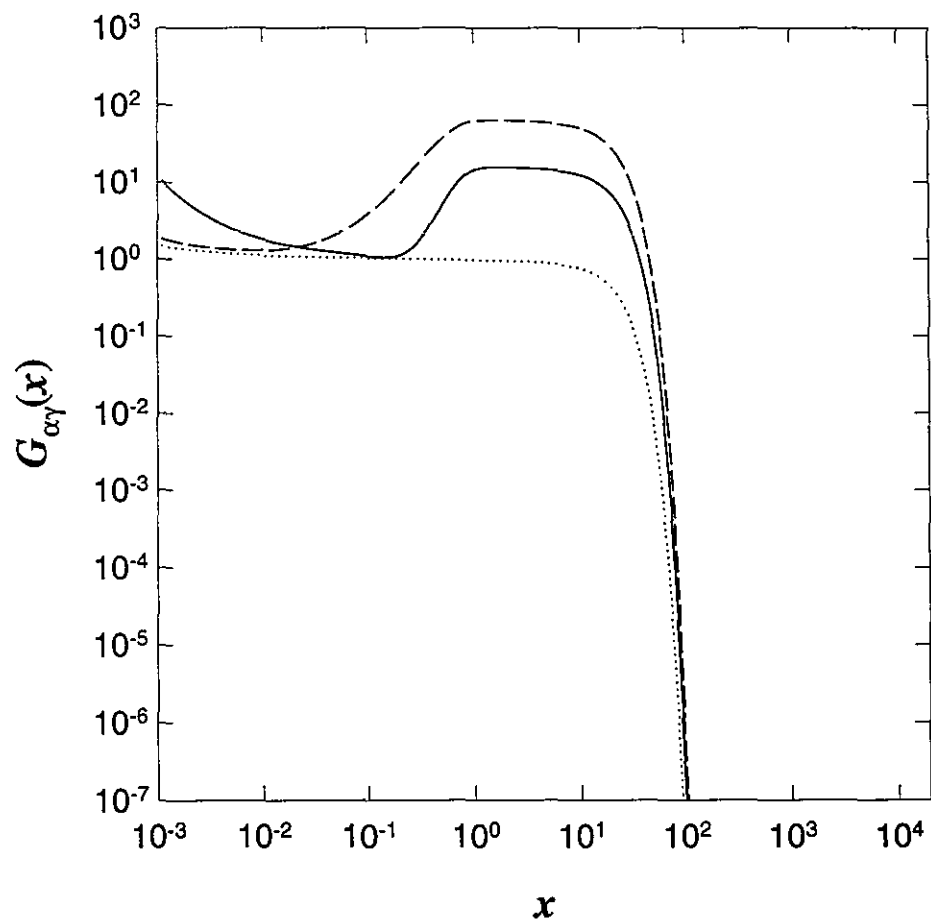


FIGURE 11a. The positive-ion spectrum (solid curve), the negative-ion spectrum (short-dashed curve), and the cospectrum (medium-dashed curve) that is always positive. Inputs are listed in Table 11.

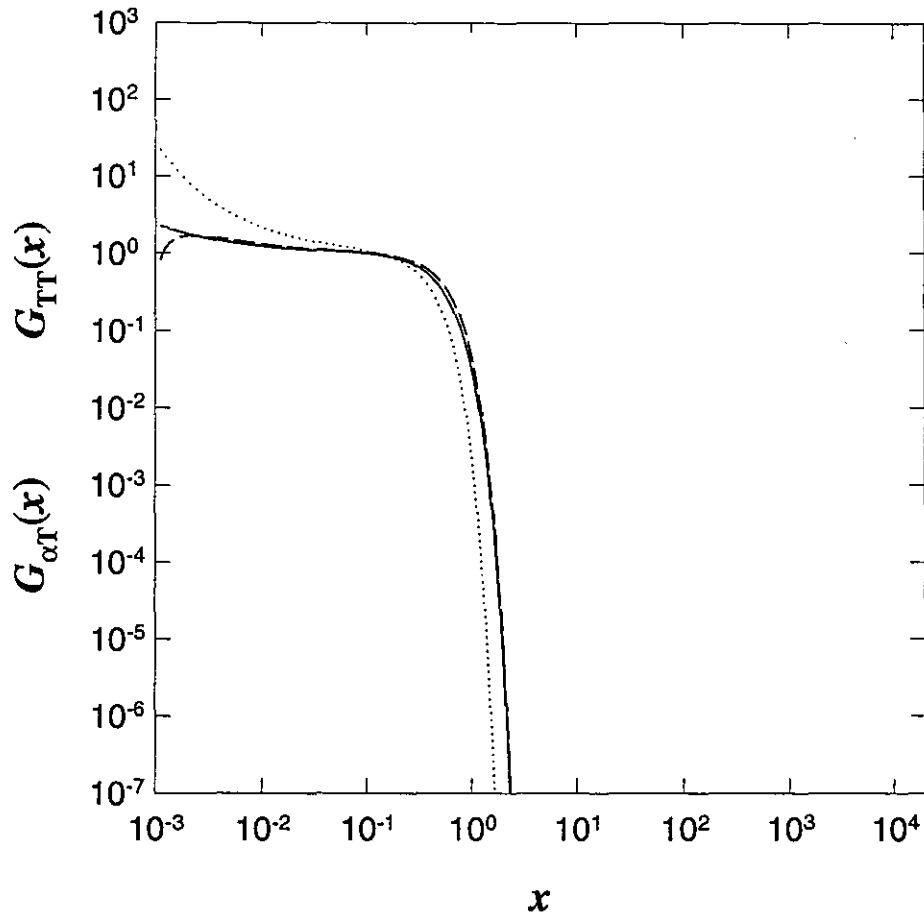


FIGURE 11b. Potential temperature-ion cospectra for the first (solid curve) and second (long-dashed curve) ions. The short-dashed curve is the potential temperature spectrum. Inputs are listed in Table 11.

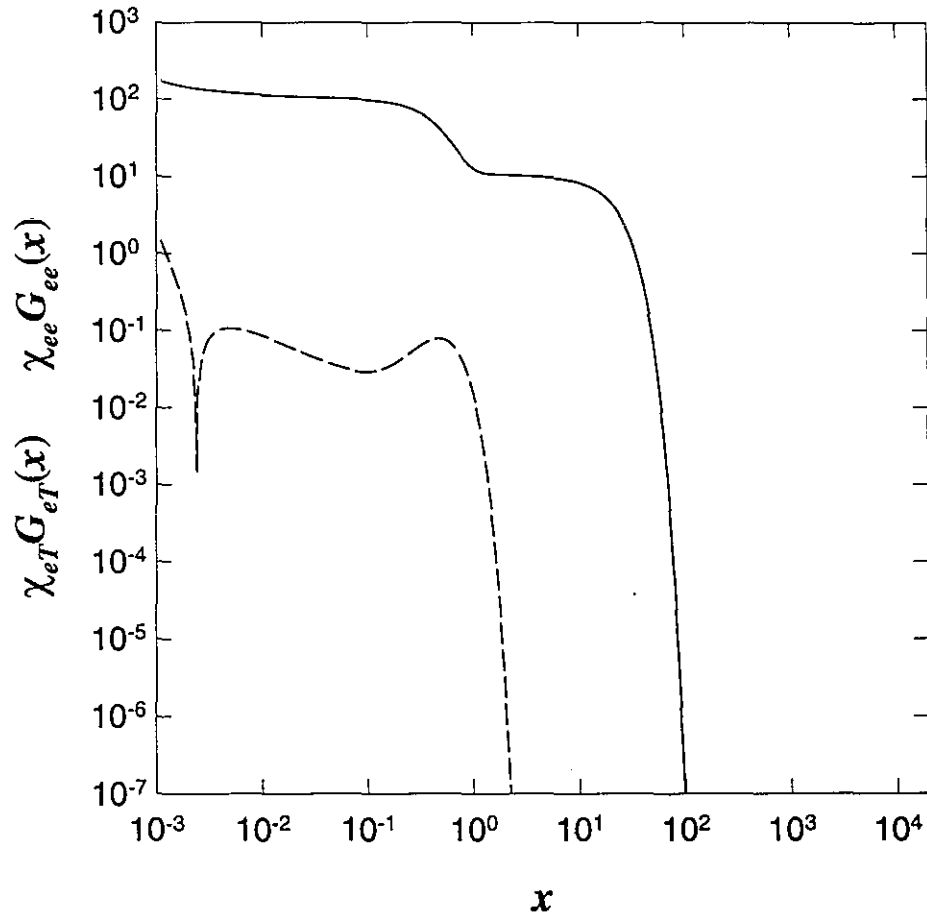


FIGURE 11c. The electron mixing-ratio spectrum (solid curve) and the cospectrum of potential temperature with electron mixing ratio (dashed curve) that is negative for  $x > 0.152$ . Inputs are listed in Table 11.

## 12. RELATIONSHIP TO RADAR CROSS SECTION AND SCATTERED POWER

Following Villars and Weisskopf (1955), the differential of power reflected into a solid angle  $d\Omega$  from a volume  $dV$  given incident power density  $\rho_0$  is

$$dP_r = \rho_0 \sigma dV d\Omega \sin^2 \chi ,$$

where  $\sigma$  is the scattering cross section per unit volume and per unit solid angle. To account for the angular scattering diagram, we have included the factor  $\sin^2 \chi$ , where  $\chi$  is the angle between the electric vector of the incident wave and the direction from the scattering volume to the receiver. The case  $R \gg d$  is considered, where  $R$  is range and  $d$  is any length dimension of the scattering volume. The solid angle subtended by the receiving antenna of area  $A$  is

$$\Delta\Omega = \frac{A}{R^2} .$$

If  $F$  is the cross-sectional area of the incident beam, then the transmitted power is

$$P_t = F \rho_0 .$$

Villars and Weisskopf (1955) considered the case of a scattering layer that is equidistant from identical transmitter and receiver antennas. For this case, the volume of a scattering height increment is

$$V_s = \frac{F \Delta z}{\sin(\theta/2)} ,$$

where  $\theta$  is the angle between incident and scattered wave vectors. Therefore, integrating  $dP_r$  over the volume  $V_s$  and solid angle range  $\Delta\Omega$  gives, for nearly uniform  $\rho_0$  and  $\sigma$ ,

$$P_r = \rho_0 \sigma \frac{F \Delta z}{\sin(\theta/2)} \frac{A}{R^2} \sin^2 \chi .$$

For backward scatter, we substitute  $\chi = \pi/2$  and  $\theta = \pi$ , and use  $P_t = \rho_0 F$  to obtain

$$P_r = P_t \sigma \Delta z \frac{A}{R^2} .$$

The scattering volume is determined by radar beamwidth and pulse length. However, the scattering volume can also be considered to be a smaller volume for which we choose to calculate the contribution to the total scattered power. If  $\Delta F$  is the increment of the cross-sectional area on the incident beam, then the incident power increment is  $\Delta P_i = \Delta F \rho_0$  and the scattering volume increment is  $\Delta V_s = \Delta F \Delta z$ , where  $\Delta z$  is some fraction of the height of the scattering volume. As before, the receiving antenna subtends the solid angle  $A/R^2$ . The increment of power to the receiver is then

$$\Delta P_r = \Delta P_i \sigma \Delta z \frac{A}{R^2} ,$$

where  $\sigma$  is the scattering cross section within the increment of the scattering volume.

Because the definition of the spectra in (53a,b), *et seq.*, are the same as in Hill and Bowhill (1976, p. 181), the relationship between  $\sigma$ , as defined by Villars and Weisskopf (1955), and the electron power spectrum  $\Gamma(k)$ , as given in (102), is the same as in equation (9.2) of Hill and Bowhill (1976); that is,

$$\sigma = r_e^2 2\pi^2 K^{-2} \Gamma(K) ,$$

where  $K$  is the Bragg wavenumber, and  $r_e$  is the classical electron radius, namely,

$$r_e = 2.8 \times 10^{-13} \text{ cm} .$$

For backscatter, the Bragg wavenumber is given in terms of the radar's frequency  $f$  in megahertz by

$$K = 2 \frac{2\pi}{c} f \times 10^6 ,$$

where  $c = 3 \times 10^8 \text{ m s}^{-1}$  is the speed of light.

Let us denote the above cross section as defined by Villars and Weisskopf (1955) and used by Hill and Bowhill (1976) as  $\sigma_{\text{VW}}$ , that defined by Ottersten (1969) as  $\sigma_{\text{OT}}$ , and that defined by Royrvick and Smith (1984) as  $\sigma_{\text{RS}}$ . It is useful to relate these definitions. As described by Ottersten (1969),  $\sigma_{\text{OT}}$  is the scattered power per unit solid angle, per unit volume, and per unit incident power density. Ottersten (1969) also defined another cross section per unit volume  $\eta$ , which is just  $\sigma$  integrated over all solid angles, such that  $\eta_{\text{OT}} = 4\pi \sigma_{\text{OT}}$  for isotropic scattering. Using well-known spectral definitions such as those given by Ottersten (1969), one obtains  $\sigma_{\text{VW}} = \sigma_{\text{OT}} = \sigma_{\text{RS}}/4\pi$ ; therefore,  $\sigma_{\text{RS}} = \eta_{\text{OT}}$ . In relating these cross sections, it is useful to note that the refractive index  $n$  of a plasma is given by  $n^2 = 1 - (\omega_p/\omega)^2$ , where  $\omega_p^2 = 4\pi N_e e^2/m_e$  is the plasma frequency and  $\omega$  is the radar frequency in  $\text{rad s}^{-1}$ . We are concerned with the case for which  $\omega \gg \omega_p$  such that  $\omega = kc$ , where  $k$  is the radar's wavenumber in  $\text{rad m}^{-1}$ . For  $\omega \gg \omega_p$ , the fluctuations of refractive index  $n'$  are approximated by the Taylor series expansion of  $n = [1 - (\omega_p/\omega)^2]^{1/2}$  in terms of electron-concentration fluctuations  $N_e'$ ; this gives

$$n' \approx -\frac{1}{2} (\omega_p/\omega)^2 \frac{N_e'}{N_e} .$$

Now  $\Gamma(K)$  is an average spectrum over a given volume; hence,  $\sigma$  must be taken as uniform over the given volume. It follows that the power ratio in decibels is given by

$$10 \log_{10} (P_r/P_i) = 10 \log_{10} \left[ (r_e/R)^2 2\pi^2 A \Delta z K^{-2} \Gamma(K) \right] . \quad (164)$$

Given pulse length  $\Delta z$ , antenna area  $A$ , range  $R$ , radar frequency  $f$ , and the calculated electron spectrum  $\Gamma(K)$  from (102), we can evaluate the power ratio, whereas only  $f$  and  $\Gamma(K)$  are needed to evaluate the cross section  $\sigma$ . The radar equation (164) is the same as was given by Villars and Weisskopf (1955). The reader is cautioned that the radar equation applied to specific radars can differ from (164). For instance, a factor accounting for antenna efficiency might be included, or signal-to-noise ratio might be given instead of  $P_r/P_t$ . Thus, (164) is for purposes of illustration only.

### 13. DISCUSSION

Equations describing diffusion modes of a multiconstituent collision-dominated plasma with negligible magnetic-field effects have been used to obtain continuity equations for the mixing ratios of the charged species. A perturbation analysis is used to linearize those equations. The linearized continuity equations are used to derive equations for spectra and cospectra of the ionic constituents in terms of which the spectrum of electron-concentration fluctuations is expressed on the basis of approximate charge neutrality. Charge neutrality is approximate in the sense that the effects of a nonzero Debye length are included. Solutions for spectra and cospectra are obtained and explained in section 11. It is seen that massive ions can cause electron fluctuations at small scales. If the ions are sufficiently massive, the Debye shielding effect can determine the smallest scales on which there are electron-concentration fluctuations. For more than one species of ion, the turbulent advection is in no sense characterized by a single Schmidt number.

### 14. ACKNOWLEDGMENTS

Funding was provided by National Science Foundation grant ATM-9618004. The numerical simulation of the Kelvin-Helmholtz instability and its analysis was performed at the Colorado Research Associates by Joseph Werne, David Fritts, and Dorothy Gibson-Wilde.

### 15. REFERENCES

- Azoulay, A., V. Thiermann, A. Jetter, A. Kohnle, and Z. Azar, 1988. Optical measurements of the inner scale of turbulence. *J. Phys. D.* **21**:541–544.
- Batchelor, G. K., 1959. Small-scale variation of convected quantities like temperature in turbulent fluid. Part 1: General discussion and the case of small conductivity. *J. Fluid Mech.* **5**:113–133.
- Batchelor, G. K., 1970. *An Introduction to Fluid Dynamics*. Cambridge University Press, Cambridge, England, 615 pp.
- Bogucki, D., J. A. Domaradzki, and P. K. Yeung, 1997. Direct numerical simulations of passive scalars with  $Pr > 1$  advected by turbulent flow. *J. Fluid Mech.* **343**:111–130.
- Chasnov, J. R., 1998. The viscous-convective subrange in nonstationary turbulence. *Phys. Fluids* **10**(5):1191–1204.

- Cho, J. Y. N., 1993. Radar scattering from the summer polar mesosphere: Theory and observations. Ph.D. thesis. Cornell University, Ithaca, New York, 204 pp.
- Cho, J. Y. N., T. M. Hall, and M. C. Kelley, 1992. On the role of charged aerosols in polar mesosphere summer echoes. *J. Geophys. Res.* **97**:875–886.
- Cho, J. Y. N., C. M. Alcala, M. C. Kelly, and W. E. Swartz, 1996. Further effects of charged aerosols on summer mesospheric radar scatter. *J. Atmos. Terr. Phys.* **58**:661–672.
- Consortini, A., F. Cochetti, J. H. Churnside, and R. J. Hill, 1993. Inner-scale effect on irradiance variance measured for weak-to-strong atmospheric scintillation. *J. Opt. Soc. Am. A* **10**:2354–2362.
- Flatté, S. M., G. Wang, and J. Martin, 1993. Irradiance variance of optical waves through atmospheric turbulence by numerical simulation and comparison with experiment. *J. Opt. Soc. Am. A* **10**:2363–2370.
- Frehlich, R. G., 1992. Laser scintillation measurements of the temperature spectrum in the atmospheric surface layer. *J. Atmos. Sci.* **49**:1494–1509.
- Hill, R. J., 1978a. Nonneutral and quasi-neutral diffusion of weakly ionized multiconstituent plasma. *J. Geophys. Res.* **83**(A3):989–998.
- Hill, R. J., 1978b. Models of the scalar spectrum for turbulent advection. *J. Fluid Mech.* **88**(3):541–562.
- Hill, R. J., 1978c. Spectra of fluctuations in refractivity, temperature, humidity, and the temperature-humidity cospectrum in the inertial and dissipation ranges. *Radio Sci.* **13**(6):953–961.
- Hill, R. J., 1979. Magnetic field effects on ionization inhomogeneities advected by motions of the neutral gas. *J. Geophys. Res.* **84**(A10):5850–5862.
- Hill, R. J., 1981. Dissipation of D-region ionization inhomogeneities by diffusion and photochemical relaxation. Abstracts of Scientific Papers, Scientific Sessions of the URSI Commissions, XX<sup>th</sup> General Assembly of the Int. Union of Radio Science, August 10–19, 1981, Washington, DC, p. 86.
- Hill, R. J., 1989. Structure functions and spectra of scalar quantities in the inertial-convective and viscous-convective ranges of turbulence. *J. Atmos. Sci.* **46**(14):2245–2251.
- Hill, R. J., and S. A. Bowhill, 1976. Small-scale fluctuations in D-region ionization due to hydrodynamic turbulence. Aeronomy Report no. 75. Aeronomy Laboratory, Dept. of Electrical Engineering, University of Illinois, Urbana, IL, 371 pp.
- Hill, R. J., and S. A. Bowhill, 1977a. Transient compressional response of D-region ionization. *J. Atmos. Terr. Phys.* **39**:333–345.
- Hill, R. J., and S. A. Bowhill, 1977b. Collision frequencies for use in the continuum momentum equations applied to the lower ionosphere. *J. Atmos. Terr. Phys.* **39**:803–811.
- Hill, R. J., and G. R. Ochs, 1978. Fine calibration of large-aperture scintillometers and an optical estimate of inner scale of turbulence. *Appl. Opt.* **17**:3608–3612.
- Hill, R. J., and G. R. Ochs, 1992. Inner-scale dependence of scintillation variances. *J. Opt. Soc. Am. A* **9**:1406–1411.
- Hill, R. J., and S. T. Thoroddsen, 1997. Experimental evaluation of acceleration correlations for locally isotropic turbulence. *Phys. Rev. E* **55**(2):1600–1606.
- Holt, E. H., and R. E. Haskell, 1965. *Plasma Dynamics*. Macmillan, New York, 510 pp.

- Kelley, M. C., and J. C. Ulwick, 1988. Large- and small-scale organization of electrons in the high-latitude mesosphere: Implications of the STATE data. *J. Geophys. Res.* **93**:7001–7008.
- Kelley, M. C., D. T. Farley, and J. Rottger, 1987. The effect of cluster ions on anomalous VHF backscatter from the summer polar mesosphere. *J. Geophys. Res.* **14**:1031–1034.
- Kraichnmn, R. H., 1968. Small-scale structure of a scalar field convected by turbulence. *Phys. Fluids*, **11**:945-953.
- Langevin, M. P., 1905. Une formule fondamentale de théorie cinétique. *Annales de Chimie et de Physique*, series 8, **5**:245–288.
- McDaniel, E. W., 1964. *Collision Phenomena in Ionized Gases*. Wiley Series in Plasma Physics, John Wiley & Sons, Inc., New York, 775 pp.
- Obukhov, A. M., 1949. Structure of the temperature field in turbulent flow. *Izv. Akad. Nauk. SSSR, Ser. Geogr. i Geofiz.* **13**:58–69.
- Ochs, G. R., and R. J. Hill, 1985. Optical-scintillation method of measuring turbulence inner scale. *J. Opt.* **24**:2430–2432.
- Ottersten, H., 1969. Radar backscattering from the turbulent clear atmosphere. *Radio Sci.* **4**(12):1251–1255.
- Rastogi, P. K., and S. A. Bowhill, 1976. Scattering of radio waves from the mesosphere. 2. Evidence for intermittent mesospheric turbulence. *J. Atmos. Terr. Phys.* **38**:449–462.
- Rastogi, P. K., and R. F. Woodman, 1974. Mesospheric studies using the Jicamarca incoherent-scatter radar. *J. Atmos. Terr. Phys.* **36**:1217–1231.
- Royrvik, O., and L. G. Smith, 1984. Comparison of mesospheric VHF radar echoes and rocket probe electron concentration measurements. *J. Geophys. Res.* **89**:9014–9022.
- Sreenivasan, K. R., 1998. An update on the energy dissipation rate in isotropic turbulence. *Phys. Fluids* **10**:528–529.
- Thiermann, V., and H. Grassl, 1992. The measurement of turbulent surface-layer fluxes by use of bichromatic scintillation. *Bound.-Layer Meteor.* **58**:367–389.
- Villars, F., and V. F. Weisskopf, 1955. On the scattering of radio waves by turbulent fluctuations of the atmosphere. *Proc. IRE* **43**:1232–1238.



## APPENDIX: COLLISION RATE FOR SPECIES $\alpha$

Transport coefficients  $\mu_\alpha$ ,  $D_\alpha$ , and  $\mathcal{D}_\alpha$  appear in many equations in this report. These transport coefficients are defined in terms of the momentum-transfer collision rate for species  $\alpha$ , which is denoted by  $v_\alpha$ . Here, we describe the calculation of  $v_\alpha$ . We adopt the collision model of the polarization interaction with an elastic sphere repulsion. This model is analyzed in a classic paper by Langevin (1905), who reduced the calculation to a single graph supplemented with analytic formulas. A translation of Langevin's (1905) paper is given by McDaniel (1964), but the graph in the translation has slight inaccuracies. A discussion of ion collision processes for the lower ionosphere and applicability of the polarization interaction is given by Hill and Bowhill (1977b).

Air molecules are by far the most numerous collision partners; thus, ion-ion and ion-electron collisions need not be considered. The total collision rate is the sum of contributions of the three most numerous constituents of air, namely, nitrogen ( $N_2$ ), oxygen ( $O_2$ ), and argon (Ar).

The parameters of these constituents of air that are required for the calculation of  $v_\alpha$  are given in Table A1. These parameters are abundance ( $A$ ), polarizability ( $\kappa$ ), mass ( $m$ ), and radius ( $r$ ). We calculate the collision rate for a given ion with each of the three constituents of air and sum these collision rates in proportion to the abundance ( $A$ ) of the constituents (see Table A1) to obtain  $v_\alpha$ .

**TABLE A1.** Properties of  $N_2$ ,  $O_2$ , and Ar.

	Abundance <sup>§</sup> ( $A$ )	Polarizability <sup>†</sup> ( $\kappa$ )	Mass <sup>‡</sup> ( $m$ )	Radius <sup>§§</sup> ( $r$ )
$N_2$	0.78	1.74	$28 m_n$	1.5
$O_2$	0.21	1.57	$32 m_n$	1.5
Ar	0.01	1.64	$40 m_n$	0.75

<sup>§</sup>Abundance ( $A$ ) is given as a fraction of  $N$ .

<sup>†</sup>Polarizability ( $\kappa$ ) is in units of  $10^{-24} \text{ cm}^3$ .

<sup>‡</sup>Mass ( $m$ ) is given in units of the nucleon mass,  $m_n = 1.67 \times 10^{-24} \text{ gr}$ .

<sup>§§</sup>Radius ( $r$ ) is given in units of  $10^{-8} \text{ cm}$  (i.e., the Angstrom).

The ion is assumed to be a hydrated proton having  $n_w$  water molecules ( $H_2O$ ). The mass of this ion is therefore  $m_\alpha = (18 n_w + 1) m_n$ , where  $m_n = 1.67 \times 10^{-24} \text{ gr}$  is the nucleon mass. The radius of this ion is taken to be  $r_\alpha = 10^{-8} \text{ cm}$  if  $n_w = 1$  and, for  $n_w > 1$ , it is  $r_\alpha = (1.93 \times 10^{-8} \text{ cm}) n_w^{1/3}$ , the latter being the radius of an ice sphere of mass density  $1 \text{ gr cm}^{-3}$ . Any other type of ion requires changing only the relationship between mass  $m_\alpha$  and radius  $r_\alpha$ ; this relationship, above, is parametric with the parameter  $n_w$ .

If the ion is very large, it becomes likely that it will simultaneously collide with more than one neutral air molecule, whereas Langevin's model is for single-molecule collisions. The interaction distance of an air molecule with a very large ion is probably not greater than 20 angstroms ( $1 \text{ \AA} = 10^{-8} \text{ cm}$ ). Hence, we need the likelihood that two air molecules are within a shell that is 20  $\text{\AA}$  thick and that has the radius of the ion. This shell has a volume of  $(4\pi/3) [(r_a + 2 \times 10^{-7} \text{ cm})^3 - r_a^3] \approx 2.5 \times 10^{-6} \text{ cm} r_a^2$ . The volume per air molecule is  $N^{-1}$ . If the volume of the interaction shell exceeds  $N^{-1}$ , then multiple simultaneous collisions become likely. This condition is  $2.5 \times 10^{-6} \text{ cm} r_a^2 > N^{-1}$ . For  $N = 2 \times 10^{14} \text{ cm}^{-3}$ , the condition is  $r_a > 45 \text{ \mu m}$ . Ions that have radii less than  $0.45 \text{ \mu m}$  are considered. Therefore, the single-molecule collision model is applicable.

The approximation of colliding elastic spheres requires the introduction of the necessarily approximate radii  $r$  and  $r_a$ . Certainly,  $\text{O}_2$ ,  $\text{N}_2$ , and a hydrated proton are not spherical. Moreover, a collision with a multiply hydrated proton need not be elastic. A multiply hydrated proton can have many closely spaced energy levels or have energy bands that can absorb or add kinetic energy during an impact. Nevertheless, the polarization interaction with an elastic-sphere repulsion is the most reasonable collision model that can be attained without undue labor.

Langevin's (1905) graph gives a parameter that he called  $(3/16 Y)$  as a function of  $\mu^{-1}$ , the latter being defined as

$$\mu^{-1} \equiv (r + r_a)^2 (2T/q_a^2 \kappa)^{1/2} ,$$

where  $\kappa$  is polarizability as given in Table A1, and recall that  $T$  is air temperature in energy units. Langevin's graph is reproduced in Fig. A1; he obtained the graph by integration using graphical methods. Now  $\mu^{-2}$  is proportional to the ratio of kinetic energy to the potential energy of the polarization interaction when the two spheres touch. Thus, for large  $\mu^{-1}$  the collision is essentially an elastic-sphere collision with negligible effect of the polarization interaction, in which case  $(3/16 Y) \approx 3/(4 \mu^{-1})$ . For small  $\mu^{-1}$ , the collision is essentially the polarization interaction with negligible elastic repulsion, in which case  $(3/16 Y) \approx 0.505$ . As seen in Fig. A1, at  $\mu^{-1} \approx 0.41$  the parameter  $(3/16 Y)$  has a local maximum of about 0.585. This maximum corresponds to increased mobility of the ion because the attractive polarization interaction is partially compensated by the elastic-sphere repulsion. We have digitized Langevin's graph of  $(3/16 Y)$  versus  $\mu^{-1}$  for  $0 \leq \mu^{-1} \leq 4.03$ . We use interpolation to obtain  $(3/16 Y)$  for a given  $\mu^{-1}$ . For  $\mu^{-1} > 4$ , the elastic-sphere asymptotic formula is used; in comparison with Langevin's graph, it is accurate to better than 0.1% at  $\mu^{-1} \geq 4$ .

The algorithm for the contribution of any one of the air constituents in Table A1 to the collision frequency  $\nu_a$  is

$$\frac{8 AN}{3} (r + r_a)^2 M (2\pi T)^{1/2} \quad \text{for } \mu^{-1} > 4 \quad (\text{A1a})$$

$$\frac{2 AN}{(3/16 Y)} M (\pi \kappa q_a^2)^{1/2} \quad \text{for } \mu^{-1} \leq 4 , \quad (\text{A1b})$$

where

$$M \equiv \left( \frac{m m_\alpha}{m + m_\alpha} \right)^{1/2} m_\alpha^{-1}.$$

Of course,  $AN$  is the number of molecules per unit volume of the constituent of air. Recall that  $A$ ,  $\kappa$ ,  $m$ , and  $r$  are given in Table A1;  $N$ ,  $T$ ,  $m_\alpha$ , and  $q_\alpha$  are described in the notation list; and  $(3/16 Y)$ ,  $\mu^{-1}$ , and  $r_\alpha$  are described in this Appendix. Note that  $\mu^{-1}$  is a different value for each of the three constituents in Table A1. The sum of the three contributions from (A1a,b) gives  $v_\alpha$  in units of  $s^{-1}$ .

In Fig. A2, we show  $D_\alpha = T/m_\alpha v_\alpha$  as a function of  $n_w$ . Of course, use of  $n_w$  as the abscissa is similar to use of  $m_\alpha$  or  $r_\alpha^3$  for the abscissa. Cases for two temperatures and single-charged ( $S_\alpha = 1$ ) and quintuple-charged ( $S_\alpha = 5$ ) ions are shown in Fig. A2. The asymptote for very large  $n_w$  (hence, very large  $m_\alpha$  and  $r_\alpha^3$ ) is  $v_\alpha \propto n_w^{-2/3}$ . A line of slope  $-2/3$  is shown in Fig. A2 to indicate this asymptote. The decrease in the lowest curve in Fig. A2 for  $n_w \lesssim 10$  is caused mainly by the variation of  $1/(m_\alpha M)$ . The maximum of  $(3/16 Y)$  at  $\mu^{-1} \approx 0.41$  corresponds approximately to  $n_w$  between 1 and 2 for  $S_\alpha = 1$  and  $n_w \approx 31$  for  $S_\alpha = 5$ . Values of  $v_\alpha$  (and, hence,  $D_\alpha$ ) calculated solely from the polarization interaction and solely from the elastic-sphere repulsion are equal at  $\mu^{-1} = 1.485$ , which corresponds to  $n_w = 17$  for  $S_\alpha = 1$  and to  $n_w = 300$  for  $S_\alpha = 5$ .

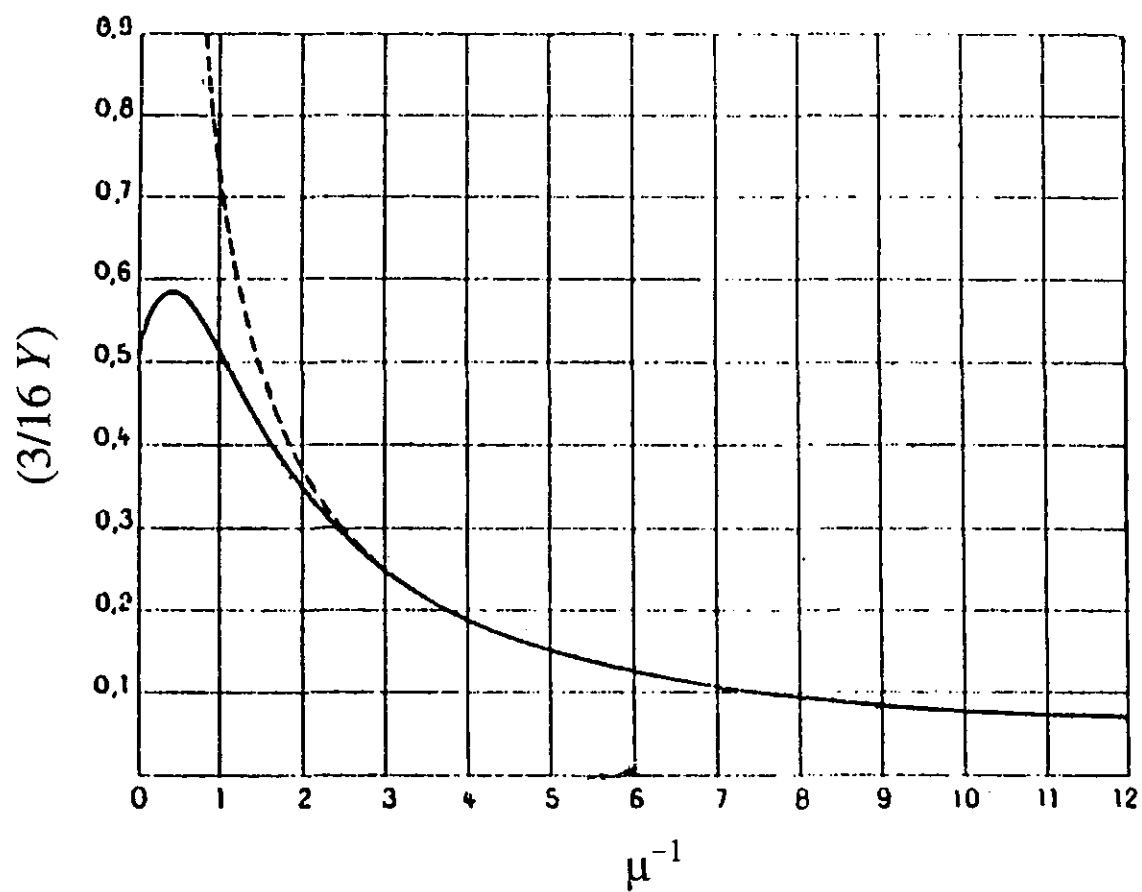


FIGURE A1. Langevin's (1905) graph of  $(3/16 Y)$  versus  $\mu^{-1}$  is the solid curve. Elastic-sphere repulsion without polarization interaction is the dashed curve. The polarization interaction without elastic-sphere repulsion is the intercept at  $\mu^{-1} = 0$ , where  $(3/16 Y) = 0.505$ .

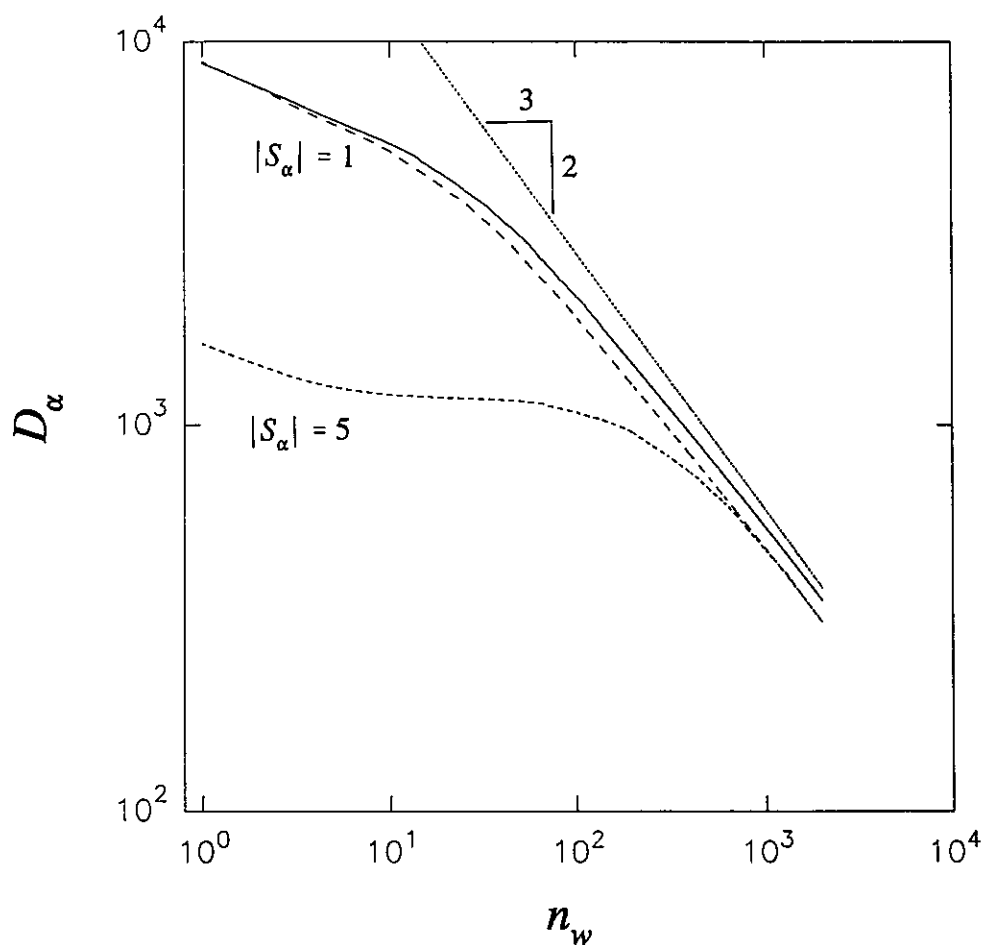


FIGURE A2. Diffusion coefficient versus number of water molecules in the hydronium ion. The solid curve is at  $T = 140$  K,  $N = 1.282 \cdot 10^{14}$  molecules /  $\text{cm}^3$ , and  $|S_\alpha| = 1$ . The long- and medium-dashed curves are both  $T = 180.65$  K and  $N = 1.654 \cdot 10^{14}$  molecules /  $\text{cm}^3$ . The long-dashed curve is  $|S_\alpha| = 1$ , while the medium-dashed curve is  $|S_\alpha| = 5$ . The short-dashed line is  $60,000 \times n_w^{-2/3}$ .